H. P. Wit

Rare earth impurities in ferromagnetic metals studied with mössbauer spectroscopy

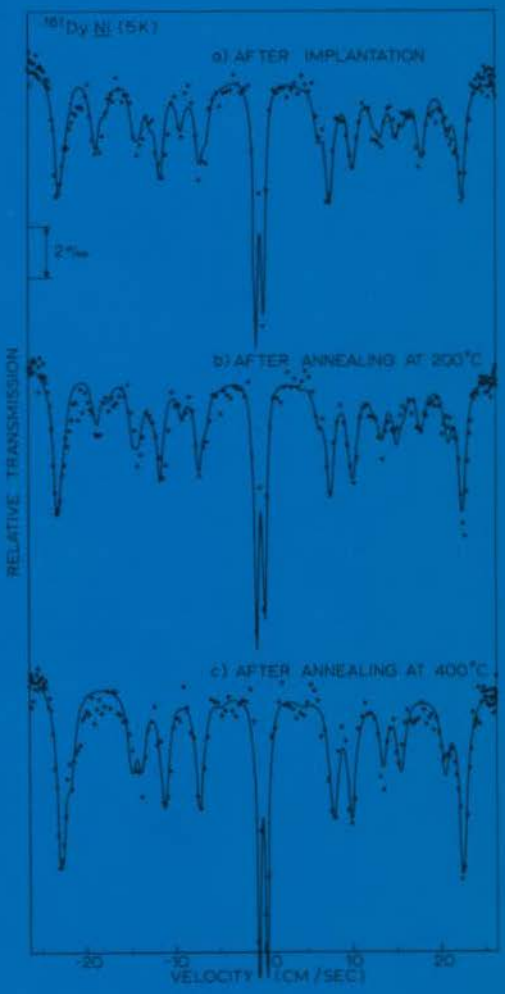

RIJKSUNIVERSITEIT TE GRONINGEN

RARE EARTH IMPURITIES IN FERROMAGNETIC METALS STUDIED WITH MÖSSBAUER SPECTROSCOPY

PROEFSCHRIFT

TER VERKRIJGING VAN HET DOCTORAAT IN DE
WISKUNDE EN NATUURWETENSCHAPPEN
AAN DE RIJKSUNIVERSITEIT TE GRONINGEN
OP GEZAG VAN DE RECTOR MAGNIFICUS DR. M. J. JANSSEN
IN HET OPENBAAR TE VERDEDIGEN OP VRIJDAG 25 JUNI 1976
DES NAMIDDAGS TE 2.45 UUR PRECIES

DOOR

HERO PIET WIT
geboren te Onstwedde

Druk: VRB Offsetdrukkerij bv – Kleine der A 4 – Groningen

PROMOTOR: Prof.Dr. H. de Waard

COREFERENT: Dr. L. Niesen

STELLINGEN

1. Het verdient aanbeveling om, op een soortgelijke manier als dat voor $\vec{Yb}Fe$ is gedaan, gecombineerde hyperfijninteratie en channeling metingen te doen aan $\vec{Dy}Ni$.

   R.B. Alexander, J. Gellert, B.I. Deutch, L.C. Feldman en E.J. Ansaldo in "Hyperfine Interactions studied in Nuclear Reactions and Decay" ed. E. Karlsson en R. Wäppling (Uppsala, 1974) p. 76.

2. De in dit proefschrift beschreven methode om relaxatiespectra uit te rekenen met behulp van de door Clauser voorgestelde procedure geeft een grote vermindering van de benodigde rekentijd.

   M.J. Clauser, Phys. Rev. B3 (1971) 3748.

3. De manier waarop Stöhr et al. Mössbauerspectra berekenen van een bron waarin relaxatie effecten optreden is fout.

   J. Stöhr, G.M. Kalvius, G.K. Shenoy en L.L. Hirst in "Hyperfine Interactions studied in Nuclear Reactions and Decay" ed. E. Karlsson en R. Wäppling (Uppsala, 1974) p. 80.

4. De component in de in dit proefschrift beschreven Mössbauerspectra, die wordt veroorzaakt door niet-substitutionele onzuiverheden, kan ook worden toegeschreven aan onzuiverheidsparen.

5. Het door Leffelaar gegeven "bewijs" voor het uitdrogen van de huid onder de positieve electrode tijdens de behandeling van een patient met een galvanische stroom is kenmerkend voor de manier waarop fysiotherapeuten met de natuurkunde omspringen.

   E.G. Leffelaar en Sv. Cohen Stuart in "Compendium Fysiotechniek" (De Tijdstroom, Lochem, 1969) p. 54.

6. De door Miedema gegeven frequentie voor ultrasonore trillingen (1000-3000 Hz) en zijn impliciet gegeven waarde voor de lichtsnelheid in lucht (3×10^7 m/sec) getuigen niet van veel begrip van de natuurkunde.

   J.J. Miedema in "Codex Medicus" (Agon Elsevier, Amsterdam, 1975) Hoofdstuk "Revalidatie".

7. Het opnemen van een Nederlandse samenvatting in een in het Engels geschreven proefschrift over een specialistisch onderwerp heeft geen zin wanneer deze samenvatting (vrijwel) dezelfde inhoud heeft als de Engelse samenvatting.

8. Evenals men bijvoorbeeld onderscheid maakt tussen een theoretisch en een experimenteel fysicus verdient het aanbeveling om onderscheid te maken tussen een theoretisch en een experimenteel onderwijskundige.

9. Een natuurkundeleraar die zijn lessen geeft zonder ze met goed uitgevoerde demonstratieproeven te verduidelijken kan beter wiskundeleraar worden.

10. De aanwezigheid van veel versnellingen op moderne sportfietsen doet vermoeden dat bij een bepaalde rijsnelheid het door de fietser ontwikkelde vermogen sterk afhangt van het toerental van de trapbeweging.

11. Bij ziekenhuispatienten wordt vrijwel altijd een polsslagfrequentie gemeten die een veelvoud is van vier.

H.P. Wit juni 1976

Aan mijn ouders

Lay-out: *Willy Smeenge*
Tekeningen: *B. Kamps*

Het in dit proefschrift beschreven onderzoek vond plaats in het Laboratorium voor Algemene Natuurkunde van de Rijksuniversiteit te Groningen in de periode 1972 - 1976. Zoals het bij dit soort onderzoek gebruikelijk is, waren verschillende medewerkers van dit laboratorium erbij behulpzaam. Hiervoor wil ik ze op deze plaats bedanken. Veel heb ik in de afgelopen vier jaar geleerd van Bert Niesen.

De computer berekeningen vonden plaats op het Rekencentrum van de Universiteit.

CONTENTS

SUMMARY

This thesis deals with investigations of samples of dilute rare earth impurities in iron and nickel using Mössbauer spectroscopy. The samples were obtained by implanting radioactive rare earth ions of ^{161}Tb and ^{169}Er by means of an isotope separator into clean and pure iron or nickel foils. From the measured spectra conclusions are drawn about the hyperfine interaction of the impurities, which in turn provides information about the lattice location of the implanted ions. Pure substitutional and defect associated sites can be distinguished. Both sites are about equally populated. This could be concluded from the annealing behaviour of the samples and from the relaxation behaviour at different temperatures. The influence of the crystalline electric field acting on the rare earth ions was analyzed in particular.

In *Chapter 1* a short introduction on hyperfine interactions and the Mössbauer effect is given. Also the method of source preparation, by implantation, is treated in this chapter, together with some basic information concerning the Mössbauer effect in Dy and Tm.

In *Chapter 2* a theoretical description of the hyperfine interaction of a rare earth ion in a ferromagnetic host is given. This theory is used to analyse the measurements. The influence of the crystalline electric field on the Mössbauer spectra is also treated in detail in this chapter.

In *Chapter 3* a thorough treatment is provided of the stochastic relaxation theory used to describe the relaxation effects observed in the spectra of some of the sources.

All instrumental details are given in *Chapter 4*. The relative shortness of this chapter is no measure for the amount of attention paid to the instrumental side of the investigation. Instrumental results, among others, are the development of a simple velocity calibration system and the improvement of Mössbauer drive systems.

In *Chapters 5* and *6* some tests are described to obtain good single line absorbers. Accurate measurements on Dy metal and Tm

metal are also described in these chapters.

In *Chapter 7* Mössbauer spectra obtained with implanted sources of DyNi, DyFe, TmNi and TmFe are given, together with the parameters derived from them by computer fitting procedures.

The measurements described in Chapter 7 are discussed in *Chapter 8*. In this discussion three subjects are treated: lattice location of the implanted ions, lack of oxidation of the samples and crystal field parameters. In the last section of Chapter 8 a summary of the results of measurements with ErNi and ErFe, carried out by other members of the group, is given.

CHAPTER 1
INTRODUCTION

Preface

The main part of this thesis deals with experiments using the Mössbauer effect to investigate samples obtained by implanting radioactive rare earth ions into iron or nickel. Measurements on the systems DyFe, DyNi, TmFe and TmNi are reported and discussed in combination with measurements on the systems ErFe and ErNi, carried out by other members of the group [1].

This work is a continuation and an extension of that started in Groningen by Inia [2], who measured Mössbauer spectra of DyFe sources. The conclusion from Inia's measurements was that the implanted rare earth ions very likely did not occupy unique positions in the host lattice. Our investigation confirms that conclusion and gives an explanation for the shape of the measured Mössbauer spectra based on the assumption that part of the implanted ions occupy substitutional sites and that part of these ions are associated with damage in the host lattice.

In the following sections of the introduction we will briefly review the main features of the hyperfine interaction of rare earth isotopes in cubic magnetic metals and of the source preparation method used in this investigation.

1.1 Hyperfine interactions

In 1924 Pauli [3] suggested that the hyperfine structure observed in the lines of optical spectra in a number of cases could be explained by assuming that the nucleus of an atom possesses a magnetic dipole moment that interacts with the surrounding electrons.

In general the multipole field, created by the distribution of electric charge and current inside the nucleus, can be decomposed into electric and magnetic multipole moments: E_0, E_1, E_2, E_3, ... and M_0, M_1, M_2, M_3, ... , being monopole-, quadrupole-, octupole-moments etc. In a system with axial symmetry parity considerations give an alternating sequency of zero multipole moments:

$M_0 = E_1 = M_2 = E_3 = ... = 0.$

In practice one deals with three interactions:

a) The Coulomb interaction of E_0 with the surrounding electrons.
b) The interaction of M_1 with an effective magnetic hyperfine field at the nucleus.
c) The interaction of E_2 with the electric field gradient at the site of the nucleus.

These interactions are extensively dealt with in textbooks on hyperfine interactions including the Mössbauer effect [4,5].

In 1959 Samoilov et al. [6] discovered that a strong magnetic field exists at the site of diamagnetic gold nuclei dissolved in iron. This discovery started much experimental and theoretical work on the subject of hyperfine interactions of impurity atoms dissolved in metals. In order to prevent the dissolved impurities from interacting with each other, their concentration should be kept very low. This makes it attractive to use radioactive nuclei to study hyperfine interactions.

One of the methods that can be applied then is the Mössbauer effect, discovered just in time (1958).

1.2 The Mössbauer effect

When a nucleus emits a gamma quantum, another nucleus of the same kind can absorb this quantum. This nuclear resonance effect was predicted already in 1929 [7].

In general, however, it is hard to observe the resonance, because of the energy difference between the gamma emission and absorption lines, that is much larger than the natural width of these lines. This energy difference is caused by the recoil of the nucleus when it emits or absorbs a gamma quantum. In 1951 gamma resonance was observed for the first time by Moon [8], who compensated for the energy difference by mounting the source in an ultra centrifuge.

Recoilless gamma resonance was discovered in 1958 by Mössbauer [9]. He moved a source of osmium metal containing ^{191}Ir, that emitted γ-rays with an energy of 129 keV, with respect to an absorber of iridium metal and measured the transmission of the γ-rays through the absorber as a function of the source velocity.

Both source and absorber were at liquid oxygen temperature (90 K). The transmission showed a minimum at zero velocity, indicating that part of the gamma quanta are emitted and absorbed without recoil: The nuclei emitting or absorbing these quanta behave as if they are fixed to the surrounding lattice.

Using the Mössbauer effect it is possible to measure the three types of hyperfine interaction mentioned in section 1.1. These interactions cause subsequently the isomer shift, the magnetic splitting and the quadrupole splitting in a Mössbauer spectrum [4].

1.3 Hyperfine interactions of rare earth impurities

An extensive survey of the Mössbauer effect in rare earths and their compounds has been given by Ofer, Nowik and Cohen [10]. We will restrict ourselves to a short introduction.

I. Magnetic hyperfine interaction

When a rare earth impurity is dissolved in a ferromagnetic metal it behaves like a trivalent ion in most cases (exceptions Eu^{2+}, Yb^{2+}).

In such an ion the 4f shell is shielded effectively from its surroundings by the 5sp electrons. This causes the spin-orbit coupling term $\lambda \underline{L} \cdot \underline{S}$ in the hamiltonian for the ion to dominate the interactions generated by the influence of the environment (crystal field, exchange field; see chapter 2). For such a rare earth $J = L \pm S$ is a good quantum number and the ground state is determined by Hund's rules. For instance, for Dy^{3+} with 9 electrons in the 4f shell: $L = 5$, $S = 5/2$, $J = 15/2$. The experimental value for the spin-orbit coupling parameter λ for this ion is 1820 cm^{-1} (= 2618 K) leading to a first excited state at $\approx$ 15000 cm^{-1} (22000 K) [11]. Corresponding values for Tm^{3+} are $L = 5$, $S = 1$, $J = 6$ and $\lambda = 2750$ cm^{-1} (= 3956 K) [11]. The exchange field and the crystal field generated by the surrounding ferromagnetic neighbours split up the ground state of the $J = L \pm S$ multiplet of the rare earth ion. The order of magnitude of the total splitting caused by the exchange field in iron is 1500 K (see chapter 8), while the strength of the crystal field is appreciably

smaller. For Ni, both interactions are of comparable magnitude (total splitting ≃ 200 K). A very simple case occurs when the interaction between the rare earth ion and its surroundings has axial symmetry. (A more general case is described in chapter 2). The magnetic hyperfine interaction for such an ion, experiencing a magnetic hyperfine field H_{hf} at its nucleus, can be described by the simple hamiltonian:

$$\mathcal{H}_m = - g_N \mu_N H_{hf} I_z \qquad (1)$$

The main contribution to H_{hf} comes from the 4f electrons (H_{4f}). (Especially the strong coupling between $\underline{L}$ and the nuclear spin $\underline{I}$ can lead to large values for H_{hf}).

In the ground state multiplet J = L ± S this 4f contribution can, for a non-degenerate electronic ground state, be written as [12]:

$$\mathcal{H}_m^{(4f)} = - g_N \mu_N H_{4f} I_z = A \langle J_z \rangle I_z = 2\mu_B g_N \mu_N \langle J_z \rangle \langle J||N||J \rangle \langle r^{-3} \rangle I_z \qquad (2)$$

Values for $A = A_J - A_S'$ are [13]: - 114.1 MHz (= - 8.72 × 10^{-4} K) for the ground state of ^{161}Dy and - 400.0 MHz (= - 3.06 × 10^{-3} K) for the ground state of ^{169}Tm.

The reduced matrix elements $\langle J||N||J \rangle$ have been tabulated by Elliot and Stevens [14].

Apart from the 4f contribution there is a component H_s of the hyperfine field caused by s electrons. When the rare earth ion is dissolved in a (ferromagnetic) metal this contribution consists of at least four terms:

a) core polarization
b) conduction electron polarization by the own 4f electrons
c) conduction electron polarization due to the host
d) other effects, e.g. covalency [15].

According to Watson and Freeman [16] the core polarization can be estimated by:

$$H_{cp} = - 90 (g_J - 1) J \text{ kOe}.$$

The two different parts of the conduction electron polarization contribution are discussed by Hüfner [17]. For a source of ErFe the theoretical H_s is about 3 % of the theoretical H_{4f} [1]. The s contribution can, as far as it is proportional to $\langle J_z \rangle$, be absorbed in the value of $\langle r^{-3} \rangle$ in formula (2) to calculate the total magnetic hyperfine field $(H_{4f} + H_s)$.

II. Electric quadrupole interaction

Since the quadrupole contribution to the hyperfine interaction arises predominantly from the electrons of the rare earth ion itself, this contribution and the magnetic contribution are both quantized along the magnetization axis of the ferromagnetic domain. This quadrupole contribution can then be written as:

$$\mathcal{H}_Q^{(4f)} = \frac{e^2 \cdot q_{4f} \cdot Q}{4} \cdot \frac{3I_z^2 - I(I+1)}{I(2I-1)} \cdot (1 - R) \qquad (3)$$

in which q_{4f} is the electric field gradient produced by the 4f electrons and Q is the nuclear quadrupole moment.

The term $(1 - R)$ accounts for the distortion of the charge cloud of the inner closed shells of electrons that produces an appreciable change in the electric field gradient at the nucleus (Sternheimer shielding). The magnitude of R is rather uncertain (0.1 - 0.4). Using the matrix elements $\langle J||\alpha||J \rangle$ that have also been tabulated by Elliot and Stevens [14], $\mathcal{H}_Q^{(4f)}$ can be written as:

$$\mathcal{H}_Q^{(4f)} = -\frac{e^2 Q}{4I(2I-1)} (3\langle J_z^2 \rangle - J(J+1)) \times \langle J||\alpha||J \rangle \langle r^{-3} \rangle (1 - R)(3I_z^2 - I(I+1)) \qquad (4)$$

Apart from q_{4f}, the nucleus of the rare earth ion may experience an electric field gradient produced by charges of the lattice surrounding it. This gradient is amplified by the distortion induced in the closed shells of the 4f ion (Sternheimer antishielding); in general, however, it is an order of magnitude smaller than q_{4f}. In the case of cubic symmetry around the ion the lattice contribution vanishes.

1.4 ^{161}Dy Mössbauer effect [18]

In our measurements we used the gamma transition with energy E_γ = 25.65 keV occurring in the decay of ^{161}Tb to ^{161}Dy. As can be seen from fig. 1.1 the spin-parity assignment of the ground state is $5/2^+$ and that of the excited state is $5/2^-$. The transition has E_1 character leading to 16 possible transitions between these two states. The lifetime of the excited state is reasonably long ($T_{\frac{1}{2}}$ = 28.1 ns), leading to a natural linewidth $\Gamma = \frac{\ln 2}{2\pi \cdot T_{\frac{1}{2}}}$ = 3.92 MHz. (This is equivalent to 1.62 × 10^{-8} eV or to 0.19 mm/s).

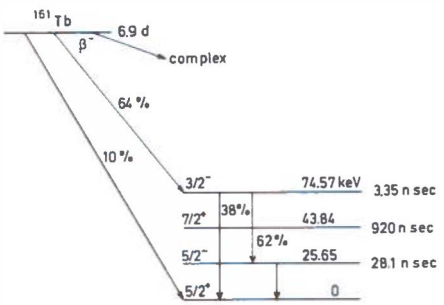

Fig. 1.1
Part of the decay scheme of ^{161}Tb [18,19].

So the minimum observable linewidth in a Mössbauer experiment is $\Gamma_{source} + \Gamma_{absorber}$ = 0.38 mm/s. The minimum linewidth we have observed in our measurements was about a factor 10 larger, but as the over all hyperfine splitting for a free Dy^{3+} ion is about 45 cm/s, well resolved spectra were obtained in most cases.

The magnetic moment of the ground state of ^{161}Dy is μ = − 0.472(13) nm [20]. We have measured the ratios of the magnetic- and quadrupole-moments of the excited and ground state very accurately (see section 5.2) and found: μ^*/μ = − 1.2382(13), Q^*/Q = 0.9883(7). The value for μ^*/μ is within the errors the same as that measured by Cohen and West [21]. Our value of Q^*/Q differs slightly from their value 0.995(2). The natural abundance of ^{161}Dy is 18.88 %.

1.5 ^{169}Tm Mössbauer effect [22]

The ^{169}Tm-nucleus has a 8.401 keV [23] gamma transition suitable for Mössbauer work, although the high conversion coëf-

ficient ($\alpha \approx 300$) requires the use of strong sources in order to obtain reasonable counting rates. The spin-parity assignment of the ground state and the excited state are $1/2^+$ and $3/2^+$ subsequently, as can be seen from fig. 1.2. The transition has M_1 character, leading to six possible transitions between these two states.

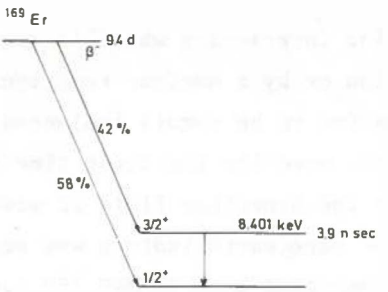

Fig. 1.2
Part of the decay scheme of ^{169}Er [22].

The lifetime of the excited state is 3.9 ns, leading to a natural linewidth of 28.2 MHz = 1.17×10^{-7} eV = 4.17 mm/s.

In our measurements we observed a linewidth of about 3.5 cm/s, being about 4 times the minimum observable linewidth. For a free Tm^{3+} ion the over all splitting is about 110 cm/s. So a special velocity transducer can be necessary in Mössbauer experiments with this isotope.

The magnetic moment of the ground state of ^{169}Tm is $\mu = -0.231(1)$ nm [22]. We have measured the ratio of the magnetic moments of the ground state and the excited state accurately (see section 6.2): $\mu^*/\mu = -2.223(13)$. The natural abundance of ^{169}Tm is 100 %.

1.6 Implantation

It is impossible to make dilute solutions of rare earth impurities in iron or nickel by alloying or diffusion. Nevertheless such systems can be studied if the impurities are implanted. This means that the impurities are shot into the material as ions with a high kinetic energy. To keep the concentration of the implanted ions low, radioactive isotopes must be used. Two methods can be used for such an implantation:

a) The ions are accelerated in an isotope separator. This method was used for the first time by De Waard and Drentje to measure the hyperfine field of ^{129}I in iron [24]. For this purpose they implanted radioactive ^{129m}Te ions into an iron foil by means of the Groningen isotope separator [25] and measured the hyperfine field at the ^{129}I nucleus using Mössbauer spectroscopy.

b) An excited state of the hyperfine interaction which is measured is produced by Coulomb excitation or by a nuclear reaction, which causes the nuclei in question to be recoil implanted into the backing. This method was used for the first time by Grodzins et al. [26] to measure the hyperfine field of some rare earth isotopes in iron. The rare earth isotope was evaporated onto an iron foil and bombarded with 36 MeV ^{16}O ions. The magnetic hyperfine fields were derived from the time integral perturbed angular distribution of gamma rays emitted by the implanted nuclei.

With the first implantation method the concentration of the implanted ions can easily become too high, because of the small penetration depth. A typical value for the dose in the sources we have prepared is 10^{14} implanted ions per cm^2. The ions were implanted with an energy of about 130 keV.

Using the theory of Lindhard, Scharff and Schiøtt [27] we calculate a mean penetration depth of 220 Å in iron for ^{161}Tb or ^{169}Er ions. If we assume the depth distribution to be Gaussian, the width of the distribution curve, calculated with the same theory, is 140 Å. From this we find a maximum impurity concentration of about 0.1 at.%. For implants in nickel the estimated maximum concentration is the same. The L.S.S. theory is based on the assumption that the ions are implanted into amorphous materials. For implants into crystalline materials the maximum concentration will be lower than the value calculated above. This is caused by the fact that the impurity distribution will have a "channeling tail" [28].

As starting material for the implantation of rare earth ions neutron irradiated trivalent oxides were used (R_2O_3). As these oxides have very high melting points (> 2000°C) they were

converted into trichloride (RCl_3) in the ion source of the isotope separator by means of the CCl_4 method [2,29]. The melting point of the chloride is only about 700°C.

During the implantation the current of the stable beam (e.g. ^{160}Gd when ^{161}Tb is implanted) is measured in a Faraday cup. The ion current of the radioactive beam is about 2000 times smaller than that of the stable beam. The Faraday cup, however, measures a stable beam current that is about a factor 3 larger than the ion current falling into it. This is caused by secondary electrons leaving the cup.

If we assume the irradiated area to be a uniformly implanted rectangle with a width of d mm and a height of 35 mm (= height of the beam profile) we can calculate: (the ions in the beam are monovalent):

$$D = 1.1 \times 10^{13} \times Q/d \qquad (1)$$

D is the implanted dose in at/cm^2; Q is the total charge measured in the Faraday cup in μAh. We have used this formula to estimate the dose of the implanted sources. Our estimates are believed to be correct within a factor of 2.

The radii of iron and nickel atoms in the metal are 1.24 Å [30]. In the intermetallic compounds $TmNi_2$, $DyNi_2$, $TmFe_2$ and $DyFe_2$, that all have a cubic structure ($MgCu_2$-type), the radii of the rare earth atoms range from 1.54 Å to 1.58 Å [31]. So it is likely to assume that a rare earth impurity, that is implanted into iron or nickel, does not fit very well in the host lattice.

In channeling measurements [32] it has been seen that after a room temperature implantation roughly only one half of the impurities occupy substitutional sites in the lattice.

1. L. Niesen and P.J. Kikkert in "International conference on Hyperfine Interactions studied in nuclear reactions and decay", ed. E. Karlson and R. Wäppling, (Upplands Grafiska AB, Uppsala, 1974) p. 160.
2. P. Inia, Thesis, Groningen (1971).
3. W. Pauli, Naturwissenschaften 12 (1924) 741.
4. H. Wegener, "Der Mössbauer Effekt und seine Anwendung in Physik und Chemie", (Bibliographisches Institut, Mannheim, 1966).
5. B. Bleaney in "Hyperfine Interactions", ed. A.J. Freeman and R.B. Frankel, (Academic Press, New York, 1967).
6. B.N. Samoilov, V.V. Sklyarevskii and E.P. Stepanov, Zh. Eksperim. i Theor. Fiz. 36 (1959) 644 [Engl. Transl.: Sov. Phys. JETP 36 (1959) 448].
7. W. Kuhn, Phil. Mag. 8 (1929) 625.
8. P.B. Moon, Proc. Roy. Soc. 64 (1951) 76.
9. R.L. Mössbauer, Z. Phys. 151 (1958) 124,
   R.L. Mössbauer, Naturwissenschaften 45 (1958) 538,
   R.L. Mössbauer, Z. Naturforschung 14a (1959) 211.
10. S. Ofer, I. Nowik and S.G. Cohen in "Chemical Applications of Mössbauer spectroscopy", ed. V.I. Goldanskii and R.H. Herber (Academic Press, New York, 1968) Chapter 8.
11. A. Abragam and B. Bleaney, "Electron paramagnetic resonance of transition ions", (Clarendon Press, Oxford, 1970) p. 284.
12. l.c. ref. 9, p. 296
13. l.c. ref. 9, p. 298
14. R.J. Elliot and K.W.H. Stevens, Proc. Roy. Soc A218 (1953) 553.
15. H. Maletta, G. Crecelius and W. Zinn, J. Physique Colloque C6 (1974) 279.
16. R.E. Watson and A.J. Freeman in "Hyperfine Interactions", ed. A.F. Freeman and R.B. Frankel (Academic Press, New York, 1967) Chapter 2.
17. S. Hüfner, Phys. Rev. Lett. 19 (1967) 1034.
18. "Mössbauereffect Data Index 1972", ed. J.G. Stevens and V.E. Stevens, (Adam Hilger, London, 1973) p. 138.

19. C.M. Lederer, J.M. Hollander and I. Perlman in "Table of Isotopes" (1967).
20. E. Münck, Z. Phys. 208 (1968) 184.
21. R.L. Cohen and K.W. West in "Hyperfine Interactions in excited nuclei", ed. G. Goldring and R. Kalish (Gordon and Breach, New York, 1971) p. 613.
22. "Mössbauer effect Data Index 1970", ed. J.G. Stevens and V.E. Stevens, (Plenum, New York, 1971) p. 613.
23. Nuclear Data Sheets B10 (1973) 381.
24. H. de Waard and S.A. Drentje, Phys. Lett. 20 (1966) 38.
25. S.A. Drentje, Nucl. Instrum. Meth. 59 (1968) 64 and Thesis, University of Groningen (1969).
26. L. Grodzins, R.R. Borchers and G.B. Hageman, Phys. Lett. 21 (1966) 214.
27. J. Lindhard, M. Scharff and H.E. Schiøtt, Mat. Fys. Medd. Dan. Vid. Selsk. 33 (1963) number 14.
28. J.L. Whitton in "Channeling", ed. D.V. Morgan (John Wiley, New York, 1973) p. 231.
29. G. Sidenius and O. Skilbreid in "Electromagnetic separation of radioactive isotopes", ed. M.J. Higatsberger and F.P. Viehbock (Springer Verlag, Vienna, 1961).
30. From X-ray crystallographic data in "Handbook of Chemistry and Physics" 53rd ed.
31. K.N.R. Taylor, Advances in Physics 20 (1971) 551.
32. R.B. Alexander, J. Gellert, B.I. Deutch, L.C. Feldman and E.J. Ansaldo, l.c. ref. 1, p. 76.

CHAPTER 2

THEORETICAL DESCRIPTION OF RARE EARTH IMPURITIES IN A FERROMAGNETIC HOST.

2.1 Rare earth ion in cubic crystalline electric field

Introductions to crystal field theory have been given, for instance, by Abragam and Bleaney [1] and by Hutchings [2]. The case of rare earth ions in a crystalline field of cubic symmetry has been treated thoroughly by Lea, Leask and Wolf [3]. As was already remarked in the introduction, the spin-orbit coupling dominates the effect of the solid state environment for a rare earth ion. Therefore, the effect of the crystalline electric field can be treated within the ground state multiplet of the rare earth ion, the result being the removal of the spatial degeneracy of the total angular momentum J. Quantitatively the effect can be calculated using the so-called "operator equivalent" technique, originally developed by Stevens [4].

Within a manifold of angular momentum J, composed of f-electron wave functions, the most general operator equivalent potential with cubic point symmetry may be written as:

$$\mathcal{H} = B_4(O_4^0 + 5O_4^4) + B_6(O_6^0 - 21O_6^4) \qquad (1)$$

if the hamiltonian is quantized along a (1,0,0) direction.

Expressions for the fourth and sixth degree spherical tensor operators O_4^0, O_4^4 and O_6^0, O_6^4 can be found in the article of Lea, Leask and Wolf [3] or in the book of Abragam and Bleaney [1].

The coëfficients B_4 and B_6 determine the magnitude of the crystal field splitting. They are linear functions of $\langle r^4 \rangle$ and $\langle r^6 \rangle$, the mean fourth and sixth powers of the radii of the magnetic ion wave functions. Since these are very difficult to calculate quantitatively, it is customary to regard the coëfficients B_4 and B_6 as parameters to be determined empirically.

2.2 The host-impurity exchange interaction

Up to now we have supposed that only a crystalline electric

field acts on the magnetic ion. However, the rare earth ion spin $\vec{S}$ also experiences an exchange interaction with the (polarized) conduction electrons $\vec{s}$, which, in a molecular field approximation, can be written as:

$$\mathcal{H} = - J_{sf} \langle \vec{s} \rangle \cdot \vec{S} = -(g_J - 1) J_{sf} \langle \vec{s} \rangle \cdot \vec{J} = (g_J - 1)\mu_B \vec{H}_{exch} \cdot \vec{J} \qquad (1)$$

J_{sf} is the s-f exchange integral. g_J is the Landé factor and $\vec{H}_{exch}$ is the effective exchange field acting on the 4f electron spin. It can be remarked here, that apart from the well-known s-f exchange mechanism, other magnetic interactions may play a role, such as a 3d-5d exchange between the host and the impurity [5]. All such interactions will be absorbed in $\vec{H}_{exch}$.

The total hamiltonian can thus be written as:

$$\mathcal{H} = (g_J - 1)\mu_B \vec{H}_{exch} \cdot \vec{J} + B_4(O_4^0 + 5O_4^4) + B_6(O_6^0 - 21O_6^4) \qquad (2)$$

The direction of this exchange field with respect to the crystal field can be defined by angles θ and ψ (see fig. 2.1).

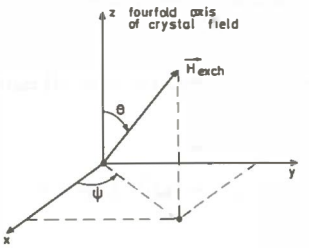

Fig. 2.1 Direction of exchange field.

Using the operators $J_+ = J_x + iJ_y$ and $J_- = J_x - iJ_y$ [6], the first term in (2) can be written as:

$$(g_J - 1)\mu_B \vec{H}_{exch} \cdot \vec{J} = (g_J - 1)\mu_B H_{exch} \times \left[J_z \cos\theta + \tfrac{1}{2}(J_+ + J_-)\sin\theta \cos\psi + \frac{1}{2i}(J_+ - J_-)\sin\theta \sin\psi\right] \qquad (3)$$

This operator is real as long as $\psi = 0$. For $\theta = 0$ it simply reduces to:

$$(g_J - 1)\mu_B H_{exch} \cdot J_z \tag{4}$$

2.3 Application of theory to DyNi and TmNi

We want to apply the theory of the previous section to Dy or Tm ions that occupy a substitutional site in nickel.

Because the "axis of easy magnetization" of nickel is along the (1,1,1) direction in the crystal [7] we can safely assume that in polycrystalline nickel in zero external field the exchange field will be directed along this axis for the majority of the domains. In this case it is more convenient to write the hamiltonian with the (1,1,1) direction as a 3-fold quantization axis. Then, using the transformation properties of the spherical tensor operators, the hamiltonian can be written as [8]:

$$\mathcal{H} = (g_J - 1)\mu_B H_{exch} J_z - \frac{2}{3}B_4\{O_4^0 + 20\sqrt{2}\cdot O_4^3\} + \frac{16}{9}B_6\{O_6^0 - \frac{35}{4}\sqrt{2}\cdot O_6^3 + \frac{77}{8}O_6^6\} \tag{1}$$

(One of the signs in the corresponding expression given by Hutchings is wrong [9]).

The operators O_4^0, O_4^3 etc. are given by Abragam and Bleaney [10]:

$$O_4^0 = 35J_z^4 - [30J(J+1) - 25]\,J_z^2 - 6J(J+1) + 3J^2(J+1)^2 \tag{2}$$

$$O_6^0 = 231J_z^6 - 105[3J(J+1) - 7]\,J_z^4 + [105J^2(J+1)^2 - 525J(J+1) + 294]\,J_z^2 - 5J^3(J+1)^3 + 40J^2(J+1)^2 - 60J(J+1) \tag{3}$$

$$O_4^3 = \tfrac{1}{4}[J_z(J_+^3 + J_-^3) + (J_+^3 + J_-^3)J_z] \tag{4}$$

$$O_6^3 = \tfrac{1}{4}\left[\{11J_z^3 - 3J_z \cdot J(J+1) - 59J_z\}\ (J_+^3 + J_-^3) + \right.$$
$$\left. + (J_+^3 + J_-^3)\ \{11J_z^3 - 3J_z \cdot J(J+1) - 59J_z\}\right] \tag{5}$$

$$O_6^6 = \tfrac{1}{4}(J_+^6 + J_-^6) \tag{6}$$

Numbering $m = 1, 2, \ldots\ldots 2J+1$ and $n = 1, 2, \ldots\ldots 2J+1$ and using the expressions [11]:

$$\langle m|J_z|n\rangle = \delta_{mn}\ (m - J - 1) \tag{7}$$

$$\langle m|J_+|n\rangle = \delta_{m,n+1}\ \{m(2J+1-m)\}^{\frac{1}{2}} \tag{8}$$

$$\langle m|J_-|n\rangle = \delta_{m,n-1}\ \{(m-1)(2J+2-m)\}^{\frac{1}{2}} \tag{9}$$

we can write down the matrix elements H_{mn} of the hamiltonian (1):

$$H_{mn} = \delta_{mn} \cdot P_0(m,J) + \delta_{m,n+3} \cdot P_3(m,J) + \delta_{m,n+6} \cdot P_6(m,J) \tag{10}$$

P_0, P_3 and P_6 can be calculated straightforward from (2) - (9).

As the matrix is symmetric (and real) it is no problem that only the lower triangle has been given by (10).

2.4 Calculation of the matrix elements of the electron-spin hamiltonian

For computational reasons we write the hamiltonian 2.3.(1) as:

$$\mathcal{H} = W\{2y \cdot J_z + x \cdot \frac{O_4}{F_4^0} + (1 - |x|)\ \frac{O_6}{F_6^0}\} \tag{1}$$

In this expression

$$2Wy = (g_J - 1)\mu_B\ H_{exch} \tag{2}$$

gives the strength of the exchange field. The relative strength of

the exchange field with respect to the crystal field is described by y. The eigenvalues of $\mathcal{H}$, giving the electronic energy levels, are proportional to the scale factor W. All possible values of the ratio between the fourth and the sixth degree terms of the crystal field are covered by putting [3]:

$$B_4 F_4^0 = Wx \tag{3}$$

$$B_6 F_6^0 = W(1 - |x|) \tag{4}$$

where
$$-1 \leq x \leq +1 \tag{5}$$

The factors F_4^0 and F_6^0 are common to all matrix elements of O_4^0 and O_6^0. From (3) and (4) we get:

$$\frac{B_4}{B_6} = \frac{x}{1 - |x|} \frac{F_6^0}{F_4^0} \tag{6}$$

The operators O_4 and O_6 are given by

$$O_4 = -\frac{2}{3} O_4^0 - \frac{40}{3}\sqrt{2}\, O_4^3 \tag{7}$$

and

$$O_6 = \frac{16}{9} \cdot O_6^0 - \frac{140}{9}\sqrt{2}\, O_6^3 + \frac{154}{9} O_6^6 \tag{8}$$

We can now construct the matrix elements of the hamiltonian for the cases of Dy^{3+} ($J = 15/2$) and Tm^{3+} ($J = 6$) using the expressions for the spherical tensor operators given in section 2.3. These matrix elements H_{mn} are given in Table 2.I.

Once the matrix has been constructed, its eigenvalues and eigenvectors can be calculated.

2.5 The hyperfine structure hamiltonian

The hyperfine structure hamiltonian for a rare earth ion in a ferromagnetic host can be written as [12] (see section 1.3):

$$\mathcal{H}_{hf} = \mathcal{H}_m + \mathcal{H}_Q = 2\mu_B g_N \mu_N \langle r^{-3} \rangle \langle J||N||J \rangle \vec{J}\cdot\vec{I} + \frac{e^2 Q \langle r^3 \rangle}{I(2I-1)} \langle J||\alpha||J \rangle (1-R) \{\frac{3}{2}(\vec{J}\cdot\vec{I})^2 + \frac{3}{4}(\vec{J}\cdot\vec{I}) - \frac{1}{2} J(J+1)\cdot I(I+1)\} \tag{1}$$

If we introduce a magnetic hyperfine splitting constant by

$$A = 2\mu_B g_N \mu_N \langle r^{-3} \rangle \langle J||N||J \rangle \tag{2}$$

and a quadrupole splitting constant by

$$K = \frac{e^2 Q \langle r^{-3} \rangle}{I(2I-1)} \langle J||\alpha||J \rangle (1 - R) \tag{3}$$

we can write the hamiltonian as [13]:

$$\mathcal{H}_{hf} = AJ_zI_z + \frac{1}{2}A(J_+I_- + J_-I_+) + \frac{1}{4}K\{3J_z^2 - J(J+1)\}\{3I_z^2 - I(I+1)\} +$$

$$+ \frac{3}{8}K(J_zJ_+ + J_+J_z)(I_zI_- + I_-I_z) + \frac{3}{8}K(J_zJ_- + J_-J_z)(I_zI_+ + I_+I_z) +$$

$$+ \frac{3}{8}K(J_+^2I_-^2 + J_-^2I_+^2) \tag{4}$$

We will use this hamiltonian to calculate the Mössbauer spectrum for the case that the electron spin of the rare-earth ion is in its ground state, while the degeneracy of the electron-spin manifold has been removed by the combination of exchange field and crystal field outlined in sections 2.1 and 2.2. If $|\psi_0\rangle$ denotes the electronic ground state, we can write:

$$|\psi_0\rangle = \sum_{N=-J}^{+J} |N\rangle \langle N|\psi_0\rangle \equiv \sum_{N=-J}^{+J} |N\rangle C_N \tag{5}$$

in which the C_N are the elements of the eigenvector $\vec{C}$ of the ground state, i.e. an eigenvector of the electron-spin matrix of section 2.4.

The $2I+1$-fold degeneracy of the electronic ground state is removed by the hyperfine interaction $\mathcal{H}_{hf}$.

We assume that $\mathcal{H}_{hf} << \mathcal{H}_{exch} + \mathcal{H}_{crystalfield}$ (see section 1.3). Then matrix-elements of the form $\langle \psi_0, m|\mathcal{H}_{hf}|\psi_i, n\rangle$ can be neglected if $\psi_0 \neq \psi_i$. This means that the problem has been reduced to finding eigenvalues and eigenvectors of a $(2I+1)$-dimensional matrix H_{hf} with elements given by:

$$H_{m,n}^{(hf)} = \langle \psi_0, m|\mathcal{H}_{hf}|\psi_0, n\rangle \tag{6}$$

For the first term of $\mathcal{H}_{hf}$, given by (4), this is for instance:

$$\langle\psi_0,m|AJ_zI_z|\psi_0,n\rangle = A\cdot\langle\psi_0|J_z|\psi_0\rangle\ (m-I-1)\cdot\delta_{mn} \qquad (7)$$

with $m = 1, 2, \ldots\ldots, 2I+1$.

This term is proportional to the expectation value of J_z in the electronic ground state. This expectation value can be calculated using:

$$\langle\psi_0|J_z|\psi_0\rangle = \sum_{M,N=-J}^{+J} \langle\psi_0|M\rangle\ \langle M|J_z|N\rangle\ \langle N|\psi_0\rangle = \sum_{M=-J}^{+J} C_M^* C_M \cdot M \qquad (8)$$

By writing down all the terms in the elements of $\mathcal{H}_{hf}$ it turns out that the following expectation values have to be calculated: $\langle J_z\rangle$, $\langle J_z^2\rangle$, $\langle J_+\rangle$, $\langle J_-\rangle$, $\langle J_zJ_+\rangle$, $\langle J_+J_z\rangle$, $\langle J_zJ_-\rangle$, $\langle J_-J_z\rangle$, $\langle J_+^2\rangle$, $\langle J_-^2\rangle$. However, in the assumption we have made (exchange field along 3-fold axis of crystal field) all the expectation values vanish, except the first two. This is caused by the fact that these vanishing expectation values contain products like $C_{M+1}^* C_M$, $C_{M+2}^* C_M$, etc., while the shape of the eigenvector $\vec{C}$ is

$$\underline{C}^T = (\ldots\ldots, C_1, 0, 0, C_4, 0, 0, C_7, 0, 0, \ldots\ldots) \qquad (9)$$

So we are only left with

$$\langle J_z\rangle \equiv \langle\psi_0|J_z|\psi_0\rangle = \sum_{M=-J}^{J} C_M^* C_M \cdot M = \sum_{k=1}^{2J+1} C_k^* C_k\ (k-J-1) \qquad (10)$$

and

$$\langle J_z^2\rangle \equiv \langle\psi_0|J_z^2|\psi_0\rangle = \sum_{M=-J}^{J} C_M^* C_M \cdot M^2 = \sum_{k=1}^{2J+1} C_k^* C_k\ (k-J-1)^2 \qquad (11)$$

This makes it easy to write down the matrix elements of $\mathcal{H}_{hf}$ that is diagonal now:

$$H_{m,n}^{(hf)} = \delta_{mn}\{A\langle J_z\rangle\ (m-I-1) + \tfrac{1}{3}K\left[3\langle J_z^2\rangle - J(J+1)\right] \times \left[3(m-I-1)^2 - I(I+1)\right]\} \qquad (12)$$

The same matrix elements can be obtained from the hamiltonian for a free rare-earth ion in a field with axial symmetry (see 1.3.(2) and 1.3.(4)).

$$\mathcal{H} = A\langle J_z\rangle I_z + \tfrac{1}{4}K\left[3\langle J_z^2\rangle - J(J+1)\right]\left[3I_z^2 - I(I+1)\right] \qquad (13)$$

For such a free ion

$$|\langle J_z\rangle| = J \qquad (14)$$

$$\langle J_z^2\rangle = J^2 \qquad (15)$$

which gives the so-called ionic values for the magnetic and electric hyperfine interaction.

The presence of the cubic crystalline electric field in general reduces $|\langle J_z\rangle|$ and $\langle J_z^2\rangle$ below their ionic values. For this case we introduce the reduction factors:

$$R_m = \frac{|\langle J_z\rangle|}{J} \qquad (16)$$

for the magnetic hyperfine field

and

$$R_q = \frac{3\langle J_z^2\rangle - J(J+1)}{3J^2 - J(J+1)} \qquad (17)$$

for the quadrupole splitting.

2.6 Reduction of $\langle J_z\rangle$ and $\langle J_z^2\rangle$ for different values of x and y

A computer program has been made to calculate the eigenvalues and eigenvectors of the electron spin matrix given in section 2.4. From the eigenvector of the ground state $\langle J_z\rangle$ and $\langle J_z^2\rangle$ are calculated, giving the reduction factors R_m and R_q. This has been done for different values of x and y, both for $W=+1$ and $W=-1$. (If the sign of W changes, the electronic energy level scheme is turned upside down). The results of the calculations are shown in fig. 2.2 for $J = 15/2$ (Dy^{3+}) and in fig. 2.3 for $J = 6$ (Tm^{3+}).

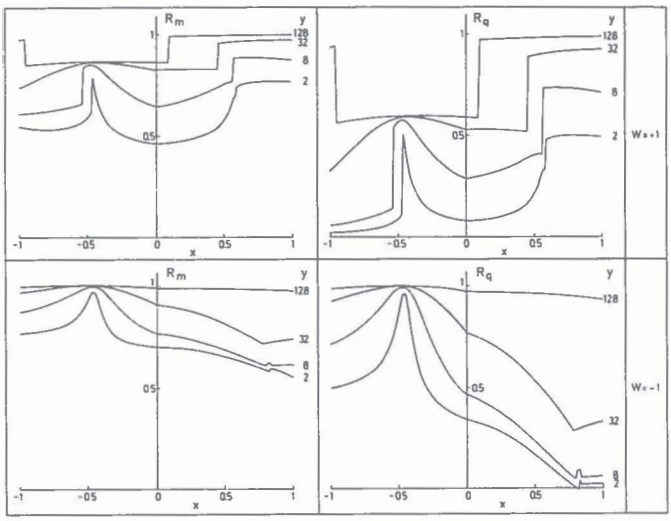

fig. 2.2 Reduction of hyperfine field (R_m) and quadrupole splitting (R_q) for J = 15/2.

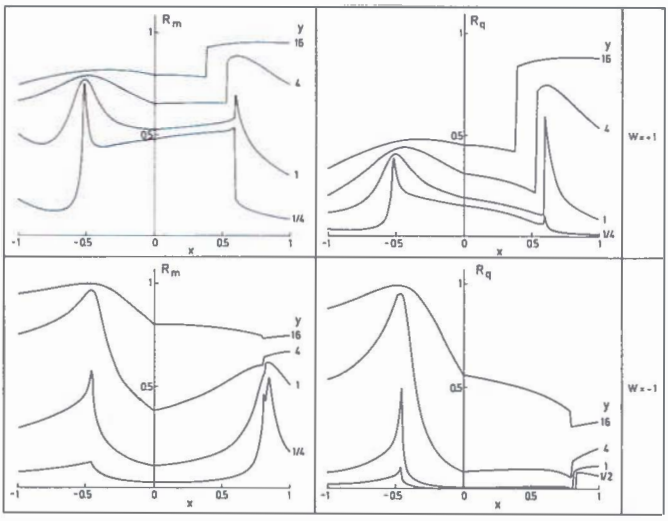

fig. 2.3 Reduction of hyperfine field (R_m) and quadrupole splitting (R_q) for J = 6.

2.7 Effective reduction of magnetic field and quadrupole splitting in the case of fast relaxation

As will be pointed out in section 3.1, the magnetic hyperfine field in the fast relaxation limit can be obtained by taking a Boltzmann-average over the electronic sublevels. The magnetic hyperfine field is then proportional to:

$$\sum_k p_k \langle J_z \rangle_k \qquad (1)$$

in which p_k is the population of the k-th sublevel and $\langle J_z \rangle_k$ its expectation value for J_z.

$$p_k = exp\left[-E_k/kT\right] \; / \; \sum_j exp\left[-E_j/kT\right] \qquad (2)$$

where E_k is the electronic energy of the k-th sublevel; i.e. the k-th eigenvalue of the electron-spin matrix. $\langle J_z \rangle_k$ can be calculated from the eigenvector belonging to this eigenvalue. (See 2.5.(10)).

The quadrupole splitting which is proportional to

$$3\sum_k p_k \langle J_z^2 \rangle_k - J(J+1) \qquad (3)$$

(see sect. 3.1) can be calculated similarly.

A typical result of a calculation based on expressions (1) and (3) is given in fig. 2.4. This figure shows the reduction of the effective hyperfine field $H(T)/H(0)$ and the quadrupole splitting $Q(T)/Q(0)$ with increasing temperature T in the case of fast relaxation for J = 15/2. ($H(0)$ and $Q(0)$ are the values for the magnetic hyperfine field and the quadrupole splitting if only the lowest electronic level is populated.

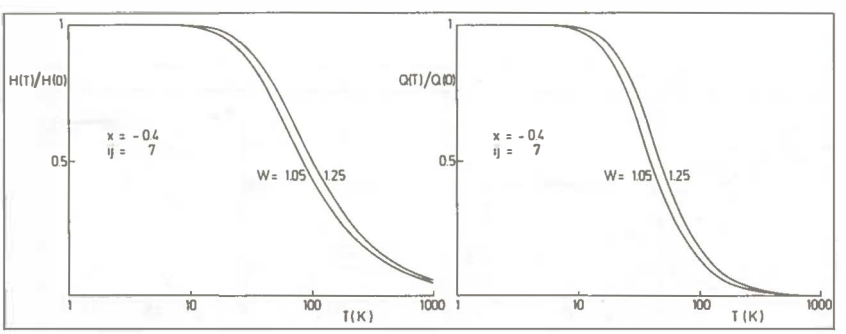

fig. 2.4 Reduction of hyperfine field and quadrupole splitting for J = 15/2 (fast relaxation).

2.8 Application of the theory on TmFe

In iron the "axis of easy magnetisation" is along the (1,0,0) direction in the crystal [7]. If we take this (1,0,0) direction as a four fold quantization axis the hamiltonian can be written as:

$$\mathcal{H} = (g_J - 1)\,\mu_B\,H_{exch}\,J_z + B_4(O_4^0 + 5O_4^4) + B_6(O_6^0 - 21O_6^4) \qquad (1)$$

With the notation of section 2.4 this hamiltonian becomes:

$$\mathcal{H} = W\{2y \cdot J_z + x\,\frac{O_4}{F_4^0} + (1 - |x|)\,\frac{O_6}{F_6^0}\} \qquad (2)$$

In this expression the operators O_4 and O_6 are given by:

$$O_4 = O_4^0 + 5O_4^4 \qquad (3)$$

$$O_6 = O_6^0 - 21O_6^4 \qquad (4)$$

Using the tables, given by Abragam and Bleaney [14], for the matrix elements of these operators, the matrix elements of the electron spin matrix can be calculated for the case that J = 6 (Tm^{3+}). Using the eigenvalues and eigenvectors of this electron spin matrix, the reduction of $\langle J_z \rangle$ for different values of x and y can be calculated in the same way as in section 2.6. The results of this calculation are given in fig. 2.5.

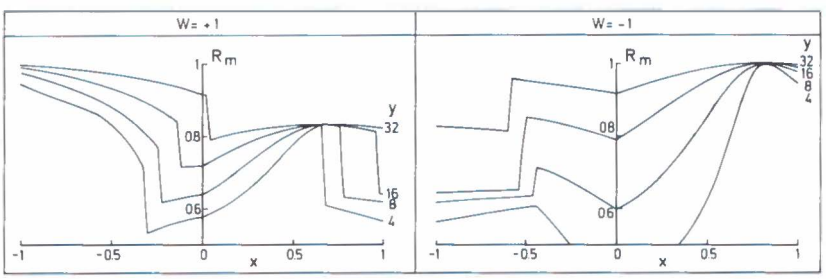

fig. 2.5. Reduction of hyperfine field (R_m) for J = 6 in iron.

Table 2.I Matrix elements of electron-spin matrix

$H_{i,i} = C_{1,i} \cdot Wy - \frac{2}{3} C_{2,i} \cdot Wx + \frac{16}{9} C_{3,i} W (1 - |x|)$

i	$C_{1,i}$	$C_{2,i}$	$C_{3,i}$	
1	-15	273	65	
2	-13	- 91	-117	
3	-11	-211	- 39	
4	- 9	-201	59	
5	- 7	-101	87	
6	- 5	23	45	
7	- 3	129	- 25	
8	- 1	189	- 75	$J = \frac{15}{2}$
9	1	189	- 75	
10	3	129	- 25	
11	5	23	45	
12	7	-101	87	
13	9	-201	59	
14	11	-221	- 39	
15	13	- 91	-117	
16	15	273	65	
1	-12	99	22	
2	-10	- 66	- 55	
3	- 8	- 96	8	
4	- 6	- 54	43	
5	- 4	11	22	
6	- 2	64	- 20	
7	0	84	- 40	$J = 6$
8	2	64	- 20	
9	4	11	22	
10	6	- 54	43	
11	8	- 96	8	
12	10	- 66	- 55	
13	12	99	22	

Table 2.I Continued

$H_{i+3,i} = -\frac{4}{3}\sqrt{2}\cdot C_{4,i}\cdot Wx - \frac{20}{9}\sqrt{2}\cdot C_{5,i}\cdot W\,(1-|x|)$

i	$C_{4,i}$	$C_{5,i}$	
1	$-3\sqrt{455}$	$-2\sqrt{455}$	
2	$-10\sqrt{91}$	$-3\sqrt{91}$	
3	$-4\sqrt{715}$	0	
4	$-30\sqrt{11}$	$7\sqrt{11}$	
5	$-5\sqrt{231}$	$2\sqrt{231}$	
6	$-4\sqrt{105}$	$2\sqrt{105}$	
7	0	0	$J = \frac{15}{2}$
8	$4\sqrt{105}$	$-2\sqrt{105}$	
9	$5\sqrt{231}$	$-2\sqrt{231}$	
10	$30\sqrt{11}$	$-7\sqrt{11}$	
11	$4\sqrt{715}$	0	
12	$10\sqrt{91}$	$3\sqrt{91}$	
13	$3\sqrt{455}$	$2\sqrt{455}$	

$H_{i+3,i} = -\frac{2}{3}\sqrt{2}\cdot C_{4,i}\cdot Wx - \frac{2}{27}\sqrt{2}\cdot C_{5,i}\cdot W\,(1-|x|)$

i	$C_{4,i}$	$C_{5,i}$	
1	$-9\sqrt{55}$	$-84\sqrt{55}$	
2	$-7\sqrt{165}$	$-14\sqrt{165}$	
3	$-50\sqrt{3}$	$175\sqrt{3}$	
4	$-6\sqrt{105}$	$43\sqrt{105}$	
5	$-7\sqrt{10}$	$63\sqrt{10}$	
6	$7\sqrt{10}$	$-63\sqrt{10}$	
7	$6\sqrt{105}$	$-43\sqrt{105}$	$J = 6$
8	$50\sqrt{3}$	$-175\sqrt{3}$	
9	$7\sqrt{165}$	$14\sqrt{165}$	
10	$9\sqrt{55}$	$84\sqrt{55}$	

Table 2.I Continued

$H_{i+6,i} = \frac{4}{9}\sqrt{11}\cdot C_{6,i}\cdot W(1-\lvert x\rvert)$		
i	$C_{6,i}$	
1	$\sqrt{455}$	$J = \frac{15}{2}$
2	$7\sqrt{39}$	
3	$4\sqrt{273}$	
4	84	
5	$42\sqrt{5}$	
6	$42\sqrt{5}$	
7	84	
8	$4\sqrt{273}$	
9	$7\sqrt{39}$	
10	$\sqrt{455}$	
$H_{i+6,i} = \frac{22}{27}\cdot C_{6,i}\cdot W(1-\lvert x\rvert)$		
i	$C_{6,i}$	
1	$2\sqrt{231}$	$J = 6$
2	$7\sqrt{66}$	
3	$14\sqrt{30}$	
4	84	
5	$14\sqrt{30}$	
6	$7\sqrt{66}$	
7	$2\sqrt{231}$	

References of Chapter 2

1. A. Abragam and B. Bleaney, "Electron Paramagnetic Resonance of Transition Ions", (Clarendon Press, Oxford, 1970) Ch. 16.
2. M.T. Hutchings, Solid State Physics 16 (1964) 227.
3. K.R. Lea, M.J.M. Leask and W.P. Wolf, J. Phys. Chem. Solids 23 (1962) 1381.
4. K.W.H. Stevens, Proc. Phys. Soc. Lond. A65 (1952) 209.
5. I.A. Campbell, J. Phys. F2 (1972) L47.
6. E. Merzbacher, "Quantum Mechanics", (John Wiley, New York, 1962) Ch. 15, sec. 9.
7. W.J. Carr in "Handbuch der Physik", Band XVIII/2, ed. H.P.J. Wijn (Springer, Berlin, 1966) p. 281.
8. J.M. Baker, B. Bleaney and W. Hayes, Proc. Roy. Soc. A247 (1958) 141.
9. l.c. ref. 2, p. 270.
10. l.c. ref. 1, Table 16, p. 863.
11. l.c. ref. 1, p. 616.
12. l.c. ref. 1, Ch. 17.
13. l.c. ref. 1, p. 684.
14. l.c. ref. 1, Table 17, p. 864.

CHAPTER 3

THE RELAXATION MODEL

3.1 Introduction

If a trivalent rare-earth ion is implanted into a ferromagnetic metal it can occupy a substitutional or a non-substitutional position in the (cubic) host lattice. The $(2J+1)$-fold degeneracy of the electronic ground state of the ion is removed in different ways in both positions:

A. Substitutional ion

As we have seen in chapter 2, the ground state is split up by two interactions in this case: The host-impurity exchange interaction (see section 2.2) and the cubic crystalline electric field. The second interaction in general leads to a reduction of the hyperfine field and quadrupole splitting as has been discussed in chapter 2, for the case of implants in nickel. In the Mössbauerspectrum of DyFe (see chapter 7) the full ionic splitting is observed at 5 K, so in this case the field reduction by the crystal field can be neglected. Then the exchange field gives rise to $2J+1$ electronic levels at equal distances (see fig. 3.1):

$$\Delta_2 = (g_J - 1)\mu_B H_{exch} \qquad (1)$$

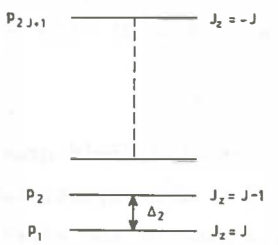

fig. 3.1 Splitting of electronic levels by an exchange field.

At a temperature T of the system the population of these levels is given by a Boltzmann distribution (analogous to 2.7.(2))

$$p_i = \exp\left[-\Delta_2 \cdot (J + 1 - i)/kT\right] \Big/ \sum_{i=1}^{2J+1} \exp\left[-\Delta_2 \cdot (J + 1 - i)/kT\right] \qquad (2)$$

B. Non-substitutional ion

If such an ion is associated with damage (e.g. a vacancy) in the host lattice, its environment has no cubic symmetry. Instead; it is very likely that there is a strong axial component of the crystalline electric field.

Since Dy^{3+} is a Kramers ion (i.e. it has an odd number of 4f electrons), its ground state will be split into doublets [1]. The Mössbauer spectrum of DyFe at 5 K can be fitted with one component with the full ionic splitting. If this component is (partly) generated by non-substitutional Dy^{3+} ions, a doublet with $\langle J_z \rangle = \pm J$ must lie lowest. The doublets may be split up by the exchange interaction, giving the level scheme of fig. 3.2.

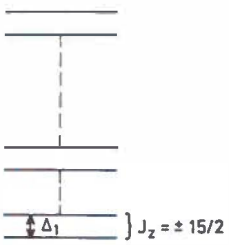

fig. 3.2 Splitting of electronic levels of Dy^{3+} ion in strong axial crystalline electric field, combined with (weak) exchange field.

As Tm^{3+} has an even number of 4f-electrons it is a non Kramers ion. Then in a purely axial symmetric crystal field the J manifold will split up into a singlet $\langle J_z \rangle = 0$, together with J doublets [2]. The Mössbauer spectrum of TmFe (see chapter 10) also shows only one component. The over all splitting of this component is about 7 % smaller than the ionic value. So also for Tm^{3+} it is a reasonable assumption to have a doublet with $\langle J_z \rangle = \pm J$ lying lowest.

Because the hyperfine field and the electric field gradient at the nucleus of the implanted ion depend on the expectation values $\langle J_z \rangle$ and $\langle J_z^2 \rangle$ (see section 2.5), a jump of the electronic energy of the ion between two sublevels will cause a change in hyperfine field and electric field gradient. Such jumps can influence the shape of the Mössbauer spectra of sources of implanted rare earth impurities. This can be illustrated by two extreme cases:

I. "Slow relaxation limit"

The frequency of the jumps is much lower than the Larmor precession frequency of the nucleus. In this case the Mössbauer spectrum is given by:

$$I(\omega) = \sum_k p_k \, I_k \, (\omega) \qquad (3)$$

In this expression $I_k(\omega)$ is the Mössbauer spectrum that would be measured if all the rare-earth ions would be in the k-th electronic substate when emitting a Mössbauer γ-quantum; p_k is the population number of each electronic substate, normalized to $\sum_k p_k = 1$.

II. "Fast relaxation limit"

The jump frequency is much higher than the Larmor precession frequency. Now the hyperfine field or the electric field gradient at all the emitting nuclei will have the same value and a single component Mössbauer spectrum will result, corresponding to a hyperfine field proportional to:

$$\langle J_z \rangle_B \equiv \sum_k p_k \langle J_z \rangle_k \quad \text{(Boltzmann average)} \qquad (4)$$

$\langle J_z \rangle_k$ is the expectation value of J_z in the k-th sublevel (k = 1, 2, ...). This gives the familiar result that the magnetic hyperfine field is proportional to the magnetization.

The quadrupole splitting is proportional to:

$$\sum_k p_k \{3\langle J_z^2 \rangle_k - J(J+1)\} = 3\sum_k p_k \langle J_z^2 \rangle_k - J(J+1) \qquad (5)$$

In the case of the level scheme of fig. 3.1 this fast relaxation will cause a reduction of the hyperfine field and of the quadrupole splitting with rising temperature ($\langle J_z \rangle_k = J - k + 1$). These reductions are given graphically in fig. 3.3.

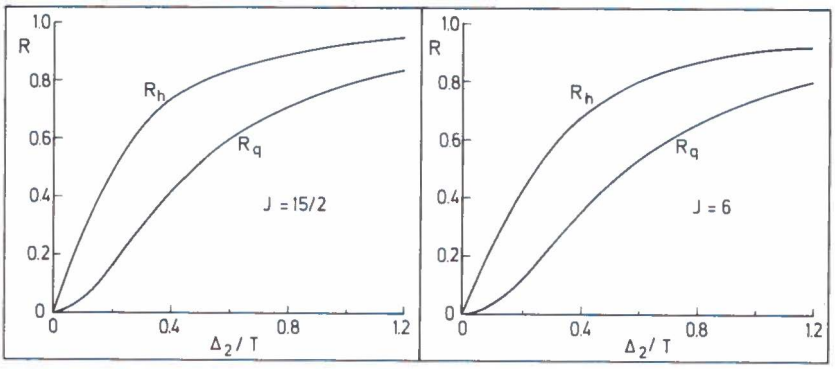

fig. 3.3 Reduction of hyperfine field and quadrupole splitting for electronic levels at equal distances.

In the case of the level scheme of fig. 3.2 fast relaxation will cause the hyperfine field and the quadrupole splitting to vanish when $\Delta_1 = 0$.

When the jump frequency and the Larmor precession frequency are of the same order of magnitude, a complicated Mössbauer spectrum will result.

The relaxation model we have used to calculate theoretical Mössbauer spectra in this case is based on a stochastic theory developed by Anderson [3] to describe the narrowing of spectral lines in magnetic resonance spectroscopy. This theory is also described by Abragam [4], by Kubo [5] and by Nowik [6]. It has been used to treat relaxation phenomena in Mössbauer spectra for the first time by Blume [7] and by Van der Woude and Dekker [8]. An extensive survey of the relaxation theories used in Mössbauer spectroscopy has been given recently by Hartmann-Boutron [9].

By combining an idea of Clauser [10,11] with the stochastic theory, we can derive the expression for a theoretical relaxation spectrum in an elegant way, as will be shown in the next sections.

3.2 The relaxation matrix

Before we come to the stochastic model itself, we will derive some properties of the relaxation matrix Π used in that model, to

enlarge out insight in the relaxation process and to supply ourselves with a valuable mathematical tool, that will also be used in section 3.3.

Consider a system that can be in n states. $p_k(t)$ is the probability to find the system in state k at time t. In other words: If there would be a large number N of these (equal) systems, then $p_k(t) \cdot N$ of them would be in state k at time t.

So $$\sum_{k=1}^{n} p_k(t) = 1 \qquad \text{for all t.} \quad (1)$$

Transitions between the states of the system are possible. The possibility to find the system, being in state k at time t, in state l at time $t + \Delta t$ will be given by: $\pi_{kl} \cdot \Delta t$. This means that the transition process is a stochastic (Markoff) process [12]. In other words: If there would be N of these systems, then $p_k(t) \cdot N \cdot \pi_{kl} \cdot \Delta t$ of these systems would go from state k, where they were at time t, to state l in the time interval $(t, t+\Delta t)$. So in this time interval:

$$\sum_{\substack{l=1 \\ l \neq k}}^{n} p_k(t) \cdot N \cdot \pi_{kl} \cdot \Delta t = p_k(t) \cdot N \cdot \Delta t \cdot \sum_{\substack{l=1 \\ l \neq k}}^{n} \pi_{kl}$$

of the N systems would leave state k where they were at time t, while

$$\sum_{\substack{l=1 \\ l \neq k}}^{n} p_l(t) \cdot N \cdot \pi_{lk} \cdot \Delta t = N \cdot \Delta t \cdot \sum_{\substack{l=1 \\ l \neq k}}^{n} p_l(t) \cdot \pi_{lk}$$

systems would return to state k from another state.

We now return to one system. The possibility to find it in state k at time $t+\Delta t$ is given by:

$$p_k(t+\Delta t) = p_k(t) - \Delta t \cdot p_k(t) \cdot \sum_{\substack{l=1 \\ l \neq k}}^{n} \pi_{kl} + \Delta t \cdot \sum_{\substack{l=1 \\ l \neq k}}^{n} p_l(t) \cdot \pi_{lk}$$

So $$\frac{p_k(t+\Delta t) - p_k(t)}{\Delta t} = - p_k(t) \cdot \sum_{\substack{l=1 \\ l \neq k}}^{n} \pi_{kl} + \sum_{\substack{l=1 \\ l \neq k}}^{n} p_l(t) \cdot \pi_{lk}$$

By letting $\Delta t \to 0$ in this expression we get a set of differential equations:

$$\dot{p}_k(t) = - p_k(t) \cdot \sum_{\substack{l=1 \\ l \neq k}}^{n} \pi_{kl} + \sum_{\substack{l=1 \\ l \neq k}}^{n} p_l(t) \cdot \pi_{lk} \quad (k = 1, \ldots, n) \qquad (2)$$

If we introduce the vectors ("T" means transpose):

$$\underline{\dot{p}}(t) = |\dot{p}_1(t), \ldots, \dot{p}_n(t)|^T \quad , \quad \underline{p}(t) = |p_1(t), \ldots, p_n(t)|^T$$

And the matrix A with

$$\left.\begin{aligned} a_{kl} &= \pi_{lk} \quad (l \neq k) \\ a_{kk} &= - \sum_{\substack{l=1 \\ l \neq k}}^{n} \pi_{kl} \end{aligned}\right\} \qquad (3)$$

then (2) can be written as:

$$\dot{\underline{p}}(t) = A \cdot \underline{p}(t) \qquad (4)$$

(From (3) we can derive that $\Pi = A^T$).

To find a general solution of (4) we proceed as follows: Let λ_i and $\underline{a}_i$ be the eigenvalues and eigenvectors of A:

$$A\underline{a}_i = \lambda_i \underline{a}_i \qquad (5)$$

and let $\underline{b}_i$ be the eigenvector of the transpose of A belonging to the same eigenvalues

$$A^T \underline{b}_i = \lambda_i \underline{b}_i \qquad (6)$$

(A matrix and its transpose have the same eigenvalues). $\underline{b}_i$ is called a left eigenvalue of A because

$$\underline{b}_i^T \cdot A = \lambda_i \underline{b}_i^T \qquad (7)$$

Now consider a left and a right eigenvector of A belonging to different eigenvalues:

$$\left.\begin{aligned} A\underline{a}_i &= \lambda_i \underline{a}_i \\ \underline{b}_j^T A &= \lambda_j \underline{b}_j^T \end{aligned}\right\} \tag{8}$$

From this we get:

$$\left.\begin{aligned} \underline{b}_j^T A\underline{a}_i &= \lambda_i \underline{b}_j^T \underline{a}_i \\ \underline{b}_j^T A\underline{a}_i &= \lambda_j \underline{b}_j^T \underline{a}_i \end{aligned}\right\} \tag{9}$$

So

$$(\lambda_i - \lambda_j)\, \underline{b}_j^T \underline{a}_i = 0 \tag{10}$$

which gives

$$\underline{b}_j^T \underline{a}_i = 0 \tag{11}$$

since $\lambda_i \neq \lambda_j$.

If we now normalize $\underline{a}_i$ and $\underline{b}_i$:

$$\underline{b}_j^T \underline{a}_i = 1 \tag{12}$$

we can introduce a set of orthogonal matrices (see proof 3.I):

$$M_i = \underline{a}_i \cdot \underline{b}_i^T \tag{13}$$

and A can be written as (see proof 3.II):

$$A = \sum_i \lambda_i M_i \tag{14}$$

Now it can easily be verified that

$$\underline{p}_1(t) = \{\sum_i e^{\lambda_i t} M_i\} \cdot \underline{p}(0) \tag{15}$$

is a solution of (4) (see proof 3.III).

A is a real matrix. Then from (14):

$$A^* = A = \sum_i \lambda_i^* M_i^* \tag{16}$$

("*" means: complex conjugate; if $z = a + bi$ then $z^* = a - bi$).

So $$\underline{p}_2(t) = \{\sum_i e^{\lambda_i^* t} M_i^*\}\ \underline{p}(0) \qquad (17)$$

is also a solution (4) and we can get a general real solution of (4) by taking

$$\underline{p}(t) = \tfrac{1}{2}\underline{p}_1(t) + \tfrac{1}{2}\underline{p}_2(t) \ .$$

By introducing $\lambda_i = \mu_i + i\sigma_i$ and $M_i = P_i + iQ_i$ this solution can be written as:

$$\underline{p}(t) = \{\sum_i e^{\mu_i t}\ (\cos \sigma_i t \cdot P_i - \sin \sigma_i t \cdot Q_i)\}\ \underline{p}(0) \qquad (18)$$

Proof 3.I: $M_i M_j = (\underline{a}_i \underline{b}_i^T)\ (\underline{a}_j \underline{b}_j^T) = \underline{a}_i (\underline{b}_i^T \underline{a}_j) \underline{b}_j^T$ (using (11))

$M_i^2 = (\underline{a}_i \underline{b}_i^T)\ (\underline{a}_i \underline{b}_i^T) = \underline{a}_i (\underline{b}_i^T \underline{a}_i) \underline{b}_i^T = \underline{a}_i \underline{b}_i^T = M_i$ (using (12))

Proof 3.II: $\sum_i \lambda_i M_i = \sum \lambda_i \underline{a}_i \underline{b}_i^T = \sum_i A \underline{a}_i \underline{b}_i^T = A \sum_i \underline{a}_i \underline{b}_i^T = A \sum_i M_i = A$

because $M_j \cdot \sum_i M_i = M_j^2 = M_j$ for all j (see proof I)

So $\sum_i M_i = I$ (unit matrix)

Proof 3.III: If $\underline{p}_1(t) = \{\sum_i e^{\lambda_i t} M_i\} \cdot \underline{p}(0)$ then

$\dot{\underline{p}}_1(t) = \{\sum_i \lambda_i\ e^{\lambda_i t} M_i\} \cdot \underline{p}(0)$

And $A\underline{p}(t) = \{\sum_i \lambda_i M_i\}\ \{\sum_i e^{\lambda_i t} M_i\} \cdot \underline{p}(0) = \{\sum_i \lambda_i e^{\lambda_i t} M_i\}\ \underline{p}(0)$

because of the orthogonality relations given in proof I, so then $\dot{\underline{p}}_1(t) = A\ \underline{p}_1(t)$

From (3) we see that the sum of the rows of A is zero. So the determinant of A is zero. Then A has an eigenvalue $\lambda_1 = 0$, with corresponding real left and right eigenvectors $\underline{b}_1$ and $\underline{b}_2$. Then (18) can be written as:

$$\underline{p}(t) = \underline{a}_1 \cdot \underline{b}_1^T \cdot \underline{p}(0) + \{ \sum_{i=2}^{n} e^{\mu_i t} (\cos \sigma_i t \cdot P_i - \sin \sigma_i t \cdot Q_i \} \cdot \underline{p}(0) \quad (19)$$

As $\mu_i < 0$ in this expression (see proof 3.IV), a final stationary occupation

$$\underline{p}(\infty) = \underline{a}_1 \cdot \underline{b}_1^T \cdot \underline{p}(0) \quad (20)$$

is reached if $t \to \infty$. By multiplying the right side of (19) by the unit vector $\underline{1}$ it can be shown that condition (1) is fulfilled (see proof 3.V).

From (19) we can see that the occupation of the k-th state (k arbitrary) behaves like a damped oscillation round the final stationary occupation $p_k(\infty)$.

A special case occurs if $\pi_{kl} = \pi_{lk}$. (The probability to jump from state k to state l is the same as that for a jump from l to k). Then A is symmetric real matrix, so all its eigenvalues and eigenvectors are real and (19) reduces to:

$$\underline{p}(t) = \underline{a}_1 \cdot \underline{b}_1^T \cdot \underline{p}(0) + \{ \sum_{i=2}^{n} e^{\lambda_i t} M_i \} \cdot \underline{p}(0) \quad (21)$$

in which λ_i is a real, negative number and M_i is a real matrix. In this case the final occupation of the states is reached without oscillations.

Proof 3.IV: In the set of equations $\underline{b}_i^T A = \lambda_i \underline{b}_i^T$ (7), the absolute value $|b_{ik}| = (b_{ik}^* \cdot b_{ik})^{\frac{1}{2}}$ of the element b_{ik} is larger than or equal to the absolute values of the ohter elements of $\underline{b}_i$. The k^{th} equation of (7) is:

$$\sum_{\substack{j=1 \\ j \neq k}}^{n} b_{ij} \cdot \pi_{jk} + \pi_{kk} \cdot b_{ik} = \lambda_i \cdot b_{ik} \quad (22)$$

From this we can deduce:

$$\sum_{\substack{j=1 \\ j \neq k}}^{n} \mathrm{Re} \{ \frac{b_{ij}}{b_{ik}} \} \cdot \pi_{jk} + \pi_{kk} = \mathrm{Re}\{\lambda_i\} = \mu_i \quad (23)$$

and from the assumption about $|b_{ik}|$ we can derive:

$$-1 \leq \mathrm{Re}\{\frac{b_{ij}}{b_{ik}}\} \leq 1 \qquad (24)$$

Combining this with $\pi_{kk} = -\sum_{\substack{j=1 \\ j\neq k}}^{n} \pi_{jk}$ (see (3)) yields: $\mu_i \leq 0$.

Proof 3.V: $\left.\begin{array}{l} \underline{A}\underline{a}_i = \lambda_i \underline{a}_i \quad (5) \\ \underline{1}^T A = 0 \text{ (see (3))} \end{array}\right\}$ $\quad \underline{1}^T \cdot \underline{a}_i = 0$ if $\lambda_i \neq 0$.

Then $\underline{1}^T M_i = \underline{1}^T \underline{a}_i \cdot \underline{b}_i^T = 0$.

So $\underline{1}^T(P_i + iQ_i) = 0$ then $\underline{1}^T P_i = 0 \qquad (25)$

and $\underline{1}^T Q_i = 0 \qquad (26)$

Because $\lambda_i = 0$: $\underline{b}_1^T A = 0$; also $\underline{1}^T A = 0$. So $\underline{b}_1$ can be chosen to be the unit vector $\underline{1}$, but then because of (12): $\underline{1}^T \cdot \underline{a}_1 = 1$ and

$$\underline{1}^T \underline{a}_1 \cdot \underline{b}_1^T \underline{p}(0) = \underline{1}^T \cdot \underline{p}(0) = 1 \qquad (27)$$

as $\Sigma p_k(0) = 1$.

Multiplying the left and the right side of (19) by $\underline{1}^T$ and substituting (25), (26) and (27) gives $\underline{1}^T \cdot \underline{p}(t) = 1$ for all t, so $\Sigma p_k(t) = 1$ for all t.

3.3 The relaxation model

To derive an expression for a Mössbauer spectrum showing relaxation effects, we will use a model based on the so-called "rate equation method". A clear, comprehensive derivation of the formula:

$$I(\omega) = Re\ (\underline{W}^T A^{-1} \underline{1}) \qquad (1)$$

that describes the Mössbauer spectrum in that model that is given by Nowik [6]. We will use Nowik's notation, but we follow a different procedure, based on an idea of Clauser [10]. In this way we can derive an expression for $I(\omega)$ different from (1), that

gives a better insight in the structure of the spectrum and makes its computation go much faster.

The assembly of nuclei making a gamma transition from the excited state to the ground state can be looked upon as a system of damped harmonic oscillators. The time dependence of the amplitude of such an oscillator is given by

$$\dot{G}_k(t) = (-\Gamma + i\omega_k)\, G_k(t) \tag{2}$$

in which $\hbar\omega_k$ is the energy of the γ transition, $\frac{1}{2\Gamma}$ the mean lifetime of the excited state and $G_k(0) = p_k$ (see section 3.1).

The frequency distribution of the emitted gamma rays will be given by:

$$I_k(\omega) = Re \int_0^\infty G_k(t) \cdot e^{-i\omega t}\, dt \tag{3}$$

In the relaxation process, jumps as described in section 3.2 are possible from oscillatory state k (frequency ω_k) to oscillatory state l (frequency ω_l). The total Mössbauer spectrum is then given by (see also section 3.8):

$$I(\omega) = Re \int_0^\infty G(t)\, e^{-i\omega t}\, dt \tag{4}$$

in which

$$G(t) = \sum_k G_k(t) \tag{5}$$

If we write

$$\underline{G}^T = (G_1(t), G_2(t), \ldots\ldots), \tag{6}$$

the function $G(t)$ can be found from the set of differential equations |4|:

$$\dot{\underline{G}}^T = \underline{G}^T\, (-\Gamma I + i\Omega + \Pi) \tag{7}$$

where I is the unit matrix, $\Omega_{kl} = \omega_k \delta_{kl}$ and Π is the relaxation matrix with elements π_{kl} that have the same meaning as in section 3.2.

We will solve (7) by introducing a matrix P given by:

$$P = \Pi + i\Omega \tag{8}$$

In the same way as in section 3.2, P can be written as:

$$P = \sum_i \lambda_i M_i \tag{9}$$

with $P\underline{a}_i = \lambda_i \underline{a}_i$; $P^T \underline{b}_i = \lambda_i \underline{b}_i$; $M_i = \underline{a}_i \underline{b}_i^T$; $\underline{a}_i^T \cdot \underline{b}_i = 1$. The solution of (7) can now be written as:

$$\underline{G}^T(t) = \underline{G}^T(0) \cdot \sum_i e^{(\lambda_i - \Gamma)t} \cdot M_i \tag{10}$$

This can easily be verified using the orthogonality of the M_i (see proof 3.VI).

Proof 3.VI: If $\underline{G}^T(t) = \underline{G}^T(0) \sum_i e^{(\lambda_i - \Gamma)t} \cdot M_i$ then

$\dot{\underline{G}}^T(t) = \underline{G}^T(0) \sum_i (\lambda_i - \Gamma) e^{(\lambda_i - \Gamma)t} \cdot M_i$

Now $\underline{G}^T(0) \cdot \sum_i \Gamma e^{(\lambda_i - \Gamma)t} \cdot M_i = \Gamma \cdot \underline{G}^T(0) \cdot \sum_i e^{(\lambda_i - \Gamma)t} \cdot M_i = \Gamma \cdot G^T(t)$

and $\underline{G}^T(0) \sum_i \lambda_i e^{(\lambda_i - \Gamma)t} \cdot M_i = \underline{G}^T(0) \cdot \sum_i e^{(\lambda_i - \Gamma)t} \cdot M_i \sum_j \lambda_j M_j =$

$\underline{G}^T(t) \cdot \sum_j \lambda_j M_j = G^T(t) \cdot P$. So $\dot{G}^T(t) = \underline{G}^T(t)\ (-\Gamma I + P)$

Combining (5) and (10) we get:

$$G(t) = \sum_i \gamma_i e^{(\lambda_i - \Gamma)t} \tag{11}$$

with

$$\gamma_i = \underline{W}^T M_i \underline{1} \tag{12}$$

and

$$\underline{W}^T = (p_1, p_2, \ldots\ldots, p_n) \tag{13}$$

The lineshape of the emitted spectrum will be given by:

$$I(\omega) = Re \int_0^\infty \sum_i \gamma_i e^{(\lambda_i - \Gamma - i\omega)t}\, dt \tag{14}$$

Integration gives:

$$I(\omega) = Re\ \{\sum_i \frac{-\gamma_i}{\lambda_i - \Gamma - i\omega}\} \tag{15}$$

Or, if we write: $\lambda_i = -\Gamma_i + i\omega_i$
and $\lambda_i = \alpha_i + i\beta_i$ (16)

then $$I(\omega) = -\sum_i \frac{\alpha_i(\Gamma+\Gamma_i)^2 + \beta_i(\omega-\omega_i)}{(\omega-\omega_i)^2 + (\Gamma+\Gamma_i)^2} \tag{17}$$

We see from (17) that the real part of the eigenvalues λ_i of the matrix P gives information about the broadening ($\Gamma_i \geq 0$; see proof 3.VII) and the imaginary part of the λ_i about the position in the relaxation spectrum. The α_i and β_i are intensity parameters.

Proof 3.VII: Ω is a diagonal matrix. (With elements Ω_{ij}). So the k-th equation of the set $P\underline{a}_i = \lambda_i \underline{a}_i$ is:

$$\sum_{\substack{j=1 \\ j\neq k}}^{n} \pi_{kj} \cdot a_{ij} + \pi_{kk} \cdot a_{ij} + i\pi_{kk} \cdot a_{ik} = \lambda_i \cdot a_{ij} \tag{18}$$

(a_{ij} is the j-th element of $\underline{a}_i$).
Or after division by a_{ij}:

$$\sum_{\substack{j=1 \\ j\neq k}}^{n} \pi_{kj} \left(\frac{a_{ij}}{a_{ik}}\right) + \pi_{kk} + i\Omega_{kk} = \lambda_i$$

and $$Re\{\lambda_i\} = -\Gamma_i = \sum_{\substack{j=1 \\ j\neq k}}^{n} \pi_{kj}\ Re\ \left(\frac{a_{ij}}{a_{ik}}\right) + \pi_{kk} \tag{19}$$

As this is the same expression as 3.2.(22) and as Π is constructed in the same way as A^T, we can proceed in the same way as in proof 3.IV to show that $Re\{\lambda_i\} \leq 0$ or $\Gamma_i \geq 0$.

In Nowik's final expression for the spectrum:

$$I(\omega) = Re\ \{\underline{W}^T A^{-1} \underline{1}\} \tag{20}$$

the elements of the matrix A depend on ω. So to compute the spectrum using this expression, one has to invert A for each different value of ω. Since the elements of matrix P do not depend on ω, one has to compute its eigenvalues λ_i and eigenvectors M_i only once to find a spectrum, using our expression (17). This saves much computer time [11].

3.4 A simple two-level example

As an illustration of the theory described in the preceding section, we will now calculate the Mössbauer spectrum for one nuclear transition in the case of two electronic levels.

The energy of the nuclear transition will be $\hbar\omega_1$ in the case that the lower electronic level is occupied and $\hbar\omega_2$ in the case that the upper level is occupied. The population of the levels is given by p_1 and p_2 subsequently. The relaxation matrix can then be written as:

$$\Pi = \pi_0 \begin{bmatrix} -\alpha & \alpha \\ 1 & -1 \end{bmatrix} \tag{1}$$

with $\alpha = \frac{p_1}{p_2}$; π_0, the relaxation "frequency", is a constant.
The position matrix Ω is given by:

$$\Omega = \begin{bmatrix} \omega_1 & 0 \\ 0 & \omega_2 \end{bmatrix} \tag{2}$$

If we shift the frequency scale by an amount $\frac{\omega_1+\omega_2}{2}$ and introduce $\delta = \frac{\omega_1+\omega_2}{2}$ (fig. 3.4) the Ω-matrix becomes:

$$\Omega = \begin{bmatrix} \delta & 0 \\ 0 & -\delta \end{bmatrix} \tag{3}$$

and the matrix P becomes:

$$P = \begin{bmatrix} -\alpha\pi_0 + i\delta & \alpha\pi_0 \\ \pi_0 & -\pi_0 - i\delta \end{bmatrix} \tag{4}$$

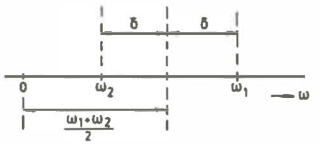

fig. 3.4 Frequency scale for two level example.

This can be simplified by introducing the dimensionless constant:

$$\pi = \frac{\pi_0}{\delta} \tag{5}$$

giving:

$$P = \delta \begin{bmatrix} -\alpha\pi + i & \alpha\pi \\ \pi & -\pi - i \end{bmatrix} = \delta P' \tag{6}$$

Using the fact that P' and P have the same eigenvectors, while the eigenvalues of P are δ times those of P', it can easily be shown using 3.3.(17) for $I(\omega)$, that we can as well calculate the spectrum starting from P', if we introduce the dimensionless variables: $\Gamma' = \frac{\Gamma}{\delta}$ and $\omega' = \frac{\omega}{\delta}$.

Summarized:

We will calculate theoretical spectra starting from

$$P' = \begin{bmatrix} -\alpha\pi + i & \alpha\pi \\ \pi & -\pi - i \end{bmatrix} \tag{7}$$

with $\alpha = \frac{p_1}{p_2}$ and $\pi = \frac{\pi_0}{\delta}$; also using $\Gamma' = \frac{\Gamma}{\delta}$ and $\omega' = \frac{\omega}{\delta}$.

The eigenvalues λ_1 and λ_2 of P' can be calculated from:

$$\lambda^2 - tr\, P' \cdot \lambda + det\, P' = 0 \tag{8}$$

in which $tr\ P'$ and $det\ P'$ are the trace and the determinant of P' respectively.

So

$$\lambda_1 + \lambda_2 = -(\alpha+1)\cdot\pi \tag{9}$$

and

$$\lambda_1\cdot\lambda_2 = 1 + i\pi(\alpha-1) \tag{10}$$

P' can be written as:

$$P' = \lambda_1 M_1 + \lambda_2 M_2 \tag{11}$$

so

$$\underline{W}^T P' \underline{1} = \lambda_1\gamma_1 + \lambda_2\gamma_2 \tag{12}$$

with $\underline{W}^T = [p_1,\ p_2]$ and $\gamma_i = \underline{W}^T M_i \underline{1}$.

From (7) we can easily calculate:

$$\underline{W}^T P' \underline{1} = i(p_1 - p_2) \tag{13}$$

Then from (12) and (13):

$$\lambda_1\gamma_1 + \lambda_2\gamma_2 = i(p_1 - p_2) \tag{14}$$

Since $\Sigma M_i = I$:

$$\gamma_1 + \gamma_2 = 1 \tag{15}$$

For some special cases the calculation of the spectrum is now straightforward:

I. Slow relaxation, $\pi = 0$.

Then

$$P' = \begin{bmatrix} i & 0 \\ 0 & -i \end{bmatrix} \qquad \text{with } \gamma_{1,2} = \pm i$$

and

$$M_1 = \begin{bmatrix} 1 & 0 \\ 0 & 0 \end{bmatrix} \quad ; \quad M_2 = \begin{bmatrix} 0 & 0 \\ 0 & 1 \end{bmatrix}$$

so $\gamma_1 = p_1$ and $\gamma_2 = p_2$.

The spectrum is given by:

$$I(\omega) = -\frac{p_1\Gamma'}{(\omega'-1)^2 + (\Gamma')^2} - \frac{p_2\Gamma'}{(\omega'+1)^2 + (\Gamma')^2} \qquad (16)$$

This gives two unbroadened lines at positions $\omega' = \pm 1$ with intensity ratio $p_1 : p_2$, as we expect for this case.

II. Fast relaxation, $\pi \to \infty$

Using (9) we can write:

$$\lambda_1 = -\pi(\alpha+1) - x - iy$$
$$\lambda_2 = \qquad x + iy$$

in which x and y are real numbers.

Then

$$Re\{\lambda_1 \cdot \lambda_2\} = -(\alpha+1)\pi x - x^2 + y^2$$
$$Im\{\lambda_1 \cdot \lambda_2\} = -(\alpha+1)\pi y - 2xy$$

Combining this with (10) we get:

$$-(\alpha+1)\cdot\pi x - x^2 + y^2 = 1$$
$$-(\alpha+1)\cdot\pi y - 2xy = \pi(\alpha-1)$$

If $\pi \to \infty$ these two relations can only hold if $x \to 0$. (Then $y \to \frac{1-\alpha}{1-\alpha} = p_1 - p_2$). So for $\pi \to \infty$ the eigenvalues of P' are:

$$\lambda_1 = -\pi(\alpha+1) - i(p_1 - p_2) \quad ; \quad \lambda_2 = i(p_1 - p_2)$$

Substituting these values in (14) and (15) we get:

$$\gamma_1 = 0 \qquad , \qquad \gamma_2 = 1.$$

The expression for the spectrum becomes:

$$I(\omega) = -\frac{\Gamma'}{\{\omega' - (p_1-p_2)\}^2 + (\Gamma')^2} \qquad (17)$$

This gives only one unbroadened line at the position:

$$\omega' = p_1 - p_2 \quad \text{or} \quad \omega = p_1\omega_1 + p_2\omega_2 \quad \text{(see fig. 2.4)}$$

This position is the Boltzmann-average of the positions ω_1 and ω_2, as we expect for this case.

III Very low temperature ($p_2 = 0$)

As $p_2 = 0$, $p_1 = 1$ and $\alpha = 0$.

Then $$P' = \begin{bmatrix} i & 0 \\ \pi & -\pi - i \end{bmatrix}$$ so $\lambda_1 = i$ and $\lambda_2 = -\pi - i$

With (14) and (15) we get: $\gamma_1 = 1$, $\gamma_2 = 0$ and the expression for the spectrum is:

$$I(\omega') = - \frac{\Gamma'}{(\omega'-1)^2 + (\Gamma')^2} \qquad (18)$$

This gives one unbroadened line at position $\omega' = 1$ or $\omega = \omega_1$, as we expect for this case.

To show the influence of the different parameters on the shape of the spectrum in cases where its calculation is not straightforward we have computed some spectra by computer in this simple two-level case. The results are given in fig. 3.5 for the cases $\alpha = 0.2$ and $\alpha = 0.5$ with $\Gamma' = 0.1$. The results of these computer calculations for the cases $\pi = 0$ and $\pi = \infty$ agree with the results obtained by the straightforward calculations given above.

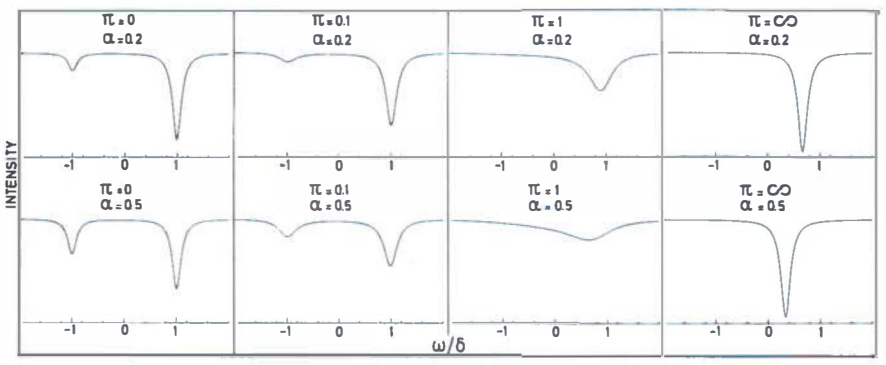

fig. 3.5 Relaxation spectra for two electronic levels ($\Gamma' = 0.1$)

We see from fig. 3.5 that if π becomes larger, starting at $\pi = 0$, at first the lines broaden ($\pi = \Gamma'$) while their position hardly changes. Then the two lines change into one broad line for $\pi \sim 1$; this means that π_0 has the same order of magnitude as ω_1 and ω_2. Finally, for very large values of π the width of this single line reduces to Γ' [13].

3.5 Relaxation spectra of Dy and Tm in the case of two electronic levels

We have written a computer program to calculate relaxation spectra for Dy and Tm with the model given in section 3.4. We assume the electronic level scheme to be that of fig. 3.2 with only the two lowest levels ($\langle J_z \rangle = \pm J$) populated. For a specific value of $\langle J_z \rangle$ the positions of the lines in the 16 line Mössbauer spectrum of ^{161}Dy is given by the hamiltonian:

$$\mathcal{H} = -g_N \mu_N H_{hf}(J_z) \cdot \left(\frac{g_N^*}{g_N} I_z^* - I_z\right) + \tfrac{1}{4} e^2 q(J_z) Q \cdot \left\{\frac{Q^*}{Q} \frac{3(I_z^*)^2 - I^*(I^*+1)}{I^*(2I^*-1)} - \frac{3I_z^2 - I(I+1)}{I(2I-1)}\right\} \quad (1)$$

that of the 6 line spectrum of ^{169}Tm by:

$$\mathcal{H} = -g_N \mu_N H_{hf}(J_z) \cdot \left(\frac{g_N^*}{g_N} I_z^* - I_z\right) + \tfrac{1}{4} e^2 q(J_z)\, Q^* \left\{\frac{3(I_z^*)^2 - I^*(I^*+1)}{I^*(2I^*-1)}\right\} \quad (2)$$

(For this nucleus there is no quadrupole splitting of the ground state).

$H_{hf}(J_z)$ is supposed to be proportional to $\langle J_z \rangle$ (see 1.3.(2)), whereas $q(J_z)$ is taken proportional to $3\langle J_z^2 \rangle - J(J+1)$ (see 1.3.(4)). For each line the resulting relaxation spectrum is calculated separately if $\langle J_z \rangle$ jumps between $+J$ and $-J$, just as in section 3.4.

The relaxation spectra obtained in this way (16 for Dy; 6 for Tm) are summed to give the total Mössbauer spectrum.

The results of these calculations for different values of the relaxation frequency (π_0) and the relative population of the two electronic levels (α) are given in fig. 3.6 for Dy and in fig. 3.7 for Tm.

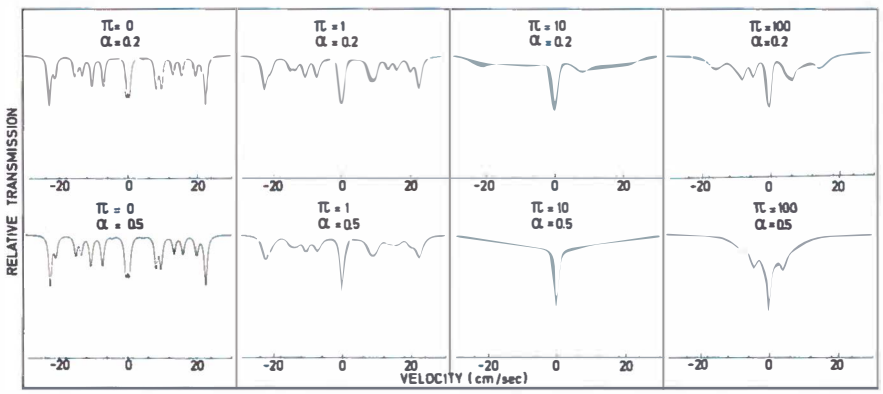

fig. 3.6 Two level relaxation spectra of ^{161}Dy. (Γ = 0.5 cm/sec)

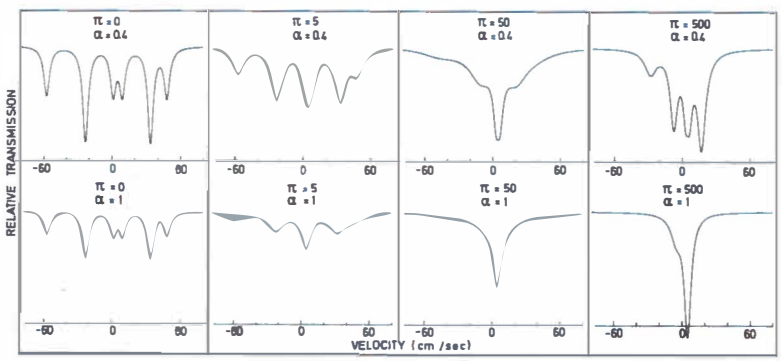

fig. 3.7 Two level relaxation spectra of ^{169}Tm. (Γ = 3 cm/sec)

The values substituted in the model for $g_N \mu_N H_{hf}$, for $\frac{1}{4}e^2qQ$, for the relative intensity and for the width of the lines are those obtained from the measured spectra of DyFe (see section 7.3) and TmFe (see section 7.5) at 5 K. At this temperature only the lowest electronic level is populated, so the calculated spectra in fig. 3.6.a and e and fig. 3.7.a and e are equal to those 5 K spectra. (If one bears in mind that for a zero quadrupole splitting and for one specific value of J_z the spectra of Dy and Tm are symmetric with respect to their center, one can test ones understanding of the relaxation model by proving the last statement).

The parameters π_0 and Γ are given in cm/sec (Γ is the half width at half maximum of an unbroadened line; see 3.3.(17)).

3.6 Relaxation spectra for Dy and Tm for $2J+1$ equidistant electronic levels

In calculating relaxation spectra for ^{161}Dy and ^{169}Tm assuming the electronic energy level scheme of fig. 3.1, we can use the same method as in the preceeding section [14].

If we describe the m-th line in the Mössbauer spectrum by $I(m,\omega)$, the complete spectrum is given by:

$$I(\omega) = \sum_{m=1}^{2J+1} I(m,\omega) \qquad (1)$$

Since the matrix Ω in 3.3.(8) now depends on m, we get

$$P(m) = \Pi + i\Omega(m) \qquad (2)$$

$I(m,\omega)$ can be calculated using 3.3.(17) if the eigenvectors and eigenvalues of $P(m)$ are calculated first.

In such a calculation $\underline{W}(m)$ is given by:

$$\underline{W}^T(m) = C(m) \left[p_1, p_2, \ldots\ldots, p_{2J+1}\right] \qquad (3)$$

where $C(m)$ is the nuclear transition probability, while the p_i are given by 3.1.(2). Also the line width Γ depends on m now.

The elements of $\Omega(m)$ are:

$$\Omega_{kl}^{(m)} = \omega_k^{(m)} \cdot \delta_{kl} \quad (k = 1, \ldots\ldots, 2J+1) \tag{4}$$

In the last expression $\omega_k^{(m)}$ is the frequency of the m-th Mössbauer transition for a given value of

$$J_z = J - k + 1 \tag{5}$$

So $\omega_k^{(m)}$ gives the m-th line in the Mössbauer spectrum for a specific value of J_z given by (5). This position van be calculated from the hamiltonians (1) or (2) in section 3.5, if just as in that section $H_{hf}(J_z)$ and $q(J_z)$, are taken proportional to J_z and $3J_z^2 - J(J+1)$, respectively.

If the rare-earth electron spin relaxes via the conduction electrons (i.e. through the off-diagonal elements of the s-f interaction [15]) the transition probabilities π_{kl}, being the elements of the matrix Π, are given by:

$$\pi(J_z \rightarrow J_z+1) = (2kD)^{-1} \cdot \left[J(J+1) - J_z(J_z+1)\right] \cdot \Delta/(exp(\Delta/kT) - 1)$$

$$\pi(J_z+1 \rightarrow J_z) = (2kD)^{-1} \cdot \left[J(J+1) - J_z(J_z+1)\right] \cdot \Delta/(1 - exp(-\Delta/kT))$$

$$\pi(J_z \rightarrow J_z) = -\left[\pi(J_z \rightarrow J_z-1) + \pi(J_z \rightarrow J_z+1)\right] \tag{6}$$

All other π_{kl} are zero. (The matrix Π with these elements π_{kl} indeed has the properties of the relaxation matrix described in section 3.2, as can easily be verified).

This is analogous to the Korringa relaxation of nuclear spins in a metal, but without the approximation that the energies associated with the spin flips are small compared to kT |16|.

The Korringa-like constant D, given by

$$D^{-1} = (4\pi/h)\ (g_J-1)^2\ J^2_{sf} \cdot \rho^2 \cdot k \tag{7}$$

is a parameter in the model. Here $\rho = \rho(E_F)$ is the density of states per atom per spin of the host at the Fermi level. The other

parameter is Δ_2, the distance between the electronic levels (see fig. 3.1).

3.7 Area of relaxation spectrum

If radioactive ions occupy different non-equivalent positions in a lattice, the Mössbauer spectrum will in general consist of as many different components as there are non-equivalent fractions. If one wishes to compare the intensities of these components it is necessary to be able to calculate the area of such a component:

$$A = \int_0^\infty I(\omega)\, d\omega$$

We will do this for a component, the m-th line of which is given by 3.3.(17):

$$A(m) = \sum_i \int_{-\infty}^{\infty} \frac{\alpha_i(\Gamma+\Gamma_i) + \beta_i(\omega-\omega_i)}{(\omega-\omega_i)^2 + (\Gamma+\Gamma_i)^2} \qquad (1)$$

Or, with the abbreviations $\Gamma + \Gamma_i = a$ and $\omega - \omega_i = x$;

$$A(m) = \sum_i \{\alpha_i a \int_{-\infty}^{\infty} \frac{dx}{x^2+a^2} + \beta_i \int_{-\infty}^{\infty} \frac{x\cdot dx}{x^2+a^2}\} \qquad (2)$$

The first integral (2) is equal to $\frac{\pi}{a}$, the second integral vanishes, as its integrand is an odd function of x.
So (2) reduces to:

$$A(m) = \pi \cdot \sum_i \alpha_i \qquad (3)$$

Because $\sum_i \alpha_i = C(m)$,

$$A(m) = C(m) \cdot \pi \qquad (4)$$

and the total area of the component is given by

$$A = \pi \cdot \sum_m C(m) \qquad (5)$$

Proof 3.VIII $\Sigma\alpha_i + i\Sigma\beta_i = \Sigma\gamma_i = \Sigma \underline{W}^T \underline{M}_i \underline{1} = \underline{W}^T \cdot \Sigma \underline{M}_i \cdot \underline{1} = \underline{W}^T \cdot I \cdot \underline{1} = \Sigma W_j$

W_j are the elements of $\underline{W}$.

(For the meaning of α_i, β_i, γ_i etc. see section 3.3).

Since $\underline{W}^T = C(m) \cdot (p_1, p_2, \ldots, p_n)$ and $\Sigma P_j = 1$ (p_j is the probability that the j-th level is occupied), $\Sigma W_j = C(m)$. $C(m)$ is a real number, so $\Sigma\alpha_i = C(m)$ and $\Sigma\beta_i = 0$.

3.8 Electronic rearrangement

According to Stöhr et al. [17] and Hirst [13,18] relaxed Mössbauer spectra for a source and an absorber experiment with the same isotope may be different. (In the first case a single line absorber is used to measure hyperfine interactions of radioactive nuclei in the source; in the second case a single line source is used to measure hyperfine interactions in the absorber).

In a source experiment with ^{161}Dy or ^{169}Tm recoilless gamma emission takes place after β-decay of ^{161}Tb or ^{169}Er, respectively. After the β-decay an electronic rearrangement of the rare earth ion occurs. Because of this rearrangement the initial population of the electronic energy levels in a source experiment is different from the thermal equilibrium Boltzmann population, but in an absorber experiment, there is an equilibrium population.

One of the possible consequences of this difference in initial population is that contributions from excited electronic states persist also if the temperature goes to zero, in a source spectrum, whereas in the corresponding absorber spectrum these contributions vanish at zero temperature.

According to Stöhr [19] the only change necessary in the stochastic relaxation theory described in the previous sections is to replace the vector $\underline{W}(m)$ (see 3.6.(3)) by

$$\underline{W}'(m) = \frac{C(m)}{2J+1} \cdot \underline{1} \qquad (1)$$

meaning that the initial populations of all electronic states are assumed to be equal.

We replaced $\underline{W}$ by $\underline{W}'$ in our computer programs to calculate relaxation spectra at 5 K for ^{161}Dy and ^{169}Tm, but the results proved to be without physical meaning.

We will show this for a simple two level example, with a straightforward calculation, using the model of section 3.4:

As the initial populations must be equal: $p_1 = p_2 = \frac{1}{2}$. At very low temperatures only jumps from the upper level to the lower level are allowed; so $\alpha = 0$. (The ions do not have enough thermal energy for a jump upward).

Matrix P' is the same as in example III of section 3.4, so its eigenvalues are $\lambda_1 = i$ and $\lambda_2 = -\pi - i$. From $\lambda_1\gamma_1 + \lambda_2\gamma_2 = i(p_1 - p_2)$ and $\gamma_1 + \gamma_2 = 1$ we get:

$$\gamma_1 = \frac{\pi^2 + 2 - i\pi}{\pi^2 + 4} \qquad \gamma_2 = \frac{2 + i\pi}{\pi^2 + 4}$$

This means that at a very low temperature the spectrum is given by:

$$I(\omega') = -\frac{\frac{\pi^2 + 2}{\pi^2 + 4} \cdot \Gamma' - \pi(\omega' - 1)}{(\omega' - 1)^2 + (\Gamma')^2} - \frac{\frac{2}{\pi^2 + 4}(\Gamma' + \pi) + \pi(\omega' + 1)}{(\omega' + 1)^2 + (\Gamma' + \pi)^2} \qquad (2)$$

This spectrum is indeed different from the single line we got in example III, section 3.4 (the absorber case).

However, the dispersion terms

$$\frac{\omega' - 1}{(\omega' - 1)^2 + (\Gamma')^2} \qquad \frac{\omega' + 1}{(\omega' + 1)^2 + (\Gamma' + \pi)^2}$$

in (2) allow, $I(\omega') > 0$ for certain values of ω'. This means that for these values of ω' more pulses are counted by the γ-detector than in the background ($\omega' \to \infty$) of the Mössbauer spectrum. This is very unlikely in a case like this.

We believe that the approach of Stöhr and Hirst is wrong for the following reason:

The expression for the spectrum is derived from the "fluctuation-dissipation: theorem [5]. This expression reads:

$$I(\omega) = \int_{-\infty}^{\infty} G(t)\, e^{-i\omega t}\, dt \qquad (3)$$

$G(t)$ is the auto-correlation function of the system, consisting of a large number of atoms. If this function is independent of the choice of time zero, then the process is stationary and the ensemble average may be replaced by the time average of one atom. In this stationary case

$$G(t) = G^{*}(-t) \tag{4}$$

and (3) can be replaced by

$$I(\omega) = Re \{ \int_{0}^{\infty} G(t)\, e^{-i\omega t}\, dt \} \tag{5}$$

In an absorber experiment the relaxation process is indeed stationary, but this is not the case for a source experiment. (Time zero cannot be chosen arbitrary; it is fixed for each atom by the ß-decay of its nucleus). So for a source experiment (4) is not true and (5) cannot be used as an expression for the relaxed spectrum (compare 3.3.(4)).

Hartmann-Boutron [9] also states that the approach of Stöhr and Hirst is wrong and shows how one should proceed in principle in the right way in the case of a source experiment (see also ref. [20], especially page 312).

References of Chapter 3

1. A. Abragam and B. Bleaney in "Electron Paramagnetic Resonance in Transition Ions" (Clarendon Press, Oxford, 1970) p. 713.
2. l.c. ref. 1, p. 733.
3. P.W. Anderson, J. Phys. Soc. Japan 9 (1954) 316.
4. A. Abragam in "The Principles of Nuclear Magnetism" (Oxford University Press, 1961) p. 447.
5. R. Kubo in "Fluctuation, Relaxation and Resonance in Magnetic Systems" ed. D. ter Haar (Oliver and Boyd, Edinburgh-London, 1961) p. 35.
6. I. Nowik, Phys. Lett. 24A (1967) 487.
7. M. Blume, Phys. Rev. Lett. 14 (1965) 96.

8. F. van der Woude and A.J. Dekker, Phys. Stat. Sol. 9 (1965) 775; F. van der Woude and A.J. Dekker, Sol. State Comm. 3 (1965) 319; F. van der Woude, thesis, (University of Groningen, 1966).
9. F. Hartmann-Boutron in "Etude de la relaxation par les methodes nucleaires", Ecole d'Automne du Mont Sainte-Odile, 1975, Université Louis Pasteur, Strasbourg.
10. M.J. Clauser, Phys. Rev. B3 (1971) 3748.
11. G.K. Shenoy and B.D. Dunlap in "Proceedings International Conference on Mössbauer spectroscopy", Volume 2, ed. A.Z. Hrynkiewicz and J.A. Sawicki (Cracow, 1975) p. 275.
12. N.T.J. Bailey, "The elements of Stochastic Processes", (John Wiley, New York, 1964) Ch. 7.
13. L.L. Hirst, Journal de Phys. Coll. 35 (1974) C6-21.
14. B. Khurgin, I. Nowik, M. Rakavy and S. Ofer, J. Phys. Chem. Sol. 31 (1970) 49.
15. J. Kondo, Solid State Phys. 23 (1968) 183.
16. F. Bacon, J.A. Barclay, W.D. Brewer, D.A. Shirley and J.E. Templeton, Phys. Rev. B5 (1972) 2397.
17. J. Stöhr, G.M. Kalvius, G.K. Shenoy and L.L. Hirst in "International Conference on Hyperfine Interactions studied in nuclear reactions and decay", ed. E. Karlson and R. Wäppling, (Upplands Grafiska AB, Uppsala, 1974) p. 80.
18. L.L. Hirst, Journ. Phys. Chem. Sol. 31 (1970) 655.
19. J. Stöhr, private communication.
20. F. Hartmann-Boutron and D. Spanjaard, Journal de Phys. 36 (1975) 307.

CHAPTER 4

INSTRUMENTATION

4.1 Movement of the absorber

As the over all splitting of the Dy sources we have used for Mössbauer effect measurements is about 45 cm/s and that of the Tm sources even 110 cm/s, a special velocity transducer (drive) is needed to move source or absorber with the required high velocities.

In the constant acceleration mode the maximum velocity of the drive is given by $v_{max} = 8\,fA$ in which f is the frequency of the movement and A is its amplitude (≈ half of full stroke).

In the sinusoidal mode the corresponding formula is $v_{max} = 2\pi fA$. In the electro-mechanical drives we have used, the amplitude is restricted to some millimeters for reasons of construction (e.g. length of magnet gap). Therefore the frequency must be high to obtain the required high velocity. (To give a specific example: for v_{max} = 80 cm/s and A = 3 mm, f must be 42 Hz with a sinusoidal movement).

When the source is moved, the background of the measured Mössbauer spectrum is curved because of the varying distance between source and detector. Because the effects in the measured sources of DyNi, DyFe, TmNi and TmFe are rather small (about 0.5 %), this curvature of the background cannot be neglected, even after the "folding" of the two obtained spectra. This problem is solved by moving the absorber, since in that case the distance between the radioactive source and the detector does not change.

Fortunately suitable single line absorbers, that can be used at room temperature, are available both for Dy and for Tm. So we have chosen to move the absorber at room temperature, while the radioactive source is kept in the tail piece of a cryostat. A special construction is needed to move the absorber, as it has to move between source and detector.

The first construction, used for measurements on DyFe and DyNi is illustrated in fig. 4.1. Because the absorber is moving off center with respect to the transducer axis in this construction,

the absorber must be connected very rigidly to the moving rod of the drive, to given the absorber the same motion as this rod.

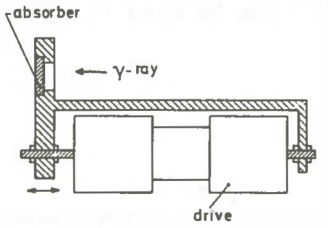

fig. 4.1. Off-axis absorber movement.

With the drives we have used, it was impossible to achieve a satisfactory constant acceleration of the absorber with such a construction, so we have chosen a sinusoidal movement. In that case the best result is obtained when the system moves at its resonance frequency. We have constructed special thick springs from fiber print-board to give the system the high resonance frequency needed.

It was impossible to reach a velocity of 80 cm/s, necessary for the measurements on TmFe and TmNi, with the construction of fig. 4.1. For this reason our first measurement with a TmFe source was done with a specially constructed mechanical drive (see section 4.2), but for the later measurements on TmFe and TmNi and also on DyNi and DyFe we have used the construction of fig. 4.2.

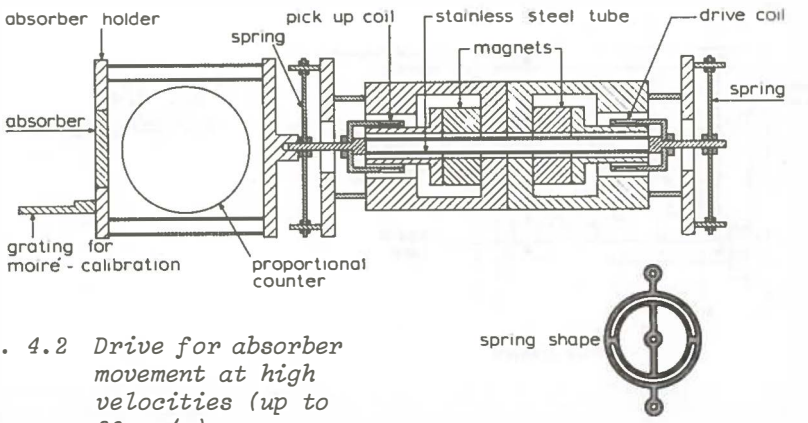

fig. 4.2 Drive for absorber movement at high velocities (up to 80 cm/s).

Here the absorber is centered on the transducer axis and the mass of the moving part can be kept much smaller than in the construction of fig. 4.1. In fig. 4.2 the detector is a proportional counter, but the arrangement of fig. 4.3 can be used if another type of detector is used.

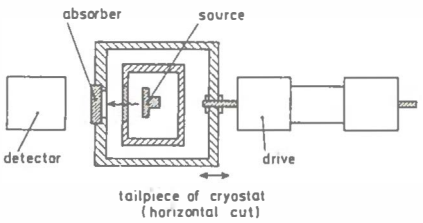

fig. 4.3
Absorber movement suitable for any type of detector.

When the absorber is moving at high velocities, it causes strong vibrations in the drive support. If the cryostat, in which the source is fixed, is connected to the same support, undesired vibrations of the source are introduced. To isolate the drive vibrations from the rest of the system, we have mounted the drive on a heavy platform as shown in fig. 4.4. Because of its large mass, the amplitude of the vibrations of the platform that carries the drive is negligibly small.

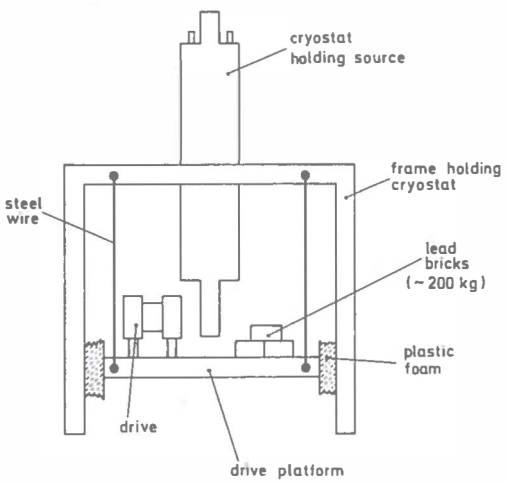

fig. 4.4
Mounting of drive.

The proportional counter should not be attached to this platform, but to the rest of the system to prevent platform vibrations from causing undesired vibrations of the thin wire inside the counter.

4.2 A mechanical high velocity drive

As has been mentioned in section 4.1, a mechanical drive has been constructed to move an absorber with a maximum velocity sufficiently high to measure the complete Mössbauer spectrum of a TmFe source (± 80 cm/s). Fig. 4.5 gives a schematic drawing of this drive. To obtain a reproduceable motion, the amplitude of the drive must be much larger than its mechanical backlash. On the other hand; The larger the amplitude, the larger the distance between source and detector, which reduces the counting rate.

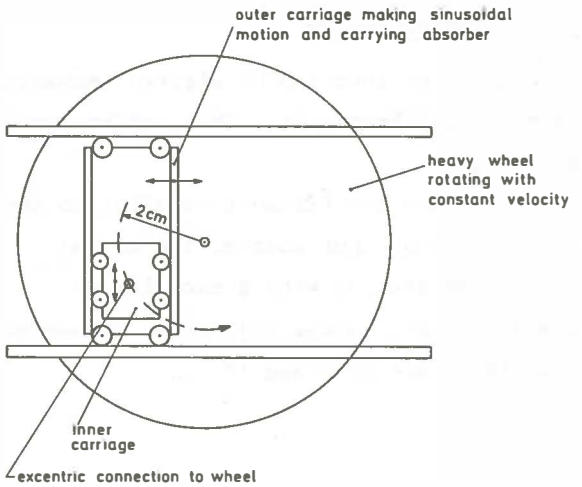

fig. 4.5 Mechanical high velocity drive.

The best results were obtained using a synchronous motor (220 V; 50 cps) coupled to a reduction gear. (With this system the variations in revolution time were smaller than 0.1 percent). For each revolution an electric pulse was obtained by means of a slotted disk, a photodiode and a light bulb. This pulse was used to synchronize the address scaler of the analyzer and the absorber motion.

An absolute velocity calibration of the drive was made by means of a simple Moiré system. (Fig. 4.6). This calibration proved that the motion of the drive deviated at most 1 percent from a pure sinusoidal motion at a maximum velocity of 79 cm/s.

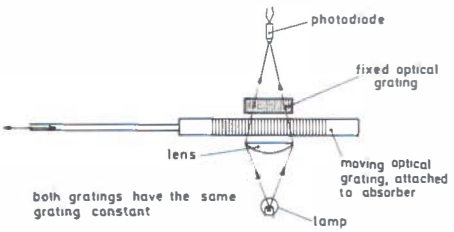

fig. 4.6. Optical velocity calibration system (Moiré type) for mechanical drive.

4.3 Absolute velocity calibration system

For the absolute velocity calibration of electro mechanical drives we have built a Moiré calibrator [1]. This calibrator is small and easy adjustable.

A light bulb (fig. 4.7) with its filament parallel to the lines of the grating is used as a light source. The moving grating is imaged onto a fixed grating with a much larger grating constant by means of a microscope objective. In our measurement the grating constants are 20 μ and 170 μ.

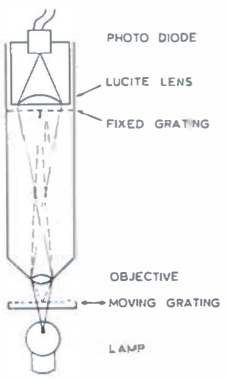

fig. 4.7
Schematic of Moiré calibrator.

The last grating has been made photographically from a line pattern drawn on paper. The frequency of the light modulation is determined by the grating constant of the moving grating. This constant has been measured from the diffraction pattern produced by the grating with a laser beam. The distance between objective and upper grating is chosen in such a way that the image of the lower grating has the same grating constant as the upper grating to obtain a strong modulation of the light. The precise position of the upper grating is not very critical. When adjusting the instrument an eyepiece can be used to look at the image produced by the objective. After adjustment the eyepiece is replaced by a small Lucite lens that focuses the light on a photodiode.

In our instrument we used a 3 W lamp that gave a modulation of the photodiode signal (Philips BPX 25) of more than 1 V, although the contrast of the moving grating is rather poor. The grating constant of the moving grating of the calibrator has been measured with the arrangement of fig. 4.8. Table 4.I gives the positions of the diffraction maxima.

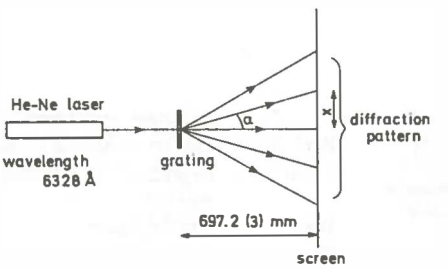

fig. 4.8. Measurement of grating constant.

$\bar{x}_n$ is the average of the distances from the zero'th order maximum to the maxima of order n left and right from it.

From the average of the values obtained for $n/\sin\alpha$ we derive a grating constant of $20.11(2) \times 10^{-6}$ m.

Table 4.I Positions of diffraction maxima

n	$\bar{x}_n$ (mm)	$n/\sin\alpha$
1	21.95	31.78
2	44.0	31.75
3	66.05	31.85
4	88.4	31.80
5	111.1	31.77
6	133.95	31.80

4.4 The complete Mössbauer spectrometer

Fig. 4.9 gives a diagram of the complete Mössbauer spectrometer as it has been used in most of the measurements. Some early measurements were done with the spectrometer arrangement described by Inia [2].

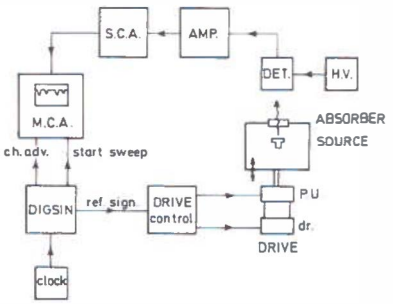

S.C.A. = single channel analyzer
M.C.A. = multi channel analyzer
Digsin = Digital sine wave generator
Amp. = Amplifier
Det. = Detector
H.V. = High voltage supply
P.U. = Pick up coil
dr. = Drive coil

fig. 4.9. Schematic of Mössbauer spectrometer.

In both versions the multichannel analyser was working in the multiscaler mode. The reference signal for the drive is produced by a digital sinewave generator. This generator is of the type described by Halder and Kalvius [3], with the possibility to generate a start pulse for the multiscaler at a pre-set step of the up-down counter (2^{14} steps in each period of the sine wave). In this way we could compensate for small phase shifts between the reference signal and the absorber movement.

4.5 Source heating

a) In the DyNi measurement which was done at a number of different temperatures (5 K, 13 K, 22 K, 57 K, 77 K and 293 K), the sources was mounted in the holder shown in fig. 4.10.

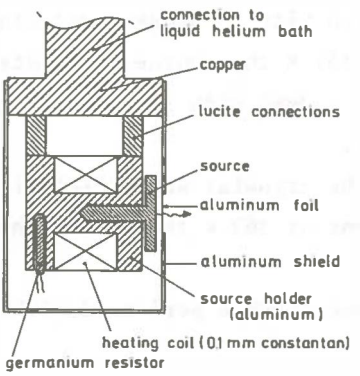

fig. 4.10. Variable temperature source holder for DyNi.

This holder was connected to a copper tail piece in a Janis 4DT liquid helium cryostat. The source was electrically heated and its temperature was measured with a calibrated germanium resistor. The resistance was measured with a conventional 4-wire potentiometric set up, using a differential voltmeter. The heater current consists of a constant part and a part proportional to the output of a differential voltmeter. In this way the temperature could be kept constant within 0.5 K in the temperature range from 5 K to 77 K. For the 77 K measurement the helium container of the cryostat was filled with liquid nitrogen.

b) In the DyFe measurement carried out at four different temperatures (5 K, 151 K, 273 K and 363 K) the holder of fig. 4.11 was used.

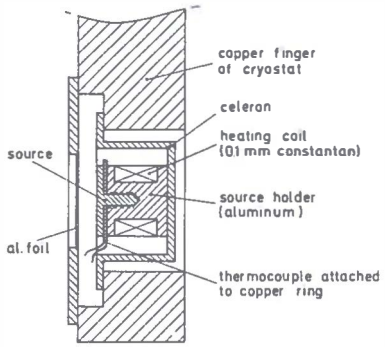

fig. 4.11. Variable temperature holder for DyFe.

The source temperature was measured with a copper-constantan thermocouple. For the measurement at 151 K the source was heated using the same principle as described for DyNi with liquid nitrogen in the helium vessel of the cryostat.

For the measurement at 0°C the cryostat was filled with melting ice and for the measurement at 363 K the source was heated again.

In this way the four measurements were performed without removing the source.

c) $^{169}ErF_3$ is a single line source for thulium Mössbauer effect measurements at temperatures above 550 K [4]. To test thulium absorbers (see section 6.1) an oven was built to heat such an ErF_3 source (see fig. 4.12). The heating coil (15 Ω) and the chromel-alumel thermocouple are made of thermocoax, a very suitable material for small ovens. The maximum oven temperature, obtained with a heating current of ∿ 3.5 A was ∿ 1000°C (1273 K).

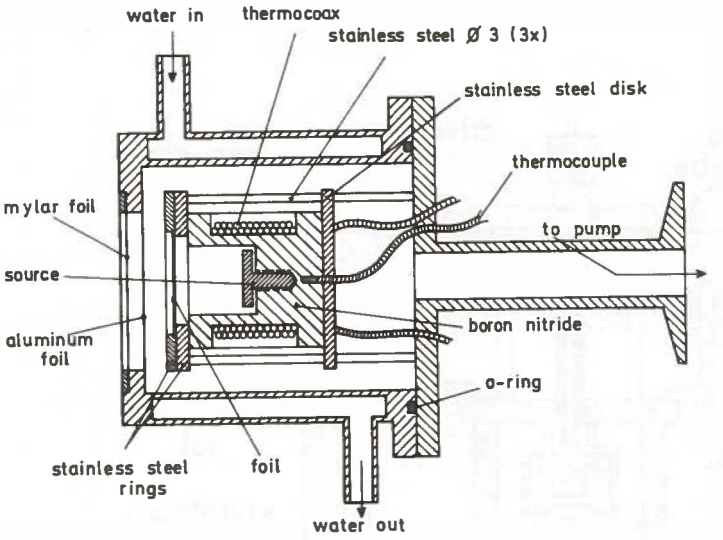

fig. 4.12. Small vacuum oven for source.

4.6 Liquid nitrogen cryostat

A simple styrofoam liquid nitrogen cryostat was built, to test single line sources and absorbers of some dysprosium compounds (see section 5.1) at different temperatures. The construction of the cryostat is clear from fig. 4.13.

Source and absorber temperature can be measured with a copper-constantan thermocouple. The temperature of the moving absorber could be regulated from 77 K up to about 160 K; that of the source between 77 K and room temperature. The liquid nitrogen consumption of the cryostat is of the order of 1 ℓ/hr.

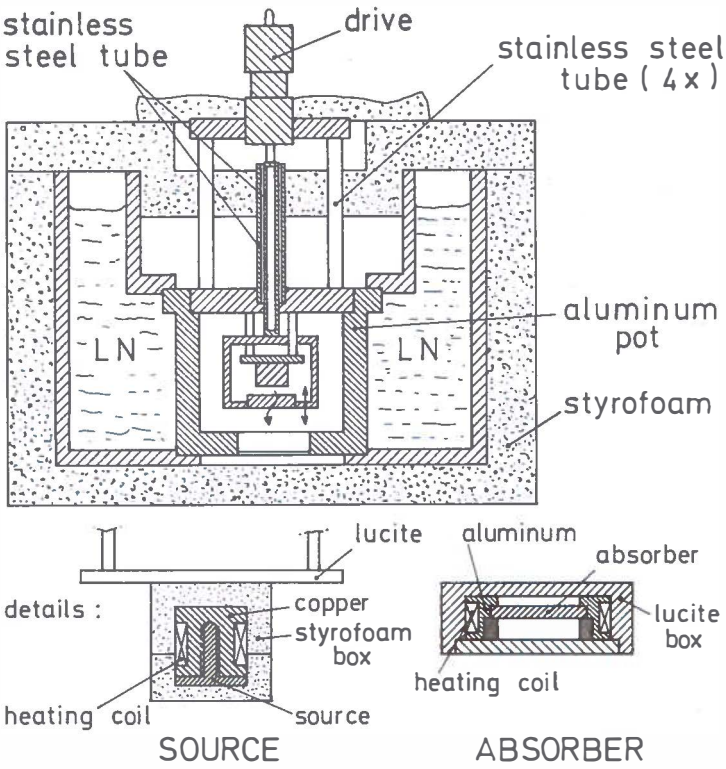

fig. 4.13. Styrofoam liquid nitrogen cryostat.

References Chapter 4

1. H.P. Wit, Rev. Sci. Instrum. 46 (1975) 927.
2. P. Inia, Thesis, University of Groningen, 1971, p. 49.
3. N. Halder and G.M. Kalvius, Nucl. Instrum. Meth. 108 (1973) 161.
4. R.G. Barnes, R.L. Mössbauer, E. Kankeleit and J.M. Poindexter, Phys. Rev. 136A (1964) 175.

CHAPTER 5

^{161}Dy ABSORBERS AND SINGLE LINE SOURCES

5.1 Dysprosium single line absorbers

To test some single line absorbers of DyF_3 and $Dy_2Ti_2O_7$, two series of measurements have been done with single line sources of $Dy_{0.5}Gd_{0.5}F_3$. According to Cohen [1] this material emits a narrow single line at room temperature. The first source was made by irradiating 15 mg of $Dy_{0.5}Gd_{0.5}F_3$, containing natural Dy and Gd, for 2 days in a neutron flux of $2 \cdot 10^{14}/cm^2s$. For the second source 10 mg of the same material was irradiated for 7 days in a flux of $5 \cdot 10^{12}/cm^2s$.

The energy spectrum of the sources obtained in this way is complicated, as besides the desired ^{161}Tb activity several unwanted radioactive isotopes are created during irradiation (^{165}Dy, ^{166}Dy, ^{159}Gd).

For this reason a Si(Li) detector has been used for the measurements. These two sources were used at different temperatures with several absorbers, also at different temperatures in the liquid nitrogen cryostat described in section 4.6. The most important results of the test measurements are:

I. The linewidth of the source decreases at increasing temperature. For this measurement the source was kept at 120, 180 and 240 K versus a Dy-metal absorber at LNT. The velocity scale was chosen in such a way, that only the two inner lines of the Dy-metal spectrum appeared. For the rest of the measurements the sources were used at room temperature.

II. The linewidth of a DyF_3 absorber is much smaller at RT than at LNT (see fig. 5.1). At LNT the line is probably broadened by relaxation effects. This broadening explains the rather large linewidth in the Mössbauer spectra of DyFe measured by Inia [2].

III. An absorber of $Dy_2Ti_2O_7$ (36 mg/cm^2) [3] has the smallest linewidth (0.73(3) cm/s) at a temperature of about 130 K. The depth of the absorption line measured with this absorber at that temperature is about a factor three smaller than if measured with a DyF_3 absorber of about the same thickness. (Also measured at the temperature where it emits the narrowest line).

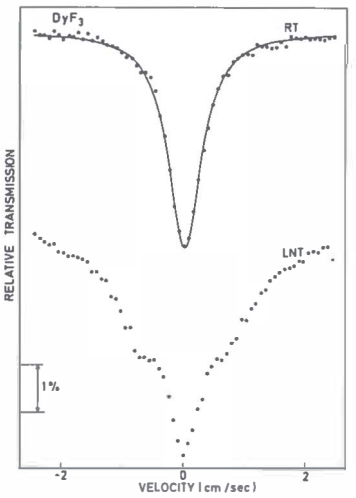

fig. 5.1 Mössbauer spectra of DyF_3 single line absorber

IV. The best result was obtained with a DyF_3 absorber at RT enriched to 92 % in ^{161}Dy. This absorber contains 11 mg/cm^2 of ^{161}Dy. It was made by dissolving enriched Dy_2O_3 in concentrated HCl under heating. The DyF_3 was precipitated by adding a small amount of 40 % HF. This DyF_3 was washed with water and dried at 110^{o}C. After this, the powder was placed in an evacuated quartz tube that was heated to 150^{o}C for 6 hours. Then the temperature was raised slowly to 850^{o}C and kept at this value for 6 hours. After cooling down, X-ray diffraction analysis of the powder showed rather broad lines. For this reason the powder was heated again in vacuum in a platinum foil in the quartz tube up to 1100^{o}C for 3 hours and after this very slowly cooled down. After this heating procedure the powder had a dark colour and the X-ray analysis gave narrow lines.

The single line in the Mössbauer spectrum of this absorber at RT measured with one of the $Dy_{0.5}Gd_{0.5}F_3$ sources also at RT had a width of 0.70(1) cm/s. From a measurement with this source at RT versus a Dy-metal absorber at 5 K. the linewidth of the source was estimated to be 0.36(4) cm/s, assuming the linewidth of the Dy metal absorber to lie between 0.02 cm/s (natural linewidth) and 0.09 cm/s. The last value was obtained by Almog et al. [3] in a spectrum of Dy metal, using a single line source of

$^{161}Tb_2Ti_2O_7$. Obviously their source emitted a very narrow single line.

We conclude that the linewidth of the enriched DyF_3 absorber at RT is 0.34(5) cm/s. This absorber has been used in most of the measurements with DyNi and DyFe sources.

5.2 Mössbauer spectrum of Dy metal

Cohen and West have measured the spectrum of Dy-metal at 4.2 K with great accuracy [4]. Mainly to test our velocity drive and calibration system we have repeated this measurement. As a source $Dy_{0.5}Gd_{0.5}F_3$, enriched to 95 % in ^{162}Dy and to 97 % in ^{160}Gd, was used. The absorber consisted of a 34 mg/cm^2, 99.9 % pure Dy foil.

Unfortunately, only a xenon-filled proportional counter was available for the measurement. With this counter the 25.65 keV Mössbauer line could not be separated from the escape peaks around 20 keV of X-ray lines. For this reason the depths of the lines in our spectrum are about three times smaller than those in Cohen's spectrum, but this has been compensated by a larger number of counts per channel. During the measurement the source, that moved sinusoidally at RT, was attached to the drive as shown in fig. 5.2. Before and after the measurement a Moiré-calibration was done with the system described in section 4.3. The absolute velocity scale could be derived from this calibration with an accuracy better than 0.2 %. A correction of about 0.3 % was made for the cosine effect.

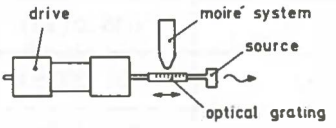

fig. 5.2
Source attachment for Dy metal measurement.

The spectrum obtained after folding the two spectra stored in 2048 channels of the multichannel analyser is given in fig. 5.3.

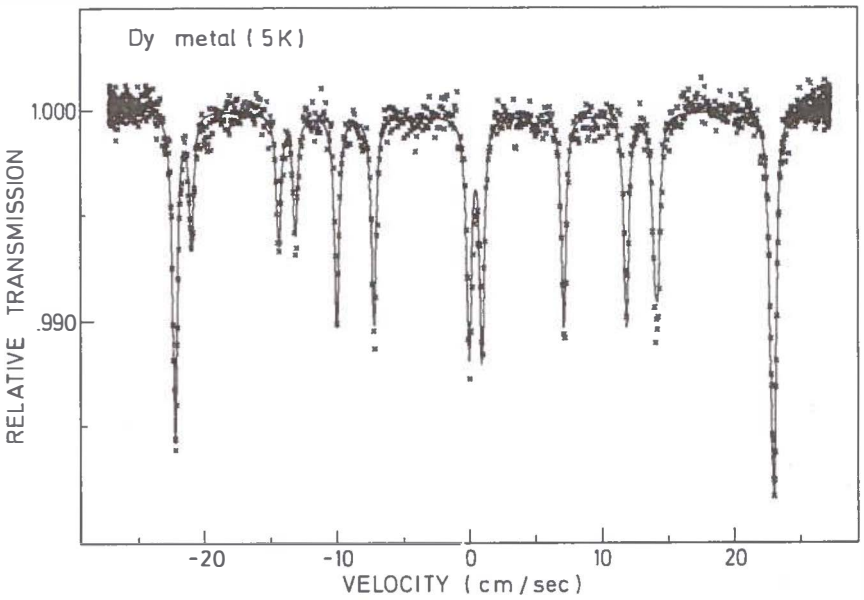

fig. 5.3. Mössbauer spectrum of Dy metal (4.2 K).

The results obtained from a computerfit of the spectrum are given in Table 5.I, together with the results of Cohen and West. Within the errors these values are the same, except for Q^*/Q.

Table 5.I Parameters of Dy metal spectrum (4.2K)

		Cohen and West	this work
$g_N \mu_N H$	cm/s	4.04(2)	4.036(11)
	MHz	836(4)	835.0(23)
$\frac{1}{4} e^2 qQ$	cm/s	3.142(15)	3.158(9)
	MHz	650(3)	653.4(1.9)
g_N^*/g_N		- 1.236(2)	- 1.238(2)
Q^*/Q		0.995(2)	0.988(2)

With the same source and absorber (at 4.2 K) a spectrum of the inner lines of the spectrum of fig. 5.3 was measured. From fig. 5.4 it is clear that these two lines do not have the same amplitude and when the spectrum is fitted with two lines with the same width and amplitude, the distance between them is about 4 % too small compared to the distance in the spectrum with the full velocity scale. The correct separation is found, if two small extra lines are added at the position indicated with arrows in fig. 5.4.

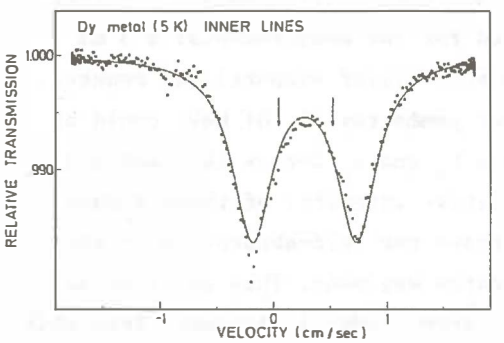

fig. 5.4
Inner lines of spectrum of Dy metal (4.2 K).

The origin of these lines is not clear. They cannot be caused by oxidation because the Dy_2O_3 spectrum is magnetically split at this temperature (See section 8.2).

References Chapter 5

1. R.L. Cohen and H.K. Guggenheim, Nucl. Instrum. Meth. 71 (1969) 27.
2. P. Inia, Thesis, University of Groningen, 1971, pp. 57,58.
3. A. Almog, E.R. Bauminger and S. Ofer, Proceedings of International Conference on Applications of the Mössbauer effect, ed. M. Pasternak, (Soreq Nuclear Research Center, Yavne, Israel, 1972) p. G1.
4. R.L. Cohen and K.W. West in "Hyperfine Interactions in excited nuclei", ed. G. Goldring and R. Kalish (Gordon and Breach, New York, 1971) p. 613.

CHAPTER 6

^{169}Tm ABSORBERS AND SOURCES

6.1 Thulium single line sources and absorbers

A series of measurements was done using a source of ErF_3 to test an absorber of $TmAl_2$. This source was made by irradiating 14 mg of ErF_3, containing natural Er, for 2 days in a neutron flux of 2×10^{14} $cm^{-2}s^{-1}$. Besides the desired ^{169}Er activity, the isotope ^{171}Er is produced, that decays with a half life of 7.5 hr. For this reason the source was not used until 3 days after irradiation. Two detectors were used for the measurements: a 3 mm thick Si(Li) detector and a krypton filled proportional counter. With the first one the Mössbauer gamma ray (8.401 keV) could be separated better from the erbium L_α and L_β X-rays (6.9 keV and 7.8 keV) [1]. To reduce the relative intensity of these X-rays as much as possible and to decrease the self-absorption of the Mössbauer gamma rays, a thin source was made. This was done by mixing 4 mg of ErF_3 with some starch powder in acetone. From this suspension a thin layer of the ErF_3-starch mixture deposited on an aluminum disk when the acetone evaporated. The absorber was made in a similar way: 5 mg/cm^2 $TmAl_2$ powder was deposited on a 1 mm thick beryllium disk and fixed with lacquer spray. With source and absorber at RT the slightly asymmetric quadrupole-split spectrum of fig. 6.1 was obtained, using the Si(Li)-detector.

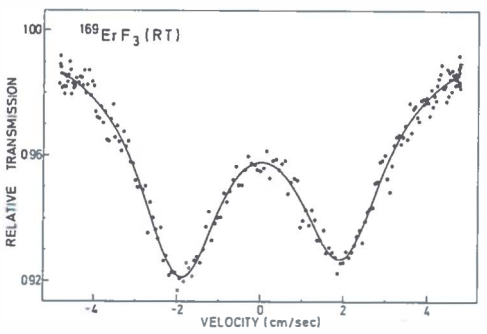

fig. 6.1
Mössbauer spectrum of a source of $^{169}ErF_3$ at room temperature.

Numerical results from the computer fit are given in Table 6.I.

Table 6.I

Parameters of $^{169}ErF_3$ Mössbauer spectrum at room temperature (versus $TmAl_2$ single line absorber)

Line	Position (cm/s)	Rel. depth (%)	Linewidth (cm/s)
1	- 1.90(2)	7.2(1)	2.5(1)
2	1.95(2)	6.6(1)	2.6(1)

The measured quadrupole splitting of 3.85(4) cm/s is in agreement with that given by Barnes et al. [2]: 3.7(2) cm/s.

When the source was heated to 553 ± 3 K [3] in the small oven described in section 4.5.c, while the absorber was moving at RT, a single line with a width of 2.77(7) cm/s was obtained. When measured with the Si(Li) detector the line had a relative depth of 8 %.

A disadvantage of the ErF_3 source described above is the fact that it has to be heated to emit a single line. Therefore an attempt was made to produce a source that emits a single line at room temperature: 17 mg of $ErAl_2$, containing natural Er, was irradiated for 5 days in a neutron flux of 2×10^{14} $cm^{-2}s^{-1}$. This source had a thickness of about 10 microns.

With this source a Mössbauer spectrum was measured versus a thulium metal absorber, both at RT. This absorber was made by evaporating a layer of Tm-metal with a thickness of 2 μm in ultra-high vacuum on an aluminum foil (thickness 12 μm).

For this measurement the Si(Li) detector was used, but the relative depth of the measured single line (width: 3.9(3) cm/s) was only about 0.6 percent. This was caused by the fact, that the Mössbauer-gamma rays were "buried" in X-rays. A careful analysis of the gamma rays emitted by this source showed that the large background mainly consisted of γ- and X-rays of several tungsten isotopes (^{182}W, ^{183}W). This can be explained by the presence of a small amount (≈ 1 %) of tantalum metal in the erbium metal used for the preparation of the $ErAl_2$.

To avoid this problem a source was made by implanting ^{169}Er ions with an energy of 120 keV into two 6 μm thick aluminum foils. Total implanted area: ≳ 3 cm^2; dose 10^{14} at/cm^2. After implantation the foils were folded to obtain a source with an area of about 1 cm^2. A pulse height spectrum measured with this source and the krypton-filled proportional counter as a detector showed a single line at 8.4 keV on a continuous 10 % background. A disadvantage of this method of source preparation is the fact that 98 - 99 % of the ^{169}Er activity gets lost in the isotope separator during implantation.

With this $^{169}ErAl$ source, used at RT, the $TmAl_2$ absorber and the Tm-metal absorber were tested at RT. Both gave a single line.

Table 6.II summarizes the results from the single-line source and absorber tests.

Table 6.II Comparison of Tm single line sources and absorbers

Source	Absorber (RT)	Rel. depth (%)	Linewidth (cm/s)	Isomer shift (cm/s)
ErF_3 (553 K)	$TmAl_2$	8	2.77(7)	0.04(2)
$ErAl_2$ (RT)	Tm metal	0.6	3.90(28)	- 0.15(7)
ErAl (RT)	$TmAl_2$	9	3.47(4)	0.05(1)
	Tm metal	21	3.94(4)	0.04(1)

In an attempt to improve the linewidth of the $^{169}ErAl$ source it was annealed for 2 hours at 620°C in vacuum. (40°C below the melting point of aluminum). However, after this anneal the source gave an asymmetric doublet instead of a narrower single line when measured at room temperature versus the $TmAl_2$ absorber (RT).

The positions of the lines of the doublet were - 1.57(3) and 1.63(3) cm/s and their widths 3.5 cm/s. Their relative depths were 4.5 and 5.2 percent respectively.

This surprising result indicates that even after annealing at this temperature there remains radiation damage in the lattice and apparently the Er ions become associated with this damage, leading to an electric field gradient at the Er nuclei in the otherwise

cubic lattice. The origin of the slight asymmetry of the doublet is not clear.

6.2 Mössbauer spectrum of Tm-metal at 5 K [4]

The Mössbauer spectrum of Tm metal at 5 K has been measured before [5,6], yielding values for the magnetic dipole and electric quadrupole interaction strengths and for the excited to ground state nuclear dipole moment ratio. We decided to repeat this measurement because we felt that the use of Moiré velocity calibration and of an implanted ^{169}ErAl source would yield more accurate values for the hyperfine interaction parameters.

For this measurement the implanted ^{169}ErAl source described in section 6.1 was used. The source was moved sinusoidally at room temperature with the drive from fig. 4.2. An absolute velocity calibration with an accuracy better than 0.2 % was made by means of the Moiré technique.

With the Tm metal absorber also described in section 6.1 at 5 K the spectrum of fig. 6.2 was obtained.

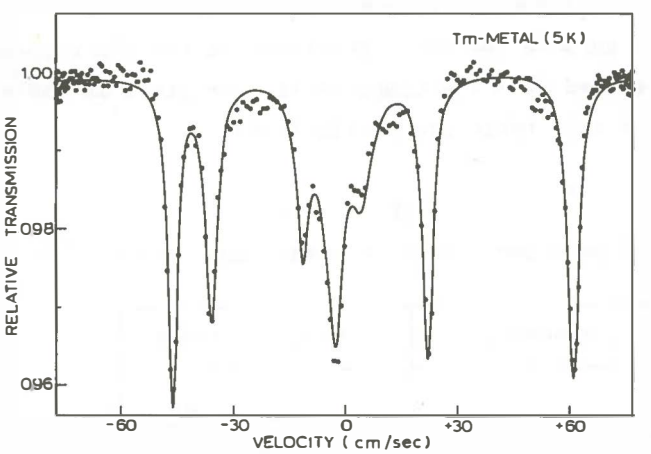

fig. 6.2 Mössbauer spectrum of Tm metal at 5 K measured with an implanted ^{169}ErAl single line source at RT.

This spectrum differs somewhat from the expected six-line pattern [5], but a good computer fit to it could be obtained by adding an

extra doublet to the six-line component. The splitting of this doublet (8 cm/s) is in fair agreement with that measured for Tm_2O_3 (7.2 cm/s) [2]. This component can therefore be explained by a slight oxidation of the absorber. A fit was also made to the four outer lines of the spectrum only. This fit yielded, within statistical errors, the same values for the parameters as the first one.

For the ratio of the excited and ground-state nuclear magnetic moments we find $\mu^*/\mu = -2.223(13)$. (The error in this value is partly caused by the fact that the movement of the source was not perfectly sinusoidal; it deviated at most 0.2 % from a pure sine wave, as could be seen from the Moiré calibration). Previously measured values for this ratio are - 2.22(7) [6], - 2.17(10) [7] and - 2.27(4) [8].

Our values for the quadrupole splitting, e^2qQ^*c/E_γ = 28.52(17) cm/s = 1933(12) MHz, and over-all splitting, 107.2(3) cm/s, are also in agreement with those previously measured [5,6] but much more accurate.

The Mössbauer spectrum of Tm metal at 5 K is a convenient calibration for drive velocities up to about 70 cm/s, using our accurate values of the hfs parameters.

For this purpose the exact positions of the six resonance lines, as obtained from the computerfit, are given in table 6.III. (The errors in this table are statistical).

Table 6.III

Position of resonance lines in Mössbauerspectrum of Tm metal.

Line number	Position (cm/s)
1	- 46.26(3)
2	- 35.86(3)
3	- 11.20(5)
4	- 2.60(5)
5	22.06(3)
6	60.98(3)

References Chapter 6

1. E. Kankeleit, F. Boehm and R. Hager, Phys. Rev. 134 (1964) B747.
2. R.G. Barnes, R.L. Mössbauer, E. Kankeleit and J.M. Poindexter, Phys. Rev. 136 (1964) A175.
3. R.L. Mössbauer, Rev. Mod. Phys. 36 (1964) 362.
4. H.P. Wit and L. Niesen, accepted for publication in Hyperfine Interactions.
5. M. Kalvius, P. Kienle, H. Eicher, W. Wiedermann and C. Schüler, Z. Phys. 172 (1963) 231.
6. R.L. Cohen, Phys. Rev. 169 (1968) 432.
7. R.L. Cohen, Phys. Rev. 134 (1964) A94.
8. M. Kalvius et al., see footnote 20 in ref. [7].

CHAPTER 7

INVESTIGATIONS OF DyNi, DyFe, TmNi and TmFe

7.1 Preparation of sources

The sources for the DyNi and DyFe investigations were obtained by implanting ^{161}Tb ions by means of the Groningen isotope separator (see section 1.6) into nickel or iron foils (purity of the foils 99.998 %). Before implantation the foils were heated for half an hour to 600°C in a hydrogen stream, to minimize the oxygen layer on the surface.

^{161}Tb was obtained with the reaction $^{160}Gd(n,\gamma)^{161}Gd \rightarrow {}^{161}Tb$ by irradiating about 7 mg. of Gd_2O_3 (enriched to 97 % in ^{160}Gd) for 4 days in a neutronflux of 2×10^{14} n/cm^{2}sec in the reactor of the R.C.N. at Petten. The efficiency of the implantations was roughly 2 %; a typical source strength was 600 μCi.

For the TmNi and TmFe investigations the sources were obtained in a similar way. The implanted ^{169}Er activity was obtained with the reaction $^{168}Er(n,\gamma)^{169}Er$ by irradiating about 15 mg. of Er_2O_3 (enriched to 98 % in ^{168}Er) for 15 days in a neutronflux of 2×10^{14} n/cm^{2}sec, also in the reactor at Petten. In this case the implanted sources had a typical strength of 3 mCi.

7.2 Investigations of DyNi

A. *Sources and absorbers*

Measurements were done with three sources:

Source I : Implantation energy 130 keV; dose 0.8(4) $\times 10^{14}$ at/cm^2
Source II : " " 140 keV; dose 1.8(9) $\times 10^{14}$ at/cm^2
Source III: " " 110 keV; dose 1.6(8) $\times 10^{14}$ at/cm^2

In all measurements an absorber of DyF_3 was moved sinusoidally at room temperature. In this way background curvature was kept to a minimum, which is important when observing the broad, relaxation-type structures frequently occurring in ^{161}Dy spectra.

The measurements with source I were done with an absorber that gave only a small resonant absorption (about 0.2 % for the outer lines at 5 K). The measurements with the other two sources were done

after the absorbertests described in section 5.1 with a much better absorber of $^{161}DyF_3$ (11 mg/cm^2), that gave about 0.8 % effect for the outer lines at 5 K.

In the measurements with the first two sources the absorber holder of fig. 4.1 was used, combined with a 3 mm thick NaI-crystal as detector. The measurements with source III were done with the absorber construction shown in fig. 4.2 and a krypton filled proportional counter.

The peak-background ratio for the 25.7 keV line of ^{161}Dy is almost the same for both counter types, but the efficiency of the NaI-counter is about a factor 2 better than that of the proportional counter. For this reason it is worthwhile to use the absorber construction shown in fig. 4.3 for future measurements with implanted Dy sources.

B. *Experimental results*

a) Source I:

Measurements were performed at source temperatures of 1.3 K and 5 K. The temperature of 1.3 K was obtained by reducing the vapor pressure of the liquid helium bath of the cryostat by means of a mechanical vacuum pump. The two Mössbauer spectra were fitted by two components, each of which is the sum of sixteen Lorentzians, given by the hamiltonian:

$$\mathcal{H} = -g_N\mu_N H_{hf}\left(\frac{g_N^*}{g_N} I_z^* - I_z\right) + \tfrac{1}{4}e^2qQ\left\{\frac{Q^*}{Q}\cdot\frac{3(I_z^*)^2 - I^*(I^*+1)}{I^*(2I^*-1)} - \frac{I_z^2 - I(I+1)}{I(2I-1)}\right. \qquad (1)$$

The relative areas of the sixteen lines are given by the appropriate Clebsch-Cordan efficients. For g_N^*/g_N and for Q^*/Q the values - 1.236 and 1.00 were used respectively (see section 5.2). The computer fits could be improved by taking the width of the two inner lines (Γ_2) smaller than that of the other fourteen lines (Γ_1). (In this way a small spread in hyperfine fields and quadrupole splittings has been incorporated).

The results of the fits are given in Table 7.I. The errors given in this table are statistical. The estimated error in the

velocity scale is about 5 % for these preliminary measurements. They mainly serve to show that the Mössbauer spectra at 1.3 K and 5 K are the same within experimental error.

Table 7.I.

Parameters derived from Mössbauer spectra for DyNi (source I)

Source temp.	Comp.	$g_N \mu_N H_{hf}$ (cm/s)	$\frac{1}{4}e^2qQ$ (cm/s)	Γ_1 (cm/s)	Isomer shift (cm/s)	Relative Intensity
1.3 K	1	4.07(1)	- 2.64(7)	1.25(12)	- 0.10(4)	0.56(7)
	2	3.32(1)	- 1.59(5)	0.93(9)	- 0.32(3)	0.44(7)
5 K	1	4.07(1)	- 2.71(5)	1.05(9)	- 0.22(3)	0.50(7)
	2	3.31(1)	- 1.69(7)	1.27(11)	- 0.28(4)	0.50(7)

Because of the fact that in these measurements (like in most of our measurements with implanted sources) the source spectrum was split instead of the absorber spectrum (single line absorber), the velocity scale is inverted with respect to that for an absorber measurement with a single line source (compare section 5.2).

b) Source II:

Measurements were performed at source temperatures of 5 K, 13 K, 22 K, 57 K, 77 K and 293 K. The four lowest temperatures were obtained as described in section 4.5.a. All spectra, except for the one measured at 293 K, were fitted by two components of Lorentzian lines in the same way as those from source I. This was done because very fast relaxation was observed for one component and very slow relaxation for the other. Then both components can be written as the sum of sixteen Lorentzians (see section 3.1). The 293 K spectrum was fitted by one component plus an extra single line. In this fit there are systematic differences between measured and calculated spectrum, indicating that the assumption of very fast

relaxation is not quite valid.

Four of the fitted spectra are given in fig. 7.1 Numerical results can be found in table 7.II. Again the errors are statistical. (In these measurements the velocity calibration turned out to be wrong, due to a systematic difference between the velocity of the absorber and of the drive rod. For this reason the velocity scale has been adjusted to obtain the same value for the overall splitting at 5 K as in the corresponding measurement with source III).

Table 7.II.
Parameters derived from Mössbauer spectra of DyNi (source II).

Comp.	Source temp.	$g_N \mu_N H_{hf}$ (cm/s)	$\frac{1}{4}e^2qQ$ (cm/s)	linewidth (cm/s$\frac{3}{4}$	Isomershift (cm/s)	Relative Intensity
I	5K	4.070(3)	-2.81(2)	1.30(3)	-0.34(1)	
	13K	4.073(3)	-2.65(3)	1.33(4)	-0.37(1)	
	22K	4.056(4)	-2.41(4)	1.48(6)	-0.31(1)	
	57K	4.07(1)	-1.90(11)	1.6(2)	-0.18(2)	
	77K	4.07(2)	-2.86(24)	2.2(4)	-0.20(2)	
	293K	single line		0.41(5)	-0.35(2)	
II	5K	3.232(4)	-1.66(2)	1.07(4)	-0.46(1)	0.38(2)
	13K	3.244(4)	-1.66(3)	1.13(5)	-0.50(2)	0.42(3)
	22K	3.140(4)	-1.40(3)	1.26(7)	-0.51(2)	0.44(4)
	57K	2.20(1)	-0.60(5)	1.75(8)	-0.43(1)	0.73(5)
	77K	1.96(1)	-0.43(6)	1.96(9)	-0.44(1)	0.79(7)
	293K	0.66(1)	-0.11(4)	1.00(4)	-0.36(2)	-

c) Source III:

Four measurements have been done with this source:

1. At 5 K, directly after implantation
2. At 5 K, after one hour annealing in vacuum at 200 ± 5°C
3. At 5 K, after one hour annealing in vacuum at 400 ± 5°C
4. At 77 K, after the annealing at 400°C.

During the annealing steps much care has been taken to avoid the presence of oxygen in the vacuum.

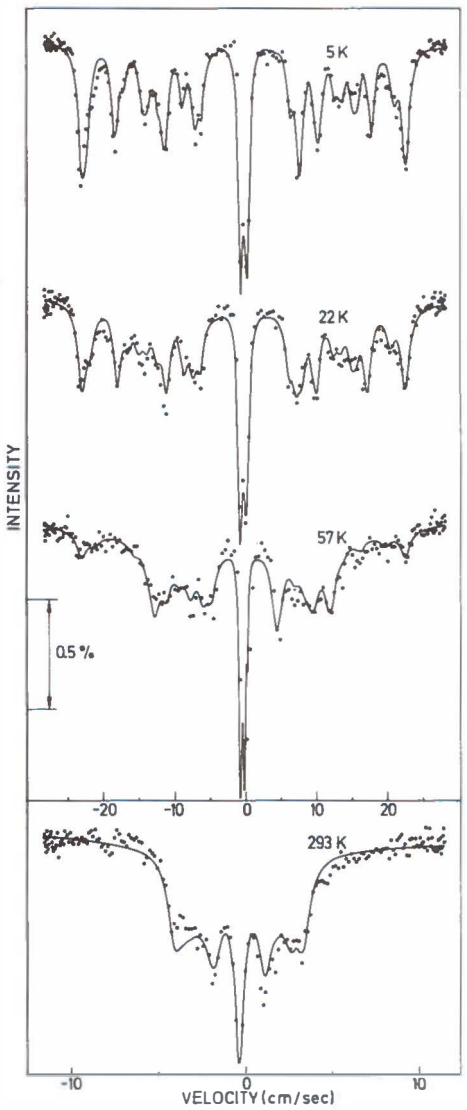

fig. 7.1
Mössbauer spectra from unannealed DyNi source at different temperatures.

The first two spectra were fitted by two components, as for source I. The third spectrum could be fitted well with only one component; the second component has a relative intensity less than 5 %.

For the fourth spectrum a theoretical fit was made using the two level relaxation model described in section 3.5, assuming that

all the Dy ions in the nickel are associated with damage after the 400°C annealing. Two components are present in this fit:

a) a component with very slow relaxation ($\pi_0 << \omega_L$; compare fig. 3.6.a). For this component (measured at 77 K) the overall splitting ($g_N \mu_N H_{hf}$ = 4.068(4) cm/sec) is the same as that measured at 5 K.

b) a component for which $\pi_0 \approx \omega_L$ (see fig. 3.6.g). A good fit was obtained for π_0 = 10 cm/sec (= 2.1 × 10^3 MHz) and α = 0,4.

(ω_L is the Larmor precession frequency of the nucleus). The total area of the spectrum measured at 77 K after annealing is 0.037(6) cm/sec.

Fig. 7.2 and 7.3 give the four spectra. Numerical results from the computer fits (with statistical errors) are given in table 7.III. For these measurements an absolute velocity calibration with an accuracy better than 0.5 percent was made.

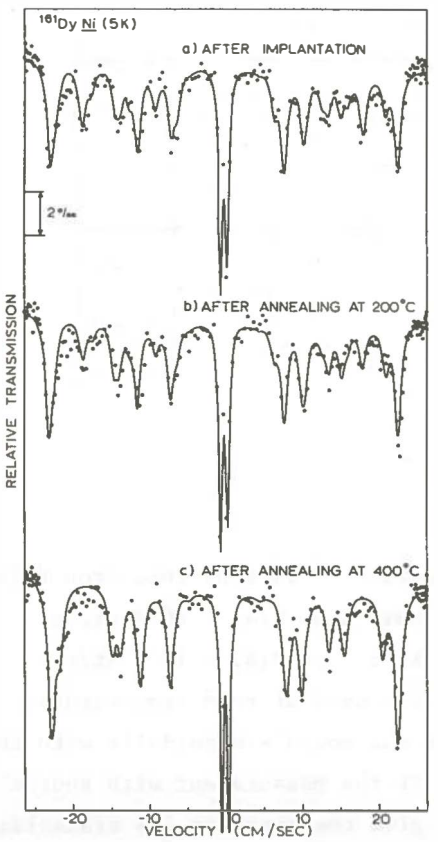

fig. 7.2
Mössbauer spectra from DyNi source (5 K) before and after annealing.

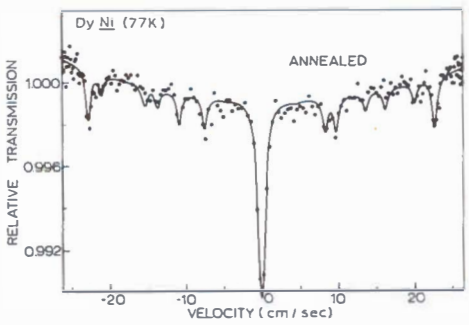

fig. 7.3
Mössbauer spectrum from DyNi (77 K), after annealing at 400°C.

Table 7.III Parameters derived from Mössbauer spectra of DyNi (source III).

Comp.	Measurement	$g_N \mu_n H_{hf}$ (cm/s)	$\frac{1}{4}e^2qQ$ (cm/s)	linewidth (cm/s)	isomershift (cm/s)	relative intensity	total area (cm/s)
I	after implantation	4.069(3)	- 2.84(3)	1.08(4)	- 0.20(1)	0.59(2)	-
	after 200°C anneal	4.084(3)	- 2.83(2)	1.03(4)	- 0.20(1)	0.71(2)	-
	after 400°C anneal	4.052(3)	- 2.47(2)	1.08(4)	- 0.17(1)	1.00(-5)	-
II	after implantation	3.29(1)	- 1.74(4)	1.15(8)	- 0.36(2)	0.41(2)	-
	after 200°C anneal	3.27(1)	- 1.66(7)	1.13(11)	- 0.33(4)	0.29(2)	-
	after 400°C anneal	-	-	-	-	0.00(+5)	-
I + II	after implantation	-	-	-	-	-	0.104(4)
	after 200°C anneal	-	-	-	-	-	0.104(4)
	after 400°C anneal	-	-	-	-	-	0.102(3)

7.3 Investigations on DyFe

A. Sources and absorbers

Two sources were made by implanting ^{161}Tb ions into iron foils.
Source I : Implantation energy 130 keV; dose 8(4) × 10^{13} at/cm^2.
Source II: " " 120 keV; " 7(4) × 10^{13} at/cm^2.

An 11 mg/cm^2 absorber of DyF_3 was used at room temperature. In the measurement with source I it was moved sinusoidally with the absorber construction of fig. 4.1. It the measurement with source II the holder of fig. 4.2 was used to give the absorber its sinusoidal

motion. With source I a series of measurements at different temperatures was done with the source mounted in the cryostat in the source holder shown in fig. 4.11. A 3 mm NaI crystal was used as a detector. For the measurements with source II a xenon filled proportional counter was used.

B. Experimental results

a) Source I.

Measurements were done at source temperatures of 5 K, 151 K, 273 K and 363 K. The spectrum obtained at 5 K (see fig. 7.4.a) was fitted with the same hamiltonian as the DyNi spectra measured at 1.3 K and 5 K.

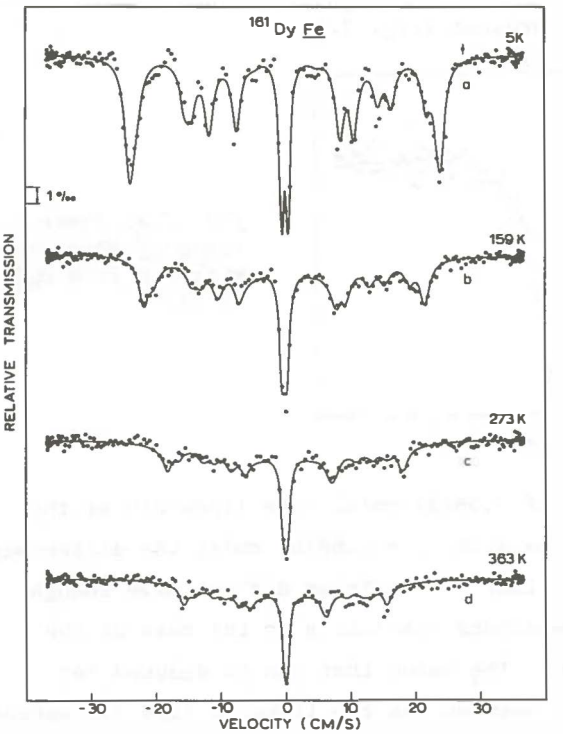

fig. 7.4. Mössbauer spectra from DyFe at different temperatures.

The DyFe spectrum, however, could be fitted well with only one component of 16 Lorentzians. The width of the two inner lines (Γ_1) was again left free with respect to that of the other 14 lines (Γ_2).

The results of the fit are given in table 7.IV.

Table 7.IV

Parameters derived from Mössbauer spectrum of DyFe at 5 K.

$g_N \mu_N H_{hf}$ (cm/s)	$\frac{1}{4}e^2qQ$ (cm/s)	Γ_1 (cm/s)	Isomer shift (cm/s)
4.276(4)	- 2.66(3)	1.66(5)	- 0.12(1)

The errors in this table are statistical. The estimated error in the absolute velocity scale is 2 %. In order to investigate the shape of the central part of the spectrum at 5 K, a measurement was done with strongly reduced velocity. In this spectrum only two lines of the sixteen are present (fig. 7.5).

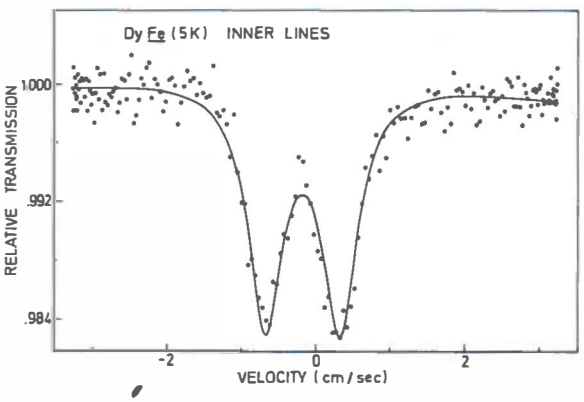

fig. 7.5. Inner lines of Mössbauer spectrum from DyFe (5 K).

These lines have a width of 0.56(2) cm/s. (The linewidth of the two inner lines in fig. 7.4.a is Γ_2 = 0.88(6) cm/s; the difference is mainly due to the fact that the analyzer did not have enough channels to obtain the necessary resolution in the case of the completely split spectrum). The value that can be deduced for $g_N \mu_N H_{hf}$ from the distance between the two lines in fig. 7.5 agrees within limits of error with the value in table 7.IV.

An attempt has been made to fit the spectra measured at 151 K, 273 K and 363 K with only one component, just as the spectrum measured at 5 K. This component was calculated with the relaxation model described in section 3.6, assuming that all Dy ions are substitutional and that the influence of the crystalline electric

field can be neglected with respect to that of the exchange field. This last assumption is justified by the fact that the 5 K spectrum shows no reduction of the hyperfine interaction with respect to the free ion value (see sect. 3.1). The results of these fits are given in fig. 7.6.

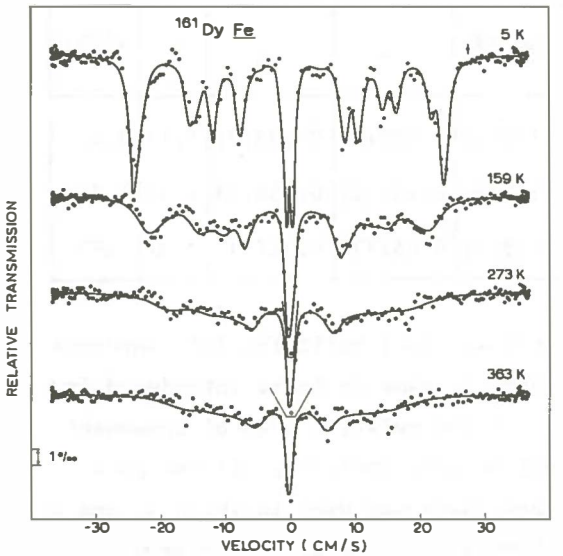

fig. 7.6. Mössbauer spectra from DyFe at different temperatures (one component fits).

As there are systematic differences between the measured and calculated spectra in these one-component fits, the fitting was repeated, assuming the presence of two components in the spectra:

Component I:

A component calculated with the relaxation model from section 2.5, assuming that the electronic sublevel scheme is that of fig. 2.2 in which only two sublevels ($J_z = \pm 15/2$) are populated.

Component II:

A component with fast relaxation. This component was calculated directly, without using the relaxation model, as the sum of the 16 Lorentzians. In section 3.1 we have shown that this procedure is justified in the case of fast relaxation. At each source temperature the reduction of the magnetic hyperfine field R_m was deduced from the reduction of the over all splitting in the spectrum. From this reduction the distance between the electronic sublevels Δ_2 and from Δ_2 the reduction of the quadrupole splitting R_q was then cal-

culated (see fig. 3.3.a).

The results for these two-component fits are given in figs. 7.4.b, c, d and table 7.V.

Table 7.V Parameters from two component fits of DyFe spectra (Two electronic levels for component I)

T(K)	α	π_0 (cm/s)	A_2	Δ_2 (K)	R_m	R_q	χ^2	$\chi^2(1)$
151	0.5(3)	9(6)	0.5(2)	130(5)	0.903(2)	0.738(2)	1.13	2.02
273	0.6(3)	16(8)	0.5(2)	116(5)	0.757(2)	0.450(2)	1.32	1.70
363	0.7(3)	16(8)	0.5(2)	115(5)	0.65(2)	0.32(1)	1.37	1.93

The parameters Δ_2 (electronic level splitting for component II), α and π_0 in this table are the same as those introduced in section 3.1 and 3.5, while A_2 is the relative area of component II. No least squares fit could be made including all the parameters. Therefore a fitting procedure was used in which Δ_2 and A_2 were kept on a fixed value. Then a χ^2-value was calculated for different combinations of α and π_0, to obtain the set α, π_0 for which χ^2 had a minimum value. This procedure was repeated for other values of Δ_2 and A_2.

The errors in table 7.V are chosen in the following way: If the error of a parameter is added to the value given for this parameter, the other parameters can be changed in such a way that χ^2 does not change more than 10 %.

The last column of table 7.V gives the χ^2 values for the fits with one-component model (see fig. 7.6). It can be seen that the two-component fit gave a very significant improvement.

Good fits for the 151 K, 273 K and 363 K spectra could also be obtained if the electronic level scheme for the first component consisted of 16 equidistant lines, just as for the second component, while relaxation with an intermediate frequency between these levels occurred. The relaxation spectrum for the first component was then calculated using the theory outlined in section 3.6. The parameters of these fits are given in table 7.VI.

Table 7.VI Parameters from two-component fits of DyFe spectra (16 electronic levels for component I)

Source temp.	Δ_1 (K)	π_1 (cm/s)	Δ_2 (K)	A_2	χ^2
151	30	4×10^{-3}	132	0.46(10)	1.17
273	30	4×10^{-3}	120	0.46(10)	1.26
363	30	4×10^{-3}	115	0.55(10)	1.43

In this table Δ_1 and Δ_2 are the distances between the electronic sublevels for the first and the second component respectively. $A2$ is the relative intensity of component II, while π_1 is the factor 1/2kD in 2.6.(6). The χ^2-values can be compared to those in the corresponding column of table 7.V. No attempt was made to reduce χ^2 by varying Δ_1, Δ_2 or π_1. For this reason no errors are given in table 7.VI for the values of these parameters.

b) Source II:

With this source measurements were done at 5 K and 77 K directly after implantation. After these two measurements the source was annealed in vacuum for one hour at 600°C and spectra were measured again at 5 K and 77 K. The two spectra obtained at 77 K are given in fig. 7.7. The shape of the two spectra measured at 5 K is the same as that of fig. 7.4.a. These spectra have again been fitted with 16 Lorentzians. The results of these fits are given in table 7.VII.

Table 7.VII Parameters from DyFe Mössbauer spectra measured before and after annealing

Measurement	Source temp.	$g_N\mu_I H_{hf}$ (cm/s)	$\frac{1}{4}e^2qQ$ (cm/s)	Γ_1 (cm/s)	Γ_2 (cm/s)	Isomer shift (cm/s)	A (cm/s)
before anneal	5 K	4.308(4)	- 2.76(3)	1.33(6)	0.65(4)	- 0.31(1)	0.140(4)
after anneal	5 K	4.020(4)	- 2.01(3)	1.22(5)	0.45(2)	- 0.17(1)	0.137(4)
before anneal	77 K	4.192(8)	- 2.45(5)	1.84(9)	0.72(5)	- 0.33(2)	0.115(4)

(A is the total area of the 16 Lorentzians. Γ_2 is the linewidth of the two central lines; Γ_1 of the 14 other lines). The errors in the table are statistical; the error in the absolute velocity scale is about 0.4 % in these measurements.

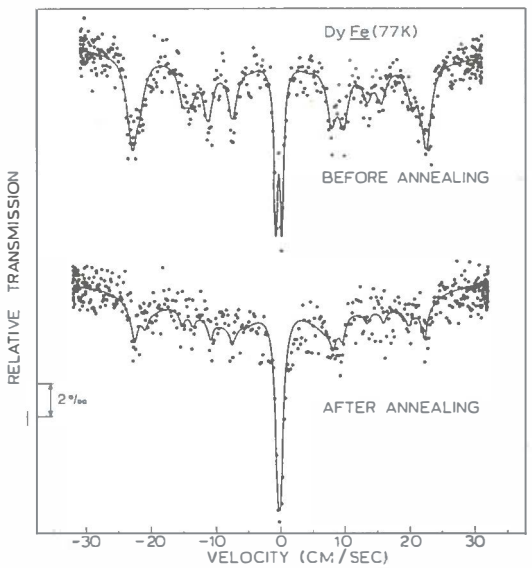

fig. 7.7. Mössbauer spectra from DyFe (77 K) before and after annealing.

Clearly both the hyperfine field and the quadrupole splitting are reduced after annealing. An attempt was made to fit the 5 K spectrum of the unannealed source with two components, one of which with the hyperfine parameters of the annealed source. This procedure, that worked well in the case of DyNi, failed however in this case.

The spectrum measured at 77 K before annealing could also be fitted well with one component of 16 Lorentzians. The results are also given in table 7.VII. The spectrum measured at 77 K after annealing (fig. 7.7) has the same shape as the spectrum obtained for DyNi at 77 K (see fig. 7.3) after annealing. In the same way as for this DyNi spectrum, it could be fitted with two components: One component with very slow relaxation with the same values for $g_N \mu_N H_{hf}$ and $\frac{1}{4}e^2qQ$ as in the spectrum after 600°C anneal. (So the over all splitting in the 5 K and 77 K spectra after annealing are the same). And one component for which the relaxation frequency has the same

order of magnitude as the Larmor-precession frequency of the Dy nucleus. (π_0 = 10 cm/s; α = 0.3). The best fit was obtained with a relative area of about 15 % for the slow relaxation component.

7.4 Investigations on TmNi

A. Sources and absorbers

Measurements were performed with three different sources of ^{169}Er implanted into nickel foils.

Source I : Implantation energy: 140 keV; dose 2(1) $\times 10^{14}$ at/cm^2
Source II : " " : 125 keV; " 1.0(5) $\times 10^{14}$ at/cm^2
Source III: " " : 125 keV; " 1.0(5) $\times 10^{14}$ at/cm^2

Sources I and III were used without further treatment; source II was annealed in a clean vacuum for 1 hour at 400 ± 5°C before use.

As the gamma ray energy (8.401 keV) of ^{169}Tm is close to that of X rays of the nickel host (K_{α_2} = 7.46 keV, K_{α_1} = 7.48 keV and K_{β_1} = 8.3 keV with intensity ratio 50 : 100 : 17), it is impossible to separate the gamma rays from this X ray background with the proportional counters used in the measurements. (Kr- or Xe-filled).

Both Tm metal and $TmAl_2$ were used as absorber material. Properties of these absorbers are given in section 6.1. These absorbers were used at room temperature and in the measurements at high velocities they were moved sinusoidally with the absorber holder of fig. 4.2.

B. Experimental results

a) Source I:

One measurement was done with the source at 5 K (vs. the TmAl absorber). The measured spectrum (fig. 7.8) was fitted with two components, each of which is the sum of six Lorentzians the positions of which are given by:

$$\mathcal{H} = - g_N \mu_N H_{hf} \left(\frac{g_N^*}{g_N} \cdot I_z^* - I_z\right) + \tfrac{1}{4} e^2 q Q^* \left\{\frac{3(I_z^*)^2 - I^*(I^*+1)}{I^*(2I^*-1)}\right\}$$

For $\frac{g_N^*}{g_N}$ the value - 0.74 was used (compare section 6.2). The results of this fit - in which the linewidth of the second component was

kept fixed - are given in Table 7.VIII. The errors in this table are statistical. The estimated error in the velocity scale is 0.5 %.

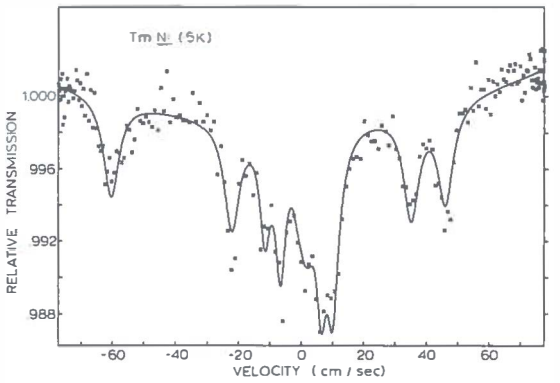

fig. 7.8. Mössbauer spectrum from TmNi (5 K) (unannealed source).

Table 7.VIII

Parameters from TmNi Mössbauer spectrum (unannealed source).

Source temp.	Comp.	$g_N \mu_N H_{hf}$ (cm/s)	$\frac{1}{4} e^2 qQ^*$ (cm/s)	linewidth (cm/s)	Isomer shift (cm/s)	Relative Intensity
5 K	I	32.67(9)	-6.86(12)	5.94(39)	-0.30(12)	0.61(6)
	II	7.44(10)	-1.04(17)	4	-1.05(11)	0.39(6)

The statistics of fig. 7.8 are rather poor. This is the case for all spectra obtained with implanted sources of ^{169}Er. The reason for this is that the conversion coëfficient of the Mössbauer transition in ^{169}Tm is very high ($\sim$ 300), that the implantation dose must be kept low enough to get a dilute source (see section 1.6) and that the Mössbauer line cannot be separated from the X ray background.

A special remark must be made about the line intensities in fig. 7.8. As in the well-known ^{57}Fe-metal Mössbauer spectrum, the line intensities in a magnetically split Tm spectrum should have the ratio 3 : 2 : 1 if the foil is randomly magnetized, or 3 : 4 : 1 when the foil is magnetized perpendicular to the gamma emission.

The parameters in table 7.VIII are obtained from a fit in which the intensity ratios for the second component were kept fixed at 3 : 4 : 1, whereas the intensity ratios of the first component were left free. This ratio turned out to be: 1.77(21) : 1.51(20) : 1. In a fit in which the intensity ratio of lines 1 and 3 was kept fixed to 3 : 1 while that of line 2 was left free, the intensity ratio for the first component became 3 : 3.0 : 1 and for the second component 3 : 3.9 : 1. However, in the last fit the χ^2-value was 2.10, whereas this value was 1.79 in the fit giving the parameters of table 7.VIII. Both fits yielded values for the other parameters that agreed within statistical errors, except for the isomer shift. (In the second fit the isomer shift for the first component was 0.13(13) cm/s and for the second component - 0.33(10) cm/s.

Possibly the intensity anomaly can be explained by relaxation effects in the source after electronic rearrangement (see section 3.8).

b) Source II.

With this annealed source 3 measurements were performed vs. the $TmAl_2$ absorber at room temperature:

a) Source temp. 5 K, velocity scale ± 75 cm/s (see fig. 7.9)
b) Source at RT, velocity scale ± 75 cm/s
c) Source at RT, velocity scale ± 13 cm/s

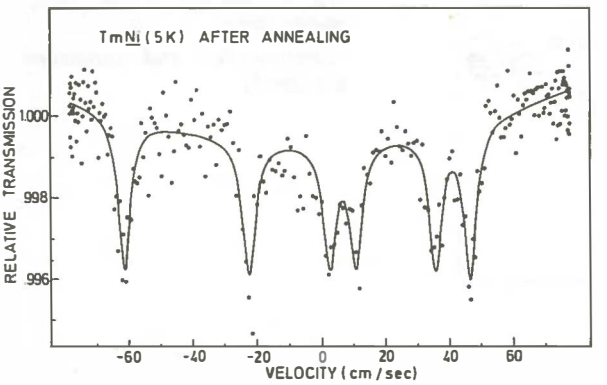

fig. 7.9 Mössbauer spectrum from TmNi (5 K) (annealed source).

The spectrum from measurement a) could be fitted well with one component. (Table 7.IX; errors are statistical, error in velocity scale 0.5 %).

Table 7.IX

Parameters from TmNi Mössbauer spectrum (annealed source)

Source temp.	$g_N \mu_N H_{hf}$ (cm/s)	$\frac{1}{4} e^2 qQ^*$ (cm/s)	linewidth (cm/s)	Isomer Shift (cm/s)	line intensity ratio
5 K	33.13(7)	- 7.04(12)	4.77(31)	- 0.23(10)	1.27(16) : 1.13(15) : 1

Measurements b) and c) both gave broad single lines. Linewidth and position of this line (see fig. 7.10) were: 6.51(26) cm/s and + 0.28(4) cm/s, respectively (results from measurement c)).

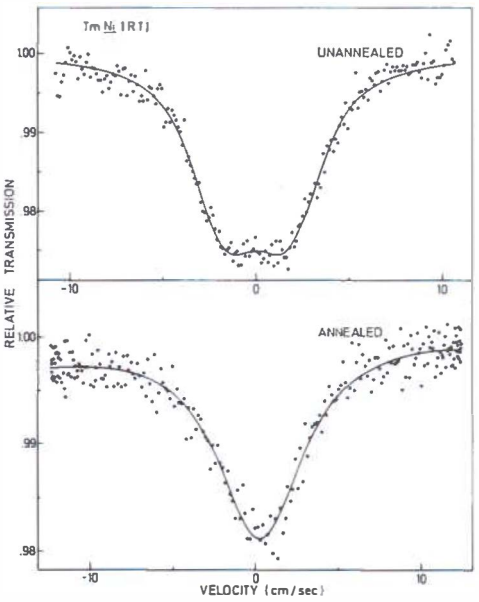

fig. 7.10.
Mössbauer spectrum from TmNi (RT).
(unannealed and annealed source).

c) Source III:

With this source three measurements were made:

a) Source at RT, absorber $TmAl_2$ (RT), velocity scale ± 75 cm/s,

b) Source at RT, absorber Tm-metal (RT), velocity scale ± 11 cm/s,
c) Source at RT, absorber Tm-metal (RT), conversion electron measurement.

The spectrum of measurement a) could be fitted with a broad single line (linewidth: 7.49(43) cm/s, position: 0.20(13) cm/s).

However, with the reduced velocity scale of measurement b) structure could be seen in this line (see fig. 7.10). Therefore a fit was tried with one component of six lines with fixed intensity ratio 3 : 4 : 1 (as for component II in table 7.1). The results are given in table 7.X (errors are statistical; due to an experimental mistake, the error in the absolute velocity scale is about 10 %).

Table 7.X

Parameters from TmNi Mössbauer spectrum measured at RT (unannealed source)

Source temp.	$g_N \mu_N H_{hf}$ (cm/s)	$\frac{1}{4} e^2 q Q^*$ (cm/s)	linewidth (cm/s)	isomer shift (cm/s)
293 K	1.58(2)	0.01(4)	3.50(14)	0.02(2)

Measurement c), with a conversion electron detector, showed that this method cannot compete with the conventional transmission method for Tm Mössbauer measurements.

7.5 Investigations on TmFe

A. Sources and absorbers

Measurements have been done with three different sources of ^{169}Er implanted into iron foils.

Source I : Implantation energy: 130 keV; dose 1.4(7) × 10^{14} at/cm^2
Source II : " " : 130 keV; dose 0.4(2) × 10^{14} at/cm^2
Source III: " " : 140 keV; dose 0.4(2) × 10^{14} at/cm^2

As in the case of TmNi the Mossbauer gamma ray could not be separated completely from the X ray background of the host (K_{α_1} = 6.39 keV; K_{α_2} = 6.40 keV; K_{α_3} = 7.1 keV; intensity ratio 50 : 100 : 16)

with the krypton filled proportional counter used for the measurements.

In all the measurements the $TmAl_2$ absorber (see section 6.1) has been used at room temperature. In the measurement with source I it was moved with the mechanical drive described in section 4.2. In the measurements with sources II and III it was moved sinusoidally with the absorber holders of fig. 4.1 and fig. 4.2, respectively.

B. Experimental results

a) Source I:

One measurement has been done with the source at 5 K. The measured spectrum (see fig. 7.11.a) has been fitted with one component of six Lorentzian lines, described by the same hamiltonian as given in section 7.4.

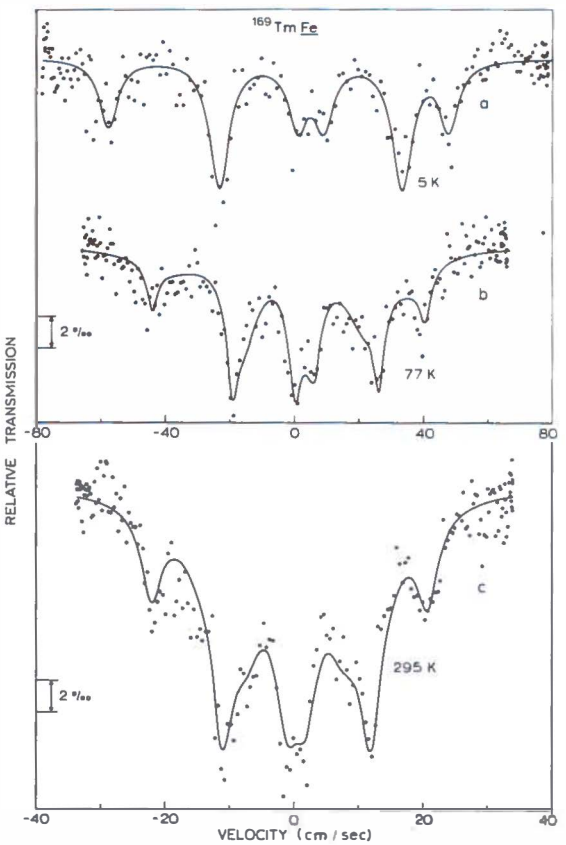

fig. 7.11 Mössbauer spectra from TmFe (two component fits).

Results of the fit (with statistical errors) are given in Table 7.XI. The estimated error in the absolute velocity scale is about 1.5 %.

Table 7.XI

Parameters from Mössbauer spectrum of TmFe at 5 K

Source temp.	$g_N \mu_N H_{hf}$ (cm/s)	$\frac{1}{4} e^2 q Q^*$ (cm/s)	Linewidth (cm/s)	Isomer shift (cm/s)	Line intensity ratio
5 K	32.40(17)	- 4.99(28)	7.09(55)	- 0.06(19)	1.08(22) : 2.06(35) : 1

b) Source II:

One measurement was done with the source at room temperature. An attempt was made to fit the measured spectrum with one component, assuming relaxation between 13 equidistant electronic energy levels (see section 3.6). The result of this attempt can be seen in fig. 7.12.

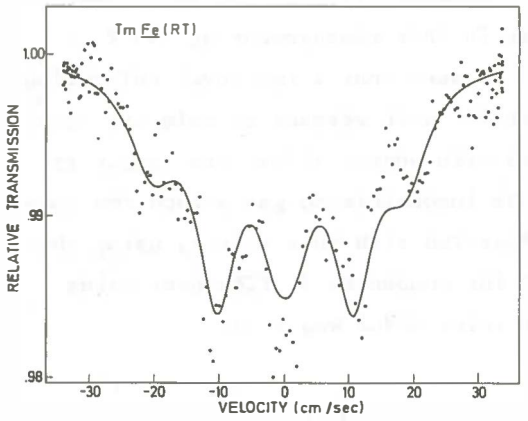

fig. 7.12
Mössbauer spectrum from TmFe (RT), one component fit.

From this figure it is clear that the spectrum cannot be fitted with one component of the type described above. Therefore a two-component fit was made (see fig. 7.11.c). In this fit fast relaxation between 13 equidistant electronic levels (distance Δ_2) is supposed for the second component (compare section 7.3).
For the first component relaxation with an intermediate frequency, also between 13 equidistant levels (distance Δ_1) has been taken.

The parameters of this fit are given in table 7.XII. In the table Γ_1 and Γ_2 are the linewidths of the first and second component, respectively. These widths were kept fixed in the fitting procedure. A_2 is the relative intensity of component II.

Table 7.XII

Parameters from TmFe Mössbauer spectra (two component fits)

Source temp.	Δ_1 (K)	π_1 (cm/s)	Γ_1	Δ_2 (K)	Γ_2 (cm/s)	A_2	χ^2	$\chi^2(1)$
293 K	37(10)	$1.0(^{+9.0}_{-0.5})$	6	56(5)	4	0.5(2)	1.33	1.94
77 K	27(7)	$0.20(^{+0.40}_{-0.16})$	6	47(5)	4	$0.3(^{+0.3}_{-0.1})$	1.29	1.43

π_1 is the factor 1/2kD in 3.6.(6). (For the second component the corresponding π_2 was taken very high). The errors in the parameters were obtained in the same way as in table 7.V. $\chi^2(1)$ is the chi-square value for the one component fit. The estimated error in the absolute velocity scale in this measurement at 293 K is about 1 %. In fig. 3.7 it can be seen that a two-level relaxation spectrum for Tm^{3+} is not symmetric with respect to velocity zero. However, the spectrum measured with source II has its center at velocity zero. Therefore it was impossible to get a good two component fit for the spectrum measured with this source, using the two-level model (section 3.5) for component I. (The best value obtained for χ^2 with this two level model was 1.9).

c) Source III:

One measurement was done with the source at 77 K. The spectrum was also fitted with one component (13 equidistant electronic levels) and with two components (two sets of 13 levels) just as the spectrum measured at RT. The result of the two-component fit is given in fig. 7.11.b and the corresponding parameters in table 7.XII. In this measurement the estimated error in the absolute velocity scale is about 1 %.

CHAPTER 8

DISCUSSION

8.1 Lattice location

After implantation rare earth ions can occupy purely substitutional or non-substitutional sites in the iron or nickel lattice. Channeling experiments have shown that only about one half of isotope separator implanted rare earth ions occupy substitutional sites in iron and that this substitutional fraction is gradually reduced to zero on annealing to 500°C. This behaviour is shown in fig. 8.1, taken from the work of Abel et al. [1] and Alexander et al. [2]. A change of site also follows from IPAC (Integral Perturbed Angular Correlation) measurements [1 - 4].

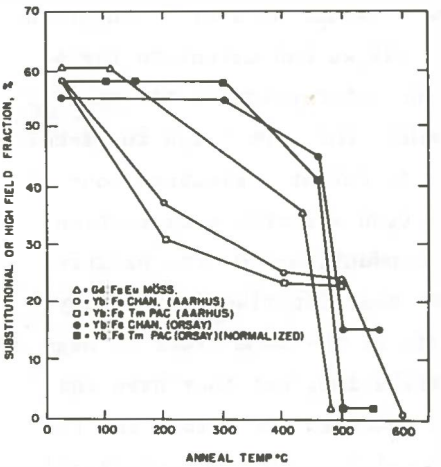

fig. 8.1.
Composite plot of Mössbauer, channeling and IPAC results on the substitutional fraction of rare earth ions in iron versus annealing temperature. (Taken from ref. [4])

The above conclusions cannot be drawn straightforwardly from our measurements with samples of DyFe and TmFe because the spectra do not clearly show the existence of more than one component. The measurements with DyNi and TmNi sources, however, give unambiguous results because here two components can be seen in the spectra. We will treat the DyNi spectra first.

DyNi. After the first annealing step (at 200°C) of the source described in Section 7.3.c, the relative intensity of the component with the lowest magnetic splitting ($g_N \mu_N H_{hf}$ = 3.28(3) cm/s; H_{hf} = 4.72(14) MOe) has been reduced from 41 % to 29 %. (The error in

H_{hf} for the Dy samples is mainly caused by the error in μ_g = − 0.472(13) μ_N). After the second annealing (at 400°C) the relative intensity of this component is smaller than 5 %, whereas that of the other component ($g_N\mu_N H_{hf}$ = 4.07(2) cm/s; H_{hf} = 5.85(17) MOe) has grown to more than 95 %. This annealing behaviour can be explained by assuming that the disappearing component is associated with purely substitutional Dy ions. During the annealing process lattice defects in the nickel move and can be trapped by such a substitutional rare-earth ion, changing this ion into a non-substitutional one. From lattice damage experiments [5] we can conclude that the non-substitutional sites consist of impurity-vacancy clusters, because mono and divacancies become mobile in the temperature range where the annealing treatments were done, while vacancy loops are not mobile below 450°C. From the value A = −114.1(2.8) MHz of the hyperfine constant of a Dy^{3+} ion given by Abragam and Bleaney (see section 1.3) we can calculate the 4f contribution to the free ion hyperfine interaction to be: $g_N\mu_N H_{hf}$ = 4.14(11) cm/s ($H_{hf}^{(4f)}$ = 5.95(24) MOe). For a Dy^{3+} ion in nickel this value must be corrected for the different s electron contributions: core polarization, conduction electron polarization due to the 4f moment of the ion and conduction electron polarization due to the host. In nickel the host contribution is very small. The other two contributions are of the same order of magnitude, a few percent of the 4f contribution, but they have the opposite sign. Nowik et al. [6] have compared the values for the hyperfine field for different intermetallic compounds of Dy and Ni (DyNi, $DyNi_2$, $DyNi_5$) to that for Dy metal. Within their experimental error (2 %) they find no difference for all these values. For these reasons we neglect the s contribution to the hyperfine field for a Dy^{3+} ion in nickel for which $\langle J_z \rangle = J$.
For Dy metal we have measured $g_N\mu_N H_{hf}$ = 4.036(11) cm/s (H_{hf} = 5.80(16) MOe). So we can conclude that the hyperfine field in Dy metal and in the intermetallic compounds mentioned above agrees within limits of error with the free ion hyperfine field $H_{hf}^{(4f)}$. This means that the s contribution is negligible in these cases too, as we have supposed for DyNi. (At least, as long as the error in the value for the hyperfine constant A is of the

same order of magnitude as the s contribution).

The hyperfine field measured for the component in DyNi with the highest field also has the free ion value given above. We expect this value for the hyperfine field, if this component is generated by Dy^{3+} ions that are in a crystalline electric field with a strong axial component, such as to be expected for a Dy^{3+} ion associated with one or more vacancies (section 3.1.B). The value measured for the hyperfine field of this non-substitutional component in itself does not exclude the possibility of clustering of Dy ions during the annealing process as suggested by Bernas [7] for Yb in Fe during high temperature annealing. However, the value measured for the quadrupole splitting of this component, 2.83(4) cm/s after the 200°C anneal and 2.47(4) cm/s after the 400°C anneal, is definitely smaller than that for Dy metal (3.158(9) cm/s; section 5.2).

The fact that the hyperfine field of the non-substitutional component of a DyNi source that has not been annealed, does not change with temperature (see table 7.II) can also be described with the two electronic level model of section 3.1.B with very slow relaxation between the two levels $J_z = \pm 15/2$.

In the spectrum measured at 77 K after annealing at 400°C (see fig. 7.3) this slowly relaxing component is still present together with a component showing a typical relaxation pattern. Actually one must expect this spectrum to consist of several components, because different vacancy clusters around a Dy ion are possible, each with its own relaxation frequency.

The same situation exists before annealing: The non-substitutional component of the spectrum corresponds to several different rare earth-vacancy clusters with different relaxation frequencies. This explains the increase of the linewidth with temperature and the extra single line at room temperature (see table 7.II).

From the value of α, the ratio of the population of the two electronic levels $J_z = \pm 15/2$, in the fit for the spectrum of fig. 7.3 the separation between these levels can be calculated as explained in section 3.4: $\Delta_1 \approx 70$ K. This gives an exchange field at the site of a non-substitutional Dy ion in nickel with a

strength of about 0.2 MOe.

The substitutional component in the DyNi spectra measured at different temperatures (given in fig. 7.1) shows very fast relaxation: the lines remain narrow and the hyperfine field and the quadrupole splitting decrease with increasing temperature. For this component the influence of the crystalline electric field has to be taken into account. This temperature behaviour will be treated in a separate section (8.3).

TmNi. The 4f contribution to the free ion hyperfine field for Tm^{3+} can be calculated in the same way as for Dy^{3+}. From the hfi constants given by Abragam and Bleaney (A_J = - 393.5 MHz and A'_S = - 6.5(8) MHz) we find $A = A_J + A'_S$ = -400.0(4.8) MHz. Abragam and Bleaney do not give the error in the value for A_J. It is reasonable to estimate this error to be about 1 % [8]. From the value for A we calculate the 4f contribution to the free Tm^{3+} ion hyperfine interaction to be: $g_N\mu_N H_{hf}$ = 35.4(4) cm/s ($H_{hf}^{(4f)}$ = 6.81(9) MOe). Using the same arguments as for DyNi, we suppose this value also to be the hyperfine field for a Tm^{3+} ion in nickel for $\langle J_z \rangle = J$.

The field value H_{hf} = 6.40(4) MOe ($g_N\mu_N H_{hf}$ = 33.26(9) cm/s) measured for Tm metal is 6 % smaller than the free ion value. (An explanation of this reduction has been given by Cohen [9]). Since no measurements have been done so far on Tm-nickel intermetallic compounds, no comparison can be made to the hyperfine field in such compounds as in the case of Dy. The hyperfine field measured at a source temperature of 5 K for the component in TmNi with the higher field is 6.29(7) MOe ($g_N\mu_N H_{hf}$ = 32.67(26) cm/s, see table 7.VIII). Just as in DyNi, this component is supposed to be due to non-substitutional impurities. The component with the lower field must be due to substitutional Tm ions. This is confirmed by the fact that this substitutional component is not present in the spectrum measured at 5 K of the annealed TmNi source (fig. 7.9). For this annealed source within the errors the same value is measured for the hyperfine interaction ($g_N\mu_N H_{hf}$ = 33.13(24) cm/s) as for the highest field in the unannealed source. The last value is the same as that measured for Tm metal at 5 K ($g_N\mu_N H_{hf}$ = 33.26(9) cm/s). Also the values found for the quadrupole splitting at 5 K,

6.86(16) cm/s for the high field component of the unannealed source and 7.04(16) cm/s for the annealed source agree within the error limits, and the last value agrees with that measured for Tm metal ($\frac{1}{4}e^2qQ^* = 7.13(5)$ cm/s).

An explanation for the values measured at 5 K for the hyperfine field and quadrupole splitting of the non substitutional component in TmNi can be sought in different directions. A first possible explanation would be that this component is caused by Tm ions that form clusters in the nickel host. This assumption is unlikely for an unannealed source for then clustering should have taken place during implantation. After annealing a broad single line (width 6.5(3) cm/s) was measured versus the $TmAl_2$ absorber at room temperature. This line is much broader than the lines measured with a single line source and a Tm metal absorber (see table 6.II); this is an indication that the spectrum from the annealed source is not that of Tm metal. So apparently after annealing no Tm metal like clusters are formed in the nickel. A second explanation is that the axial crystalline electric field at the site of the non-substitutional Tm ion is not completely dominated by the diagonal operators O_2^0, O_4^0, O_6^0, but that at least one non diagonal operator cannot be neglected. In that case the expectation values $|\langle J_z \rangle|$ and $\langle J_z^2 \rangle$ are reduced, leading to lower than free ion values of the hyperfine field and quadrupole splitting.

For the implants of Dy or Tm into iron the interpretation of the measured spectra in terms of different components is less straightforward. In the spectra measured with a source of DyFe or TmFe at 5 K only one component is seen. We will discuss the DyFe results first.

DyFe. The value measured for the hyperfine field at 5 K: $|H_{hf}| = 6.20(18)$ MOe ($g_N\mu_N H_{hf} = 4.31(2)$ cm/s) is 3.4 % larger than the calculated 4f contributions to the free ion value. Starting from this 4f contribution ($g_N\mu_N H_{hf}^{(4f)} = +\ 4.14(11)$ cm/s), the hyperfine field for Dy^{3+} in iron can be calculated in the same way as by Niesen and Kikkert [10] for ErFe: For DyFe the important s

contributions to the hyperfine interaction are:

a) core polarization + relativistic effects: - 0.17(2) cm/s (calculated from the value given for A_S' by Abragam and Bleaney; see section 1.3),

b) conduction electron polarization due to the 4f moment: - 0.17(3) MOe ≙ + 0.12(2) cm/s (this contribution is proportional to $(g_J - 1)J$),

c) conduction electron polarization due to the host: - 0.27(6) MOe ≙ + 0.19(5) cm/s.

This gives a total value $|H_{hf}|$ = 6.15(34) MOe for the hyperfine field for Dy^{3+} in iron ($g_N\mu_N H_{hf}$ = 4.28(30) cm/s) which agrees well with the measured value.

For the annealed DyFe source a hyperfine field $|H_{hf}|$ = 5.78(18) MOe ($g_N\mu_N H_{hf}$ = 4.02(2) cm/s) was measured at 5 K. This value is within the (rather small) error the same as that for Dy metal and it is 6.7(9) % smaller than the field measured for the unannealed DyFe source.

An explanation might be that the spectrum of the annealed DyFe source is caused by clusters of Dy metal. However, the quadrupole splitting for the annealed source (2.01(4) cm/s) is much smaller than the splitting for Dy metal (3.158(9) cm/s) and also smaller than the splitting for the unannealed DyFe source (2.76(4) cm/s).

For the intermetallic compound $DyFe_2$ a hyperfine field of 6.47 MOe is measured at the Dy-site [11], even larger than for the unannealed DyFe source. So we cannot explain the field in the annealed source either by assuming that it is caused by formation of $DyFe_2$.

A good explanation for the values measured for the hyperfine field and the quadrupole splitting of the annealed source is that the spectrum is generated by Dy ions associated with vacancies and that for these Dy ions $|\langle J_z \rangle|$ and especially $\langle J_z^2 \rangle$ have been reduced by the influence of non diagonal crystalline electric field operators as in the DyNi case.

An attempt to fit the spectrum of the unannealed DyFe source (measured at 5 K) with two components failed, when the values for the hyperfine field and the quadrupole splitting for one of the components were kept fixed at the values measured for the annealed

source. This proves that the high temperature anneal has also changed the character of the non-substitutional sites. A careful inspection of the values of the hyperfine field and quadrupole splitting of the non substitutional component of DyNi (component I) in table 7.III also leads to the conclusion that the highest temperature anneal (400°C) has changed the non substitutional component.

The existence of two components in the spectrum of the unannealed DyFe source can be deduced from the spectra measured at higher temperatures. In section 7.3 it was already shown that a one component fit for these spectra gave bad results (see fig. 7.6), while very reasonable results were obtained with two component fits. In these two component fits the component with very fast relaxation is supposed to be due to substitutional impurities as in DyNi. For the non-substitutional component good results were obtained both for the electronic level scheme of fig. 3.1 (equidistant levels) and that of fig. 3.2 (doublets, expected for impurities in a strong axial field). So this component in the unannealed DyFe source may be caused by Dy ions associated with vacancies. From the values for α given in table 7.V we calculate Δ_1 = 120(69) K for the splitting of the doublet $J_z = \pm 15/2$. From this value we can calculate the exchange field in iron at the site of the non substitutional Dy ions: H_{exch} = 0.33(17) MOe. (The exchange field calculated for the non-substitutional component in DyNi has the same order of magnitude: 0.2 MOe).

From the values given for Δ_2 in table 7.V the exchange field at the site of a substitutional Dy ion van be calculated for T = 0 K if we assume that Δ_2 is proportional to the iron magnetization.

We find $H^{(0)}_{exch}$ = 5.49(15) MOe. This value is not much different from that derived from the measurements performed by Bowden et al. [12] with the intermetallic compound $DyFe_2$, which has a cubic Laves structure: $H^{(0)}_{exch}$ = 6.03 MOe. (In $DyFe_2$ each Dy ion has 12 nearest Fe neighbours at a distance of 3.1 Å; a Dy ion that is substitutionally implanted in iron is surrounded by 8 Fe atoms).

The hyperfine field of 4.69(14) MOe that we have measured for the substitutional component in DyFe at room temperature ($g_N \mu_N H_{hf}$ = 3.26(3) cm/s) is much larger than the field 2.0(3) MOe found by

Grodzins et al. [13] from IMPACT measurements. In this case the influence of the "transient field" [14] can be neglected. (This effect would enlarge the value found by Grodzins et al. for H_{hf} with only 2 %). Possibly one or more of the assumptions made by Grodzins et al. to calculate the hyperfine field from their IPAC (Integral Perturbed Angular Correlation) measurement are not fullfilled.

TmFe. We will conclude this discussion of lattice location by comparing the results discussed up to now to those obtained for TmFe. For TmFe a hyperfine field of 6.23(14) MOe ($g_N\mu_N H_{hf}$ = 32.4(7) cm/s) is measured at 5 K for an unannealed source. In the same way as for DyFe, the value for the hyperfine field at the Tm^{3+} nucleus in iron can be calculated, starting from the 4f contribution: $g_N\mu_N H_{hf}^{(4f)}$ = 35.4(4) cm/s if $\langle J_z \rangle = J$.

In this case the s contributions are:

a) core polarization + relativistic effects: - 0.58(7) cm/s (From the value given for A_S' by Abragam and Bleaney; see section 1.3),
b) conduction electron polarization due to the 4f moment: - 70(15) kOe ≙ + 0.36(8) cm/s,
c) conduction electron polarization due to the host: - 270(69) kOe ≙ + 1.40(31) cm/s.

This gives a total calculated value $|H_{hf}|$ = 7.04(18) MOe for the hyperfine field ($g_N\mu_N H_{hf}$ = 36.6(9) cm/s). For DyFe the value for the hyperfine field calculated in this way agreed well with the measured value, but for TmFe the measured value is 11(4) % lower than the calculated value. This reduction can be caused by the fact that in this case the influence of the crystalline electric field cannot be neglected with respect to the exchange field as was done for DyFe. In section 8.3 we will discuss this influence on the TmFe hyperfine field. There also the measurements done at higher source temperatures will be discussed. From the fact that the spectra obtained at higher source temperatures cannot be fitted with one component, the conclusion can be drawn that also in TmFe at least two components are present in the spectrum. Again we assume one of these components to be due to substitutional impurities and one to non-substitutional impurities. In this case it is striking to see

that no good fit can be obtained if the electronic level scheme of fig. 3.2 (doublets) is taken for the non substitutional component, while reasonable fits can be obtained with the level scheme of fig. 3.1 (13 equidistant levels). From this result we learn that the assumptions leading to the doublet level scheme are not justified for TmFe (For DyFe it does work).

Because no measurements have been done with an annealed TmFe source, no conclusions can be drawn about the lattice location of the Tm ions in such a source. It would be interesting to do such a measurement, because one would like to compare the hyperfine field and the quadrupole splitting for an annealed TmFe source to the field in Tm-metal, as for the annealed DyFe source.

In table 8.I the values for the hyperfine fields discussed in this section are summarized.

Table 8.I

Hyperfine fields and quadrupole splitting for non-substitutional components in DyNi and TmNi, for DyFe before and after anneal and for TmFe. Also given are the hyperfine fields and quadrupole splittings for Dy metal and Tm metal (all values are measured at ∿ 5 K) and the calculated values for the hyperfine field in nickel and in iron.

Source or absorber	$g_N \mu_N H_{hf}$ (cm/s)	$\lvert H_{hf} \rvert$ (MOe)	$\lvert \frac{1}{4} e^2 q Q^{(*)} \rvert$ (cm/s)
DyNi, before anneal	4.07(2)	5.85(17)	2.84(5)
DyNi, after 400°C anneal	4.05(2)	5.82(17)	2.47(4)
DyFe, not annealed	4.31(2)	6.20(18)	2.76(4)
DyFe, after 600°C anneal	4.02(2)	5.78(18)	2.01(4)
Dy metal	4.036(11)	5.80(16)	3.158(9)
Dy^{3+} in nickel (calculated)	4.14(11)	5.95(24)	-
Dy^{3+} in iron (calculated)	4.28(20)	6.15(34)	-
TmNi, not annealed	32.67(26)	6.29(7)	6.86(16)
TmNi, after 400°C anneal	33.13(24)	6.37(7)	7.04(16)
TmFe, not annealed	32.4(7)	6.23(14)	4.99(35)
Tm metal	33.26(9)	6.40(4)	7.13(5)

(Table 8.I continued)

Source or absorber	$g_N \mu_N H_{hf}$ (cm/s)	$\lvert H_{hf} \rvert$ (MOe)	$\lvert \frac{1}{4} e^2 qQ^{(*)} \rvert$ (cm/s)
Tm^{3+} in nickel (calculated)	35.4(4)	6.81(9)	-
Tm^{3+} in iron (calculated)	36.6(9)	7.04(18)	-

8.2 Oxidation of sources

Cohen et al. [4] concluded from their Mössbauer spectra of one source of ^{151}EuFe that the implanted ^{151}Gd ions are "internally oxidized", because they observed a spectrum component that can be ascribed to Eu^{3+} in an oxide environment.

In none of our 5 sources of Dy or Tm implanted into iron and in none of our 6 sources of the same isotopes implanted into nickel evidence was found for this internal oxidation. not even after annealing of some of these sources. A component in the spectrum that can be ascribed to Dy_2O_3 or Tm_2O_3 was never observed.

Mössbauer spectrum of Dy_2O_3:

This spectrum was measured by Wickman and Nowik [17] with a $^{161}Tb_2O_3$ single line source at an absorber temperature of 4.2 K. The spectrum has the same shape as that of Dy metal, but the magnetic splitting ($g_N \mu_N H_{hf}$ = 3.53 cm/s) is reduced to 87 % of the splitting for Dy metal and the quadrupole splitting of Dy_2O_3 ($\frac{1}{4} e^2 qQ$ = 1.41 cm/s) is 45 % of the corresponding value for the metal.

Mössbauer spectrum of Tm_2O_3:

Barnes et al. [18] have measured this spectrum with a $^{169}ErF_3$ single line source. The spectrum is a doublet of lines with equal intensity, that lie almost symmetrical with respect to zero velocity. The splitting of the doublet is 7.2 cm/s at 5 K and at 77 K. At room temperature the splitting has been reduced to 2.8 cm/s.

An important difference between the source preparation of Cohen et al. and our source preparation is the difference in

implantation energy. The energy used by Cohen et al. (50 keV) is much lower than our implantation energy (∿ 120 keV), resulting in a much smaller penetration depth of the implanted ions. Another difference is the somewhat higher dose in the EuFe source (4×10^{14} cm^{-2}).

A simple explanation for Cohen et al.'s results may be that an oxide layer was formed on the iron foil used for the source, perhaps during implantation by a bad vacuum in the isotope separator.

Thomé et al. have shown that "internal oxidation" does not occur in the case of high energy RE implants in iron [15]. However, when oxygen is implanted in the vicinity of rare earth ions already implanted into iron, the two impurities can interact [16]. This interaction is found to be enhanced upon annealing.

8.3 Influence of the crystalline electric field

In Chapter 2 it has been shown that the crystalline electric field can cause a reduction of the hyperfine field and the quadrupole splitting for a Dy or Tm ion that is substitutionally implanted in nickel or iron. We have observed a reduction for the substitutional component in the DyNi and TmNi spectra and in the spectra of TmFe (see section 8.1). In the following discussion we will try to draw some conclusions about crystal field parameters from the measured reductions. In order to derive values for the crystal field parameters C_4 and C_6 we use the expressions (see section 2.4):

$$C_4 = \frac{B_4}{\beta_J} = A_4 \langle r^4 \rangle = \frac{Wx}{F(4) \cdot \beta_J} \qquad (1)$$

and

$$C_6 = \frac{B_6}{\gamma_J} = A_6 \langle r^6 \rangle = \frac{W(1-|x|)}{F(6) \cdot \gamma_J} \qquad (2)$$

Table 8.II gives a survey of the results obtained from susceptibility and EPR measurements performed by Williams and Hirst [19] on samples of several rare earth isotopes in the f.c.c. noble metals gold and silver. Also the results obtained by Davidov et al. [20] for DyAu, by Guertin et al. [21] and Devine et al. [22]

for DyPd (also an f.c.c. metal) and by Praddaude [23] for ErPd are given in table 8.II. The values for $F(4)$, $F(6)$, β_J and γ_J have been given by Lea et al. [24].

Table 8.II

Survey of results obtained from susceptibility and E.P.R. measurements on samples of several rare earth isotopes in different metals, using crystal field theory.

Sample	Ref.nr.	W (K)	x	C_4 (K)	C_6 (K)	C_4/C_6
TbAg	19	- 0.63	+ 0.82	- 70	+ 13	- 5.4
TbAg	19	+ 0.44	+ 0.57	- 70	+ 13	- 5.4
HoAg	19	- 0.37	- 0.37	- 70	+ 13	- 5.4
ErAg	19	+ 0.56	- 0.33	- 70	+ 13	- 5.4
TmAg	19	- 0.55	+ 0.62	- 35	+ 5	- 7.0
DyAu	20		+ 0.85	< 0	> 0	
ErAu	19	+ 0.27	- 0.33	- 32	+ 6	- 5.3
TmAu	19	- 0.27	+ 0.69	- 19	+ 2	- 9.5
YbAu	19	+ 3.7	+ 0.75	- 27	+ 5	- 5.4
DyPd	21,22	- 0.09	- 0.42	- 11	- 3.6	+ 3.1
ErPd	23	- 0.16	+ 0.47	- 28	- 3.0	+ 0.3

In a point charge model C_4 and C_6 are given by:

$$C_4 = + \frac{7}{32} \frac{Ze^2}{R^5} \langle r^4 \rangle \tag{3}$$

$$C_6 = + \frac{39}{256} \frac{Ze^2}{R^7} \langle r^6 \rangle \tag{4}$$

for an f.c.c. metal [19], if (positive) charges Ze coordinate the rare earth ion. (R is the distance of the coordinating charges).

For a b.c.c. metal the corresponding expression are [24]:

$$C_4 = + \frac{7}{18} \frac{Ze^2}{R^5} \langle r^4 \rangle \tag{5}$$

$$C_6 = - \frac{1}{9} \frac{Ze^2}{R^7} \langle r^6 \rangle \tag{6}$$

The expectation values of $\langle r^4 \rangle$ and those of $\langle r^6 \rangle$ are not expected to differ greatly among the heavier rare earths, as shown for trivalent ions by Freeman and Watson [25]. Then, a crystal field model (where the field set up by the lattice is supposed to be independent of the probe ion) would imply that the values of C_4 and those of C_6 should be the same for different rare earths in a given matrix.

From table 8.II we learn that the order of magnitude of C_4 and of C_6 is the same for the different samples studied. The signs of C_4 and C_6, however, are not in accordance with the prediction given by the point charge model. The fact that C_4 is negative for the samples studied by Williams and Hirst, whereas the point charge model predicts a positive sign for C_4, is explained by these authors on the basis of a partially filled $5d$ virtual bound state at the site of the rare earth impurity. This leads to a negative contribution to C_4 that is sufficiently large to overcome the positive point charge contribution. But it does not give a contribution to the sixth harmonic crystal field. We see, however, that for Dy and Er in palladium both C_4 and C_6 have a negative sign. Perhaps the analysis of our own results will solve the puzzle. For this analysis we will use the results obtained with the DyNi and TmNi sources. After this we will discuss the results obtained for the TmFe sources.

From the values given in section 8.1 for the magnetic splitting of the substitutional component in DyNi at 5 K and for a "free" Dy ion in nickel, we can calculate the reduction of $\langle J_z \rangle$ caused by the influence of the crystalline electric field: $R_m = 0.79(3)$ (see section 2.5) Taking the average of the value $\frac{1}{4}e^2qQ = 3.1(3)$ cm/s measured by Nowik et al. [6] for the quadrupole splitting of DyNi, $DyNi_2$ and $DyNi_5$ and the quadrupole splitting of Dy metal (3.158(9) cm/s) we estimate the free ion value for the quadrupole splitting of Dy in a cubic metal to be 3.12(12) cm/s. Our measured quadrupole splitting of 1.69(2) cm/s for the substitutional component in DyNi at 5 K implies a reduction of the quadrupole splitting by a factor: $R_q = 0.54(3)$. If we introduce the values calculated for R_m and R_q in fig. 2.2, combinations of values for the parameters x and y (see 2.4.(1)) can be found for which both R_m and R_q lie

within the range defined by their errors. In this way an "allowed" area in the xy plane is found. This area is given in fig. 8.2, both for positive and negative values of W.

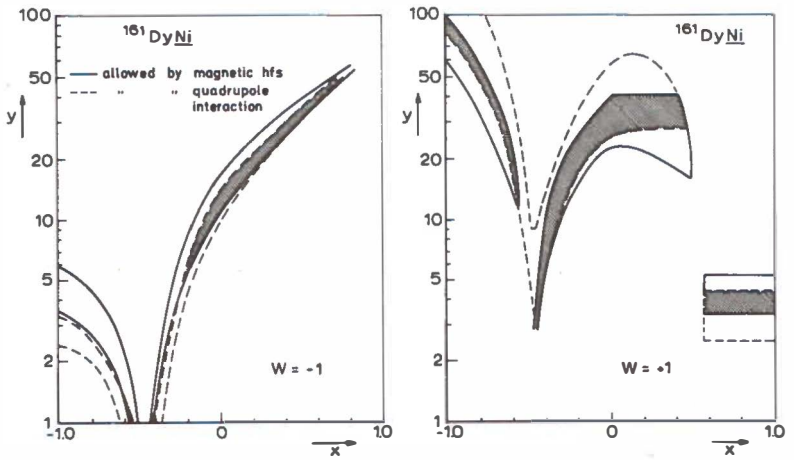

fig. 8.2 Plot of values of x and y allowed by the measured magnetic splitting of DyNi and allowed by measured quadrupole interaction. The overlap between the regions gives the allowed xy combinations.

The temperature behaviour of the magnetic and quadrupole splitting of the substitutional component in DyNi (see table 8.III) has been analyzed by Tiekstra [26]. His results on the basis of the theory outlined in section 2.7 reduces the allowed area to that given in fig. 8.3.

Table 8.III

Reduction of hyperfine field and quadrupole splitting as a function of temperature for the substitutional component in DyNi. ($H_{rel} = H(T)/H(0)$; $Q_{rel} = q(T)/q(0)$).

T(K)	$g_N\mu_N H_{hf}$ (cm/s)	$\frac{1}{4}e^2qQ$ (cm/s)	H_{rel}	Q_{rel}
5	3.232(4)	1.66(2)	1.000	1.00
13	3.244(4)	1.66(3)	1.004(2)	1.00(3)
22	3.140(4)	1.40(3)	0.972(2)	0.84(3)
57	2.20(1)	0.60(5)	0.681(4)	0.36(4)
77	1.96(1)	0.43(6)	0.606(4)	0.26(4)
293	0.66(1)	0.11(4)	0.204(4)	0.07(3)

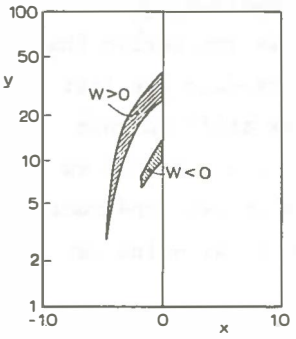

fig. 8.3. Allowed xy combinations for DyNi

To construct this area the following criterion has been used: The scale factor W describing the measured reduction of the magnetic splitting with rising temperature should not differ more than 20 % from the scale factor W describing the temperature behaviour of the quadrupole splitting. By combining the results given in fig. 8.3 with table 8.IV, that gives the possible sign combinations of the crystal field parameters W, x, C_4 and C_6 for Dy^{3+} and Tm^{3+}, we can exclude the combination $C_4 > 0$; $C_6 < 0$ and also the combinations $C_4 < 0$, $C_6 > 0$ that is found for the rare earths in f.c.c. noble metals (see table 8.II). The largest allowed area in fig. 8.3 ($W > 0$, $x < 0$) yields the combinations $C_4 > 0$, $C_6 > 0$ predicted by the point charge model for an f.c.c. metal.

Table 8.IV

Possible sign combinations of crystal field parameters for Dy^{3+} and Tm^{3+}.

Ion	W	x	C_4	C_6
Dy^{3+}	+	+	−	+
	+	−	+	+
	−	+	+	−
	−	−	−	−
Tm^{3+}	+	+	+	−
	+	−	−	−
	−	+	−	+
	−	−	+	+

For all cases given in table 8.II the absolute value of C_4 is larger than that of C_6. From (1) and (2) we can derive that this means for Dy^{3+} that $|x| > 0.2$. If we introduce the last condition in fig. 8.3, the allowed x,y area is still further reduced to the region: $-0.45 \leq x \leq -0.2$; $3 \lesssim y \lesssim 25$. If we assume x and y to be within this last region we can construct fig. 8.4 giving the allowed values of C_4 and C_6 by using expressions (1) and (2).

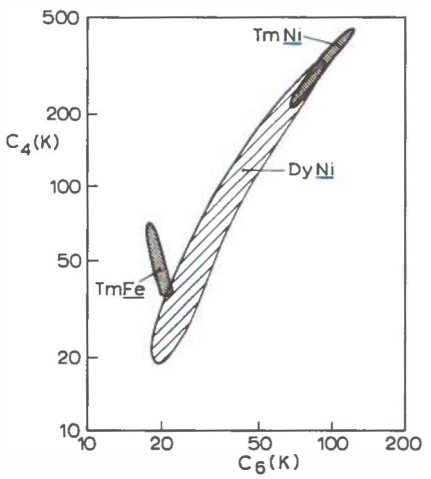

fig. 8.4
Allowed values for the crystal field parameters $C_4 = A_4 \langle r^4 \rangle$ *and* $C_6 = A_6 \langle r^6 \rangle$ *for DyNi, TmNi and DyFe.*

The allowed values of W can be obtained from fig. 8.3 by using the result of Tiekstra's analysis, that the product $|Wy|$ must lie between 6.5 and 8.7 for x,y combinations in the allowed areas of this figure. For the construction of fig. 8.4 we have taken $|Wy| = 7.6$ K.

Using the point charge model expression (3) and (4) for C_4 and C_6 Williams and Hirst [19] have calculated for a rare earth ion in silver of gold: $C_4 \approx 14$ K; $C_6 \approx 1.5$ K. A similar calculation for nickel (lattice constant = 3.523 Å) yields: $C_4 \approx 30$ K; $C_6 \approx 4.3$ K. If we compare the value for C_6 with that given in fig. 8.4, we see that the value allowed for C_6 is at least 5 times larger than the value calculated with the point charge model. The same is found for rare earths in silver and gold (see table 8.II).

With the expression

$$Wy = \tfrac{1}{2}(g_J - 1)\,\mu_B H_{ex} \qquad (7)$$

(section 2.4) the exchange field for a substitutional Dy ion in nickel can be calculated using $|Wy|$ = 7.6(1.1) K. The calculation gives H_{ex} = 0.68(10) MOe. This field is a factor 8 smaller than the exchange field for a substitutional Dy ion in iron.

For Tm^{3+} in nickel the free ion values for the magnetic and the quadrupole splitting are not well defined (see section 8.1). We take $(g_N \mu_N H_{hf})_{\text{free ion}}$ = 34(2) cm/s (see table 8.I). Combined with the magnetic splitting for the substitutional component in TmNi at 5 K: $g_N \mu_N H_{hf}$ = 7.44(14) cm/s (see table 7.VIII), we get for this case a reduction factor R_m = 0.22(2). It is more difficult to obtain the free ion value for the quadrupole splitting for Tm^{3+} in nickel. Uhrich and Barnes [27] have analysed the quadrupole splitting for Tm metal in terms of a 4f contribution and a contribution from the lattice and the conduction electrons. The last contribution corresponds to - 0.7(2) cm/s. If we subtract this value from the value $\frac{1}{4}e^2qQ^*$ = 7.13(5) cm/s we have measured for Tm metal we find $(\frac{1}{4}e^2qQ^*)_{4f}$ = 7.8(3) cm/s for the free ion value. (In nickel there is no contribution from the cubic lattice to the field gradient). This value corresponds well with the value measured by Cohen [28] for the cubic intermetallic compound $TmFe_2$: $\frac{1}{4}e^2qQ^* = 22 \times 10^{-7}$ eV ≙ 7.9 cm/s. We take for the free ion value of the quadrupole splitting: $(\frac{1}{4}e^2qQ^*)_{\text{free ion}}$ = 7.9(4) cm/s. For the substitutional component in TmNi we have measured a quadrupole splitting of 1.04(18) cm/s, so that the reduction factor of the quadrupole splitting is R_q = 0.13(3).

If we combine the calculated values of R_m and R_q with fig. 2.3 we can construct fig. 8.5 in the same way as for DyNi. We see in this figure that only for a small area of the xy plane values allowed by R_m and those allowed by R_q are the same. This area is indicated by an arrow. From table 8.IV we immediately conclude that for this area $C_4 > 0$ and $C_6 > 0$.

For TmNi at room temperature the hyperfine interaction $g_N \mu_N H_{hf}$ = 1.58(18) cm/s was measured (see table 7.X). For the substitutional component of TmNi this means that the hyperfine field has been reduced by a factor 0.21(3) with respect to the value measured at 5 K. With the theory described in section 2.7 we derive a value W = 7.7(1.1) K from this reduction. (Using xy combinations in the

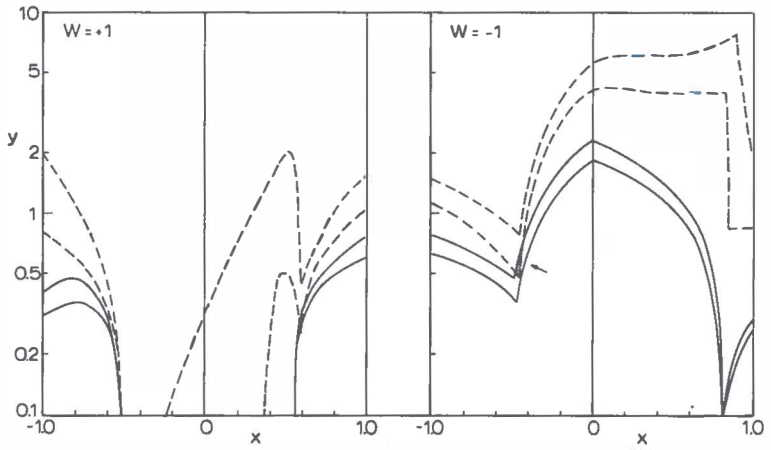

fig. 8.5. Plot of allowed xy combinations for TmNi.

allowed area of fig. 8.5). For the exchange field we calculate: H_{ex} = 0.82(12) MOe. This value compares well with the exchange field of 0.68(10) MOe found for DyNi. In the same way as for DyNi the allowed area in the C_4, C_6 plane was calculated for TmNi. The result is given in fig. 8.4. We see from this figure that C_4 and C_6 have a region of overlap for Dy^{3+} and Tm^{3+} in nickel.

We conclude this section by giving the results from a similar analysis as that described above for TmFe, using the theory of section 2.8.

For TmFe a magnetic splitting $g_N\mu_N H_{hf}$ = 32.4(7) cm/s and a quadrupole splitting $\frac{1}{4}e^2qQ^*$ = 4.99(35) cm/s were measured at 5 K (see table 8.I). Combining these values with the calculated values (also given in table 8.I) we have reduction factors: R_m = 0.89(4) and R_q = 0.63(8). Introduction of these factors in fig. 2.5 and a similar figure for R_q yields the allowed xy values shown in fig. 8.6.

In table 8.V the reduction of the hyperfine field at higher temperatures with respect to the value at 5 K is given for the substitutional component in TmFe. This reduction was derived from the over all splitting of the spectra measured at source temperatures of 77 K and 293 K (see fig. 7.11). The reduction calculated for some value of W with the theory of section 2.7

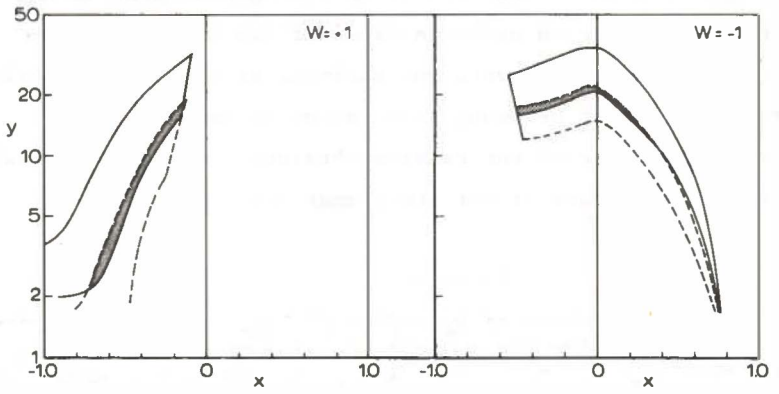

fig. 8.6. Plot of allowed xy combinations for TmFe.

lies within the error range of the reduction given in table 8.V, both at 77 K and 293 K, only for x,y values from the region $-0.5 < x < -0.3$ of fig. 8.6. This means that again only $C_4 > 0$ and $C_6 > 0$ is allowed. However, in this case the signs of C_4 and C_6 do not agree with those predicted by the point charge model ($C_4 > 0$, $C_6 < 0$; see (5) and (6)). Again the order of magnitude of C_4 and C_6 is the same as in the other cases (DyNi and TmNi). This can be seen in fig. 8.4.

Table 8.V.

Reduction of hyperfine field with respect to value at 0 K for substitutional fraction in TmFe.

Source temperature T (K)	$H(T)/H(0)$
5	1.00
77	0.81(3)
293	0.41(3)

From the value found for the scale factor W we can derive the exchange field for a substitutional Tm ion in iron: H_{ex} = 4.1(6) MOe. Cohen [28] has measured an exchange field of 4.9 MOe for the

intermetallic compound $TmFe_2$. (The exchange splitting of 44 K that Bowden et al. [12] derive from Cohen's results is wrong; the splitting is 55 K). From their analysis of an IPAC measurement Bernas and Gabriel [29] derive an exchange field of 2.5 MOe for an implanted source of TmFe. However, the estimate of Bernas and Gabriel is very rough, it might be wrong by a factor of two [30].

In table 8.VI some of the results obtained for substitutional Dy of Tm ions in iron and nickel are summarized.

Table 8.VI

Low temperature values of hyperfine fields, quadrupole splittings and exchange fields for substitutional components of DyNi, TmNi, DyFe, TmFe and for $DyFe_2$ and $TmFe_2$. (R_m and R_q are reductions with respect to the value calculated for $\langle J_z \rangle = J$).

Sample	$g_N \mu_N H_{hf}$ (cm/s)	$\lvert H_{hf} \rvert$ (MOe)	$\lvert \frac{1}{4} e^2 q Q^{(*)} \rvert$ (cm/s)	R_m	R_q	H_{ex} (MOe)
DyNi	3.28(3)	4.72(14)	1.69(2)	0.79(3)	0.54(3)	0.68(10)
TmNi	7.44(14)	1.43(3)	1.04(18)	0.22(2)	0.13(3)	0.82(12)
DyFe	4.31(2)	6.20(18)	2.76(4)	1.01(1)	0.88(5)	5.49(15)
TmFe	32.4(7)	6.23(14)	4.99(35)	0.89(4)	0.63(8)	4.1(6)
$DyFe_2$ [12]	4.52(5)	6.70(7)	3.55(35)	1.06(6)	1.14(15)	6.03
$TmFe_2$ [28]	36.0	6.9	7.9	0.98(3)	1.00(5)	4.9

8.4 Investigations of ErNi and ErFe

Mössbauer measurements on the 80.6 keV transition in ^{166}Er with implanted sources of ^{166}HoNi and ^{166}HoFe wereperformed by other members of our group [31]. The results of these measurements agree very well with our results on DyNi, DyFe, TmNi and TmFe.

The results on ErFe obtained with four different sources are given in table 8.VII. The spectra could be fitted with a unique hyperfine field and a unique quadrupole splitting. The value measured for the magnetic splitting at 4.2 K is about 6 % lower than the value that can be calculated starting from the free ion value, taking *s* electron contributions into account [10]. This is interpreted as a reduction of $\langle J_z \rangle$ below the value $\lvert \langle J_z \rangle \rvert = J$ due to

crystalline field effects.

Table 8.VII.

Results from ErFe Mössbauer measurements.

Source temp. (K)	$g_N \mu_N H_{hf}$ (cm/s)	$\frac{1}{4}e^2qQ$ (cm/s)	$H(T)/H(0)$	$Q(T)/Q(0)$
4.2	2.834(20)*	- 0.288(9)*	1	1
44.2	2.646(12)	- 0.216(21)	0.932(5)	0.79(9)
77	2.397(20)	- 0.12(4)	0.852(8)	0.41(12)

* Average of 4 measurements.

Two measurements were performed with ErNi samples; one with an unannealed source and one with a source that was annealed for 1 hour at 400°C. The spectrum of the unannealed source shows two components of about equal intensity, component 1 with H_{hf} = 7.01(14) MOe, $\frac{1}{4}e^2qQ$; - 0.20(3) cm/s and component 2 with H_{hf} = 4.76(9) MOe, $\frac{1}{4}e^2qQ$ = - 0.114(11) cm/s. In the spectrum of the annealed source the component with the smallest hyperfine field has disappeared. For the remaining high field component H_{hf} = 6.91(8) MOe and $\frac{1}{4}e^2qQ$ = - 0.170(12) cm/s.

So the annealing behaviour of the ErNi samples is comparable to that of DyNi and TmNi and an explanation on the basis of the lattice location of the implanted rare earth impurities can be given in a similar way. In this respect it is worthwhile to note that the hyperfine field found in Er metal (7.55 MOe) [32] and in $ErNi_2$ (7.44 MOe) [33] is clearly higher than that of the non-substitutional component in ErNi. So apparently no clustering of rare earth ions or precipitation of an intermetallic compound takes place during annealing to 400°C.

References of Chapter 8

1. F. Abel, M. Bruneaux, C. Cohen, J. Chaumont, L. Thomé and H. Bernas, Solid State Commun. 13 (1973) 113.
2. R.B. Alexander, J. Gellert and B. Deutch, Proc. Conf. on hyperfine interactions in nuclear reactions and decay, ed. E. Karlsson and R. Wäppling (Uppsala, 1974) p. 76.
3. L. Thomé, H. Benski and H. Bernas, Phys. Lett. A42 (1972) 327.
4. R.L. Cohen, G. Beyer and B.I. Deutch, Phys. Rev. Lett. 33 (1974) 518.
5. S. Scherrer and B. Deviot, J. de Phys. 33 (1972) 895.
6. I. Nowik, S. Ofer and J.H. Wernick, Phys. Lett. 20 (1966) 232.
7. H. Bernas, Physica Scripta 11 (1975) 167.
8. B. Bleaney, Proc. Roy. Soc. A277 (1964) 289.
9. R.L. Cohen, Phys. Rev. 169 (1968) 432.
10. L. Niesen and P.J. Kikkert in "Hyperfine Interactions studied in nuclear reactions and decay", ed. E. Karlsson and R. Wäppling (Uppsala, 1974) p. 160.
11. H. Maletta, G. Crecelius and W. Zinn, J. de Physique 35 (1974) C6-279.
12. G.J. Bowden, D.St. Bunbury, A.P. Guimaraes and R.E. Snijder, J. Phys. C1 (1968) 1376.
13. L. Grodzins, R.R. Borchers and G.B. Hagemann, Phys. Lett. 21 (1966) 214.
14. G.K. Hubler, H.W. Kugel and D.E. Murnick, Phys. Rev. C9 (1974) 1954.
15. L. Thomé, H. Bernas, J. Chaumont, F. Abel, M. Bruneaux and C. Cohen, Phys. Lett. 54A (1975) 37.
16. L. Thomé, H. Bernas, J. Chaumont, F. Abel, M. Bruneaux and C. Cohen, in "International Meeting on Hyperfine Interactions", (Leuven, 1975) p. 130.
17. H.H. Wickman and I. Nowik, J. Ph. Chem. Solids 28 (1967) 2099.
18. R.G. Barnes, R.L. Mössbauer, E. Kankeleit and J.M. Poindexter, Phys. Rev. 136 (1964) A175.
19. G. Williams and L.L. Hirst, Phys. Rev. 185 (1969) 407.
20. D. Davidov, R. Orbach, C. Rettori, L.J. Tao and E.P. Chock, Phys. Rev. Lett. 28 (1972) 490.

21. R.P. Guertin, H.C. Praddaude, S. Foner, E.J. McNiff and B. Barsonmian, Phys. Rev. B7 (1973) 274.
22. R.A.B. Devine, P. Jacques and M. Poirier, Phys. Rev. B11 (1975) 563.
23. H.C. Praddaude, Phys. Lett. A48 (1974) 365.
24. K.R. Lea, M.J.M. Leask and W.P. Wolf, J. Phys. Chem. Solids 23 (1962) 1381.
25. A.J. Freeman and R.E. Watson in "Magnetism", Ed. G.T. Rado and H. Suhl, (Academic Press, New York, 1965) Vol. IIA, p. 292.
26. G.H. Tiekstra, Internal Report, Lab. Alg. Natk. Groningen, 1975.
27. R.L. Uhrich and R.G. Barnes, Phys. Rev. 164 (1967) 428.
28. R.L. Cohen, Phys. Rev. 134A (1964) 94.
29. H. Bernas and H. Gabriel, Phys. Rev. B7 (1973) 468.
30. H. Bernas, private communication.
31. L. Niesen, P.J. Kikkert and H. de Waard, will be published.
32. R.A. Reese and R.G. Barnes, Phys. Rev. 163 (1967) 465.
33. G. Petrich, Z. Physik 221 (1969) 431.

KORTE BESCHRIJVING VAN HET ONDERZOEK.

Om deze beschrijving meer begrijpelijk te maken voor de geinteresseerde leek zullen begrippen die slechts voor de "insider" begrijpelijk zijn erin worden vermeden.

De titel van het proefschrift luidt: "Zeldzame aard onzuiverheden in ferromagnetische metalen bestudeerd met Mössbauer spectroscopie".

De "zeldzame aarden" is de groep elementen met atoomnummer 58 t/m 81 uit het Periodiek Systeem. Ze hebben sterk overeenkomende chemische eigenschappen, veroorzaakt door het feit dat ze allemaal hetzelfde aantal electronen in de twee buitenste schillen hebben. Alleen het aantal electronen in de derde schil (van buiten af gerekend), de z.g. 4f-schil, verschilt bij deze elementen. In feite zijn door ons slechts twee zeldzame aarden gebruikt: Dysprosium (Dy) met 9 electronen in de 4f-schil en Thulium (Tm) met 12 electronen in deze schil.

Radioaktieve ionen van zo'n element zijn met behulp van de isotopenseparator van ons laboratorium in dunne plaatjes ijzer (Fe) of nikkel (Ni) geschoten ("geïmplanteerd"). Ijzer en nikkel zijn ferromagnetische metalen. Bij de implantatie hadden de ionen een energie van 130 keV, wat overeenkomt met een snelheid van ongeveer 400 km/sec. Ondanks deze hoge snelheid dringen de ionen slechts over zeer kleine afstanden in het metaal door. De gemiddelde indringdiepte is 200 Å = 0,00002 mm.

Het was nodig om de zeldzame aardionen in de plaatjes te schieten, omdat dit de enige manier is om ze in sterke verdunning in ijzer of nikkel op te lossen.

Hoewel onderzoek is gedaan aan de zeldzame aarden Dy en Tm zijn radioaktieve ionen van de zeldzame aarden Terbium (Tb) en Erbium (Er) geïmplanteerd. Omdat de kernen van deze ionen radioaktief zijn vervallen ze door uitzenden van een beta-deeltje naar Dy respectievelijk Tm terwijl ze al in ijzer of nikkel zitten. De kernen van Dy of Tm zenden dan op hun beurt gammastraling uit.

Met behulp van het "Mössbauer-effekt" (in 1958 ontdekt door de Duitser Rudolf Mössbauer; hij kreeg hiervoor de Nobelprijs) kunnen zeer kleine veranderingen van de energie van deze gamma-

straling worden gemeten. (Een verandering die kleiner is dan een miljardste deel van de energie kan nog worden gedetecteerd). Zulke veranderingen worden veroorzaakt door een wisselwerking (de z.g. "hyperfijninteractie") tussen de kern van het radioaktieve ion en zijn omgeving (de electronen van het ion + de ijzer of nikkel atomen rondom het ion). Er blijkt zo bijvoorbeeld dat ter plaatse van zo'n kern een zeer sterk magneetveld (hyperfijnveld) aanwezig is. Dit veld is soms meer dan 50 keer zo sterk als dat in de sterkste electromagneten ter wereld. De sterkte van het hyperfijnveld hangt af van de plaats van het zeldzame aard ion in het ijzer of nikkel.

Door ons onderzoek hebben we kunnen vaststellen dat slechts een gedeelte (ca. 50 %) van de geïmplanteerde ionen zo in het ijzer of nikkel terecht komt, dat ze regelmatig zijn omringd door ijzer of nikkel atomen. De rest van de geïmplanteerde ionen zit op "slordige" plaatsen.

Een manier om hier achter te komen was bijvoorbeeld het ijzer of nikkel een tijdlang te verhitten ("annealen"). Door de Mössbauerspectra gemeten voor en na verhitting met elkaar te vergelijken kon worden geconcludeerd dat verhitten de omringing van alle Dy of Tm ionen onregematig maakt.

Soortgelijk onderzoek, ook met andere meetmethoden, wordt op dit moment op meerdere plaatsen in de wereld gedaan (Bell Laboratories in de Verenigde Staten, Orsay in Frankrijk, Aarhus in Denemarken, Leuven in België, München in Duitsland). Het is ook voor sommige technische toepassingen van belang. Een van deze toepassingen behelst het vervaardigen van "geïntegreerde schakelingen" (I.C.'s) voor de electronische industrie. Deze I.C.'s worden bijvoorbeeld in grote hoeveelheden in moderne computers gebruikt.